TABLES

Table 1. Scaling coefficients between rupture length, rupture width, rupture area, and moment magnitude.

Table 2. Scaling coefficients between average slip, rupture width, rupture length, rupture area, and moment magnitude.

New Empirical Earthquake-Source Scaling Laws

by Kiran Kumar S. Thingbaijam, P. Martin Mai and Katsuichiro Goda

Earth Science & Engineering
King Abdullah University of Science & Technology
Thuwal, Kingdom of Saudi Arabia
k.thingbaijam@kaust.edu.sa
(K.K.S.T., P.M.M.)

Department of Civil Engineering
University of Bristol
United Kingdom
(K.G.)

Abstract We develop new empirical scaling laws for rupture width *W*, rupture length *L*, rupture area *A* and average slip *D*, based on a large database of rupture models. The database incorporates recent earthquake source models in a wide magnitude-range (M_W 5.4 – 9.2), and events of various faulting styles. We apply general orthogonal regression, instead of ordinary least squares regression, to account for measurement errors for all variables and to obtain mutually self-consistent relationships.

We observe that *L* grows more rapidly with M_W, compared to *W*. The fault-aspect ratio (*L*/*W*) tends to increase with fault dip, which generally increases from reverse-faulting, normal-faulting, to strike-slip events. At the same time, subduction-interface earthquakes have significantly higher *W* (hence larger rupture area *A*) compared to other faulting regimes. For strike-slip events, the growth of *W* with M_W is strongly inhibited, while the scaling of *L* agrees with the *L*-model behavior (*D* correlated with *L*). However, at a regional scale where seismogenic depth is essentially fixed, the scaling behavior corresponds to the *W*-model (*D* not correlated with *L*). A consistent scaling behavior of M_W–$\log_{10} A$ with slope~1.0 is found, except for normal-faulting events. Interestingly, the ratio *D*/*W* (a proxy for average stress-drop) tends to increase with M_W, except for shallow crustal reverse-faulting events, suggesting the possibility of scale-dependent stress-drop.

The observed variations in source-scaling properties for different faulting regimes can be interpreted in terms of geological and seismological factors. We find substantial differences between our new scaling relationships and those of previous studies. Therefore, our study provides critical updates on source-scaling relations needed in seismic-tsunami hazard analysis and engineering applications.

Online Material: Figures depicting regression analysis, normality probability plots and comparisons between different source-scaling relationships, and tables listing rupture models and different earthquake source-scaling relationships.

Introduction

Earthquake source-scaling relations provide empirical equations that link observable source parameters to each other. Such scaling relations not only provide insight into earthquake mechanics (*e.g.*, Scholz, 1982; Romanowicz, 1992; Wells and Coppersmith, 1994, Mai and Beroza, 2000; Blaser *et al*., 2010; Skarlatoudis *et al*., 2016), but also constitute an essential ingredient in seismic-tsunami hazard studies (*e.g*., Stafford, 2014; De Risi and Goda, 2016). However, available databases are limited, while uncertainties in the source parameters (primarily rupture length L, rupture width W, average displacement D and seismic moment M_0) are hardly considered. Our study tries to partially overcome these limitations by using the database of finite-fault source models (Mai and Thingbaijam, 2014) that spans a wide magnitude-range (M_W 5.4 – 9.2), but also provides multiple estimates of source-parameters for a large number of events that have been studied by different research groups. In addition, for a set of earthquakes, information on fault segmentation is available that so far has not been included into any source-scaling analysis.

Several studies investigated earthquake source-scaling properties (for a summary, see Stirling *et al*., 2013), however, most of them employed datasets not limited to rupture models, but based on indirect estimates of source parameters (*e.g*., early aftershocks) and surface-rupture observations that are prone to large uncertainties. By using only inverted

rupture models for which the uncertainties in source parameters can be consistently inferred, we thrive for a more objective assessment of the source-scaling properties.

The inversions for rupture models using seismic and/or geodetic data determine the spatiotemporal properties of the rupture processes. Therefore, the corresponding source dimensions L, W, and A, as well as the seismic moment M_0 are more accurately and self-consistently estimated than from aftershock zones and/or surface ruptures. Earlier investigations of source-scaling properties based exclusively on rupture models lacked very-large magnitude events (*e.g*., Somerville *et al.*, 1999; Mai and Beroza, 2000). Other studies focused on region-specific scaling relationships (Murotani *et al*., 2008; Yen and Ma, 2011; Rodríguez-Pérez and Ottemöller, 2013; Ramírez-Gaytán *et al*., 2014), or a specific fault regime, like subduction events (Murotani e*t al*., 2013; Ye *et al*., 2016; Skarlatoudis *et al*., 2016). Thus, there is a need to re-examine earthquake source-scaling properties using a global set of rupture models, considering different faulting regimes and including very large and mega-thrust events. Such a study is now feasible because of the increased availability of inverted kinematic source models for past earthquakes.

We emphasize that regression analyses between the different parameters should produce empirical scaling laws that are fundamentally self-consistent. As explained by Leonard (2010), the self-consistency implies that the scaling equations between different parameters mutually agree with each other as well as with the definition of seismic moment. Another requirement is that scaling relationship remains invariant under interchange of variables; for instance, relationship between magnitude and rupture length should be the same irrespective of which of the two parameters is the independent or dependent variable. This condition can be met by enforcing theoretical expectations on

the scaling coefficients (*e.g.*, the slope of a linear model) in the regression analysis (*e.g.*, Somerville *et al.*, 1999; Hanks and Bakun, 2002; Leonard, 2010). However, in the present study, we make no such prior assumptions regarding the scaling coefficients in order to let the data speak, not theoretical expectations. Instead, we attempt to improve the regression analysis considering errors-in-variables models by applying general orthogonal regression. Thus, the self-consistency of the scaling laws of this study is data-driven with no prior assumptions about the relationships.

In the following sections, we describe the finite-fault rupture model database, our approach to the data selection, classification, and preprocessing, the regression technique, and then we present the new empirical scaling laws for the earthquake source. To develop the scaling laws, we adopt a standardized approach: we compute the specific source parameter from the rupture models, and then apply regression analysis on the resulting data. More specifically, we first address the scaling properties of rupture dimensions considering different faulting regimes, and compare our results with previous studies. Next, we examine the implications, immediate conclusions and physical interpretations relevant to rupture dynamics from the new relationships, and discuss their practical aspects.

Finite-fault Rupture Models

The present study is motivated by the recently augmented online repository of kinematic earthquake rupture models, the SRCMOD database (Mai and Thingbaijam, 2014). This database embodies the recent surge in finite-fault source-inversion studies of earthquakes. For discussions on the different data and inversion techniques used to

115 develop these rupture models, we refer the readers to Mai and Thingbaijam (2014). The
116 SRCMOD database comprises the current largest online repository of rupture models for
117 past global earthquakes, organized in a uniform and consistent manner.

118 It is important to note that appreciable uncertainties exist for these rupture models
119 owing to the ill-posed nature of earthquake source inversions because of limited and non-
120 uniform data coverage, incompletely known crustal structure, and unknown errors in data
121 and modeling assumptions (Beresnev, 2003; Mai *et al*., 2007, 2016). Nevertheless, these
122 rupture models were obtained by applying known physics of seismic wave excitation and
123 propagation, and/or crustal deformation due to earthquake slip. Thus, these rupture
124 models represent the currently best-resolved attributes of kinematic earthquake source
125 properties, and have been extensively used to investigate the rupture physics (for reviews
126 on this aspect, see for example Mai and Thingbaijam, 2014; Thingbaijam and Mai, 2016).
127 Varying techniques and data applied by different research teams to study the same event
128 introduce (intra-event) variability in the rupture models, but they also minimize possible
129 bias due to inversion techniques or data used for the source-inversion. Thus, multiple
130 rupture models for the same event allow accounting for independent (and usually
131 different) source-parameter estimates.

132 Before we describe our approach for selecting rupture models for the analysis, we
133 briefly discuss the relevant features of a rupture model. A rupture model usually
134 comprises several kinematic source parameters: slip, rise time (duration of slip), rupture-
135 onset time, and rake (angle of slip direction), assigned at node-points (or sub-faults) on
136 the rupture plane(s). In the present study, we are concerned only with the final
137 displacement over the fault plane, *i.e*. the slip distribution, while the temporal rupture

evolution is neglected. The spatial extent of the slip distribution along strike and down dip is related to the rupture length and rupture width. The size of the sub-faults, *i.e*. the spacing of the node-points with respect to the rupture-area defines a nominal spatial resolution of the model. Owing to the chosen spatial discretization in the source inversion and the need to utilize band-limited data, rupture models do not account for small-scale fault-surface roughness (occurring on a 1–100 meter scale), but incorporate large-scale fault segmentations (occurring on a scale of several kilometers).

Data Selection and Classification

The spatial resolution of rupture models largely decides whether application of a specific statistical analysis will be statistically meaningful or not. Accordingly, we apply the following criteria to examine the suitability of the rupture models:

(1) Magnitude $M_W \geq 5.0$, as smaller events are likely to be less well resolved in the inversions;

(2) Number of sub-faults in down-dip or along-strike larger than 3 to allow computing effective source dimensions (see below);

(3) When, for the same event, multiple rupture models are produced by the same author(s), we use its latest version.

Figure 1 depicts the distributions of the selected rupture models in terms of slip-centroid depth, fault-dip and average rake angles. We use the centroid depth of the slip distribution (as measure of effective rupture depth) to overcome the lack of hypocentral locations in inversions of geodetic data. This initial selection comprises of 268 rupture

models from 142 earthquakes, which we further examine in terms of different faulting regimes.

Earthquake source-scaling properties are found to depend on the seismotectonic regime and faulting style (see Stirling *et al*., 2013). Therefore, we group rupture models according to the faulting styles. We broadly classify seismotectonic regimes as either continental, oceanic or subduction zones. Figure 1 shows that the tectonic regime largely control the distributions of rupture depth and fault dip. For continental earthquakes, the slip-centroids are well confined within depth of 20 km. On the other hand, earthquakes in subduction zones can occur at significant depths. Subduction-interface events occur within depth of 50 km, while intra-slab events can be observed at depths over 100 km. Furthermore, we find that the average fault-dip angles δ are correlated with average rake angles, transitioning from steeper to shallower from strike-slip ($\delta \sim 70°–90°$), to normal-faulting ($\delta \sim 50°–60°$), to shallow crustal reverse-faulting ($\delta \sim 40°–50°$), and finally to subduction-interface ($\delta \sim 10°–30°$) events.

In continental and oceanic crust, earthquakes occur within the tectonic plate (intraplate) or at the interface between two tectonic plates (interplate). Intraplate events can be located either at the margins or interiors of the tectonic plates (Scholz *et al*., 1986). In the present dataset, intraplate events at active plate margins – mostly those in western North America and inland Japan – dominate the continental reverse-faulting events. The source-scaling properties of events in stable continental regions (SCR) are reported to be different from interplate as well as intraplate events (*e.g*., Johnston and Kanter, 1990; Leonard, 2014). However, we have only six events associated with SCR, and therefore, exclude SCR-events from our analysis.

For reverse-faulting earthquakes, we distinguish between shallow crustal and subduction-interface events. We classify the 2015 Gorkha earthquake as a continental subduction event owing to its rupture characteristics (*e.g.*, Goda *et al.*, 2016). Figure 2 illustrates the different dip-slip regimes in an oceanic-continental subduction zone. These include continental, back-arc and subduction-interface thrust faults, and outer-rise and subduction inslab normal faults. They differ from each other in terms of their associated tectonic loading mechanisms, as well as in dominating material properties. For the analysis, we do not differentiate continental and shallow back-arc thrust faulting, but group them as reverse-faulting (shallow crustal) events. However, we analyze the subduction-interface events separately. Owing to limited data, we examine outer-rise and inslab normal faulting events jointly, although outer-rise events occur at shallower regions and have different tectonic settings than subduction inslab events that occur within the dipping plate at larger depths.

We define the dominant faulting types, strike-slip, normal, reverse, or oblique-slip, based on average rake angle. Since considerable spatial variability of rake angles across a rupture plane may occur, we adopt a slip-weighted average rake angle,

$$\lambda_{avg} = \sum u_i \lambda_i \Big/ \sum u_i \quad , \quad u_i \geq \frac{1}{3} u_{max} \qquad (1)$$

where u and u_{max} refer to slip and maximum slip on the rupture plane, respectively. The stipulated range of slip corresponds to large-slip asperities (Mai *et al*., 2005), and limits the computation for the slip-type to prominent parts of the rupture.

Figure 1 indicates considerable variability of rake-angles in our database. In many cases, clusters are observed that can be attributed to multiple models for the same events. For instance, continental events with average rake angles between 130°–150° amount to only six earthquakes but 16 rupture models altogether. We examine whether oblique-slip events exhibit any characteristic scaling properties. First, we apply an optimal case with bin-size of 15° with rake angle centered at 0°, -180° for strike-slip, 90° for reverse-faulting and -90° for normal-faulting events, thus clearly separating oblique-slip events. Then, we assess oblique-slip events in terms of data scattering with respect to these three faulting types. Overall, the data scatter does not support characteristic scaling of oblique-slip events.

Therefore, we classify the oblique-slip events into either one of the three faulting types, but do not analyze them specifically. Only three events with very atypical rupture dimensions (for their dominant faulting type) are examined separately, namely the 1978 M_W~7.1 Tabas (one source model), the 1989 M_W~6.9 Loma Prieta (five source models), and the 2008 M_W~7.9 Wenchuan (four source models) earthquakes. These events are characterized by strongly oblique slip, comprising reverse dip-slip with considerable strike-slip components.

In summary, we classify the earthquakes into four broad categories based on the faulting regimes. These include (i) shallow crustal reverse-faulting events, (ii) subduction-interface events, (iii) strike-slip events, and (iv) normal-faulting events. We exclude a few events with hypocenters deeper than 30 km that are not located at subduction-interface. These include the 2005 M_W~7.2 Honshu, Japan earthquake, the 2006 Pingtung, Taiwan (doublet, M_W~6.9 and M_W~6.8) earthquakes (Yen *et al*., 2008),

the 2009 $M_{W\sim}$7.6 Padang, Indonesia earthquake, the 2011 $M_{W\sim}$7.4 Kermadec Islands, New Zealand earthquake, and the 2012 $M_{W\sim}$7.6 Samar, Philippines earthquake. Additionally, we remove three single fault-segment models but retain one model with multiple fault-segments for the 2012 $M_{W\sim}$8.6 Sumatra earthquake in view of the rupture complexity of this strike-slip event. In total, our analysis uses 253 rupture models of 133 earthquakes, which include (i) 15 shallow crustal reverse-faulting events with 35 models, (ii) 49 subduction-interface events with 101 models, (iii), 40 strike-slip events with 75 models, and (iv) 23 normal-faulting events with 29 models (Table S1 in the Electronic Supplement).

Data Processing

Because earthquake-source inversions a priori define the fault plane to estimate the kinematic rupture process, they may overestimate the size of the rupture plane, leading to regions of low (or zero) slips at the fault edges (Somerville *et al*., 1999; Mai and Beroza, 2000). Some inversion procedures include an iterative reduction of the fault plane to an optimal size, or use waveform data to constrain the rupture extents (*e.g*., Henry *et al*., 2000). Different approaches and data (*e.g*., aftershocks catalogue) to estimate the initial fault-plane size result in intra-event variability of the rupture dimensions. Hence, the originally defined rupture size could be adequate, overestimated, or even underestimated.

Therefore, it is necessary to implement a consistent measure of rupture dimensions based on the slip distributions. Somerville *et al*. (1999) trimmed slip models by removing rows/columns if their average slip is less than 0.3 times the overall average

slip. Mai and Beroza (2000) introduced the concept of effective source dimensions based on the autocorrelation width of the spatially variable slip. Thingbaijam and Mai (2016) extended this approach by applying constraints of sub-fault size (spatial grid-spacing), locations of large-slip asperities ($u \geq \frac{1}{3}\, u_{max}$, Mai *et al*., 2005), and if present, surface ruptures.

In this study, we trim each rupture model to its effective source dimension following Thingbaijam and Mai (2016). Note that slip distributions are expected to taper (to zero or low slip values) at their rupture terminations due to regions of increased frictional strength (Scholz, 2002; Manighetti *et al*., 2005). In this context, the autocorrelation width captures the spatial extent of the slip distribution that is consistent with slip tapering and hence the dynamic rupture process. However, we do note that there are exceptions to moderate-to-low absolute slip at the rupture edges. These exceptions include surface rupturing, and rupture edges at fault-intersections. Therefore, the locations of slip asperities and evidence of surface ruptures are crucial in deciding the effective rupture size.

Regression Analysis

We investigate earthquake source-scaling laws that correlate parameters of rupture geometry such as rupture width W, length L, area A (= $W\,L$), average slip D, and seismic moment M_0. The scaling relationships are generally linear in double-logarithmic space, for the entire range of the data or only parts of it, in the form

$$log_{10}(y) = b\ log_{10}(x) + a \quad (2)$$

This functional form is simple and well established. In case of moment magnitude M_W (which we adopt in the present study), the functional form is log-linear, which is easily understood from the relationship between M_W and M_0 (Hanks and Kanamori, 1979),

$$log_{10}(M_0) = 1.5M_W + 9.05 \quad (3)$$

where M_0 is in Nm. To develop empirical laws, the slope and intercept (b and a in Eq. 2) are estimated by regression on the data.

Most studies adopt ordinary least squares (OLS) regression to derive the scaling relationships (*e.g.*, Wells and Coppersmith, 1994; Strasser *et al*., 2010; Leonard, 2010). OLS assumes negligible uncertainty of the independent variable compared to the dependent variable. Later we show that this assumption does not hold. To account for possible measurement errors, Blaser *et al.* (2010) and Rodríguez-Pérez and Ottemöller (2013) applied orthogonal regression (OR). Previously, Stock and Smith (2000) used a generalized version of the OR-method. Thingbaijam and Mai (2016) also employed the OR-technique to relate magnitude and rupture area. In the present study, we use general orthogonal regression (GOR) technique to derive the relationships to fully consider measurement errors in the analysis.

General orthogonal regression (Fuller, 1987; Carroll and Ruppert, 1996; Castellaro *et al*., 2006) minimizes the weighted orthogonal distances of the data points to

the regression line, instead of only the vertical distances, and yields a relationship that is interchangeable such that $y = f(x)$ and $x = f(y)$. It assumes that the variables are linearly related (*i.e.*, applicability of linear model), and that errors of the variables are independent and normally distributed. The slope b in the linear relation (Eq. 2) is then computed as follows,

$$b = \frac{\sigma_y^2 - \eta\sigma_x^2 + \sqrt{(\sigma_y^2 - \eta\sigma_x^2)^2 + 4\eta\sigma_{xy}^2}}{2\sigma_{xy}} \quad (4)$$

where σ_x^2, σ_y^2 and σ_{xy}^2 denote the sample variance of x, variance of y, and covariance between x and y, respectively. When the error variance ratio of the variables, η ($=\sigma_y^2/\sigma_x^2$), is equal to 1, Eq. (4) corresponds to orthogonal regression. Based on the estimated slope, the intercept parameter is calculated as,

$$a = \bar{y} - b\bar{x} \quad (5)$$

where $\bar{x}$ and $\bar{y}$ are the average values of x and y.

Currently, the available data on earthquake source parameters, specifically for multiple intra-event rupture models, are not sufficient for reliable (empirical) analysis of measurement errors. However, we take a different perspective on this problem with respect to previous studies when evaluating source parameters independently, for instance, earthquake magnitude, surface rupture length, surface displacement (Bonila *et*

316 *al.*, 1984; Wells and Coppersmith, 1994) by relating this problem back to the
317 computation of seismic moment. Following Aki (1966), the fundamental equation is
318 given by
319
320 $$M_0 = \mu\, A\, D \qquad (6)$$
321
322 where μ is crustal rigidity (usually assumed constant and typically μ = 3.3 x 10^{10} Nm^{-2}). It
323 implies that the error variances of A and D control that of M_W (see also Eq. 3). We can
324 therefore express the error variance of moment magnitude in terms of the error variances
325 of $\log_{10} A$ and $\log_{10} D$ (denoted by $\sigma^2_{\log 10\, A}$ and $\sigma^2_{\log 10\, D}$) as
326
327 $$\sigma^2_{Mw} = \frac{4}{9}(\sigma^2_{log10\, A} + \sigma^2_{log10\, D}) \qquad (7)$$
328
329 Similarly, the error variance of $\log_{10} A$ can be expressed as
330
331 $$\sigma^2_{log10\, A} = \sigma^2_{log10\, L} + \sigma^2_{log10\, W} \qquad (8)$$
332
333 We hypothesize that the measurement errors of L, W and D are independent and
334 identically distributed (i.i.d.) random variables, affected by the above described
335 parameterization and modeling assumptions that govern source-inversion uncertainties.
336 We note that published empirical relationships predicting $\log_{10} A$ and $\log_{10} D$ from M_W
337 have comparable standard errors (*e.g.*, Mai and Beroza, 2000; Goda *et al.*, 2016),

similarly for relationships that predict $\log_{10} L$ and $\log_{10} W$ from M_W. Therefore, we assume that the error variances of $\log_{10} A$ and $\log_{10} D$ are comparable.

To realize first-order estimates of error-variance ratios, we consider that error variances of $\log_{10} L$ and $\log_{10} W$ are of the same order. Such an assumption is usually adopted if parameters have been computed by the same method with unknown measurement errors. We note that source inversions of geodetic data or near-source waveforms are associated with limited resolution of slip at depth (*e.g.*, Page *et al.*, 2009; Zhou *et al.*, 2004) that may lead to larger uncertainty of W (compared to that of L). However, our database includes a larger number of source models from teleseismic and joint inversions, as well as multiple source models for many events, justifying our assumption. Thus, combing Eqs. (7) and (8), we obtain

$$\frac{\sigma^2_{log10\,L}}{\sigma^2_{Mw}} \sim \frac{\sigma^2_{log10\,W}}{\sigma^2_{Mw}} \sim \frac{9}{16} \qquad (9)$$

Consequently, the total measurement error of M_W is larger than and independent of those of L, W and D if these physical parameters are individually considered.

Note that the actual datasets are likely to have error-variance ratios somewhat different from these estimates due to factors like data sampling, inherent data scatter (aleatoric) and heteroscedasticity (variable η for different data-points). Furthermore, orthogonal regressions may yield scaling relationships that do not exactly correlate the scaling of L and W to that of A. Such inconsistency would be marginal, but can be avoided by computing the scaling relationship of A from those of W and L, instead of

direct regression (*e.g*., Blaser *et al*., 2010). Given these factors, it is necessary to confirm if the first-order theoretical estimates of error variance ratio are appropriately chosen.

To do so, we use synthetic tests. We generate test datasets considering slopes equal to 0.4 and 0.6 for M_W – $\log_{10} W$ and M_W – $\log_{10} L$ for uniformly distributed M_W values. The choice of these slope values is motivated considering previously published scaling relations (*e.g*., Mai and Beroza, 2000; Leonard 2010). Then, we apply normally distributed random errors adjusted to achieve the desired error variance ratio.

As depicted in Figure 3, we consider four cases: (1) error variances according to the theoretical estimates (Eq. 9), (2) smaller error for both $\log_{10} W$ and $\log_{10} L$ compared to the theoretical estimates ($\sigma^2_{log10\,W}/\sigma^2_{Mw}$= 0.09, and $\sigma^2_{log10\,L}/\sigma^2_{Mw}$= 0.09), (3) larger error for $\log_{10} W$ and smaller one with $\log_{10} L$ than the theoretical estimates ($\sigma^2_{log10\,W}/\sigma^2_{Mw}$= 0.90, and $\sigma^2_{log10\,L}/\sigma^2_{Mw}$= 0.09), and (4) larger error for both $\log_{10} W$ and $\log_{10} L$ compared to the theoretical estimates ($\sigma^2_{log10\,W}/\sigma^2_{Mw}$= 0.90, and $\sigma^2_{log10\,L}/\sigma^2_{Mw}$= 0.90). The error variance of M_W is fixed in all these cases. Since the data are limited in practice, we generate only 30 pairs of data-points each time, and apply GOR using the theoretical estimates of η. Figure 3 shows that the distributions of the estimated slope b have comparable scatter in all four cases. Overall, the distributions exhibit marginal shifts of the peak (highest probability) from the actual values, although these shifts do not statistically impact the scaling behavior implied by the slope b. Thus, we conclude that the theoretical estimates of η are practical and adequate for the regression analysis.

To analyze the present dataset, we first develop the scaling relationships between M_W and $\log_{10} W$, and between M_W and $\log_{10} L$. Then we apply these relationships using the definition of seismic moment (Eqs. 3 and 6) in the regressions to develop the

383 remaining scaling laws. This approach is similar to Leonard (2010), however we avoid
384 prior assumptions on the scaling coefficients and/or fault-aspect ratio (L/W). During the
385 regression, we estimate the errors (standard deviations) for the scaling coefficients using
386 the delete-one jack-knife technique (Efron, 1982).

387 We also validate the developed linear models by testing for normality of the
388 residuals, using the Lilliefors test (Lilliefors, 1967) and the Shapiro-Wilk test (Shapiro
389 and Wilk, 1965). The Lilliefors test evaluates the statistical significance based on the
390 maximum discrepancy between the empirical cumulative distribution and normal
391 cumulative distribution to reject the null hypothesis (*i.e.*, normally distributed data). The
392 Shapiro-Wilk test applies a frequency measure based on normal scores (Ghasemi and
393 Zahediasl, 2012). In both tests, we consider a significance level of 0.05. The null
394 hypothesis is rejected if the test statistics results in h =1, otherwise it is not rejected. On
395 the other hand, if p (or p-value) is larger than the significance level, the null hypothesis is
396 not rejected.

397

398 **Empirical Scaling Laws for Rupture Dimensions**

399 To put our new empirical scaling laws in context, let us first discuss a few widely
400 accepted concepts of earthquake source scaling. An often cited scaling behavior is that of
401 self-similarity, which implies that any change in M_0 requires proportional changes in W,
402 L, and D (Kanamori and Anderson, 1975). Accordingly, the relations between fault
403 parameters and seismic moment (moment magnitude) take on the form $L \propto M_0^{1/3}$, $W \propto$
404 $M_0^{1/3}$, $D \propto M_0^{1/3}$, and $A \propto M_0^{2/3}$. This scaling behavior assumes constant fault-aspect
405 ratio (L/W), and is associated with scale-invariant stress-drop.

406 Regardless of whether stress-drop is scale-invariant or not, the $A \propto M_0^{2/3}$ scaling
407 has been observed to be consistent with empirical scaling relationships (Wells and
408 Coppersmith, 1994; Somerville *et al*., 1999; Hanks and Bakun, 2002; Murotani *et al*.,
409 2008; Leonard, 2010; Skarlatoudis *et al*., 2016). On the other hand, several studies
410 reported that L grows faster with increasing magnitude (M_W>6) compared to the growth
411 of W (*e.g.*, Mai and Beroza, 2000; Henry and Das, 2001; Papazachos *et al*., 2004; Blaser
412 *et al*., 2010; Leonard, 2010).

413 For very large strike-slip earthquakes occurring on quasi-vertical faults, the
414 seismogenic depth restricts the growth of W. Depending on whether D is controlled by L
415 or W, the two different paradigms of the L-model and the W-model have been debated.
416 The L-model proposes that D scales with L. In contrast, in the W-model, D is independent
417 of L (Scholz, 1982, 1994). The L-model exhibits $M_0 \propto L^2$ (or $M_W \propto L^{4/3}$) scaling, and is
418 supported by empirical evidences (*e.g.*, Pegler and Das, 1996). On the other hand, the W-
419 model agrees with dislocation theory and shows $M_0 \propto L$ (or $M_W \propto L^{1.5}$) scaling once W
420 is bounded by the finite seismogenic depth of the crust (Romanowicz, 1992;
421 Romanowicz and Ruff, 2002). It also has been suggested that the average slip could be
422 between these two end-member models (Bodin and Brune, 1996; Blaser *et al*., 2010;
423 Leonard, 2010). King and Wesnousky (2007) proposed that constant stress-drop scaling
424 for strike-slip earthquakes could be realized if coseismic slip occurs below the
425 seismogenic zone. Recent physical and theoretical models explored this hypothesis (*e.g*.,
426 Shaw and Wesnousky, 2008; Shaw, 2009; Jiang and Lapusta, 2016).

427 In the present study, we do not apply any theoretical constraints a priori on the
428 regression analysis, but we relate to them when discussing the empirical scaling laws. In

the following sub-sections, we describe the empirical scaling laws for W, L, and A for the different faulting regimes. Table 1 lists the scaling coefficients between M_W and $\log_{10} W$, $\log_{10} L$ and $\log_{10} A$ given by the regressions. We also compare our results with independent datasets of previous studies. Additionally, we examine the scaling properties of fault-segment dimensions for multi-segment rupture models.

Magnitude *versus* Rupture Width

Strike-slip events on quasi-vertical faults are strongly affected by the finite width of the seismogenic layer. However, the thickness of the seismogenic layer varies from continental to oceanic crust, across back-arc and fore-arc regions along subduction zones, and even along major strike-slip faults as these cross different geological-tectonic units. We first investigate linear and bilinear relationships of M_W versus $\log_{10} L$ considering only continental strike-slip events, taking into account the scaling of W (see Appendix-A). We note that the scatter in the data does not allow for a clear discrimination between linear and bilinear relationships for M_W versus $\log_{10} L$ (Figs. A1 and A2). However, we find that W grows gradually with increasing M_W, and does not saturate as expected from the W-model. This finding supports a linear relationship, rather then a bilinear one. Therefore, we apply linear relationships to describe the source-scaling properties of strike-slip earthquakes.

Figure 4 plots the regression analyses of $\log_{10} W$ against M_W for the different faulting regimes (see Figure S1 for separate plots for each faulting regime). Statistical tests do not reject normally distributed residuals (Figure S2). We observe that there are systematic deviations from self-similar scaling in the growth of W with increasing M_W

452 amongst the different faulting regimes, with slow to rapid *W*-increase from strike-slip,
453 normal-faulting, subduction-interface, and crustal reverse-faulting events. In fact, the
454 relationship for shallow crustal reverse-faulting events is close to self-similar scaling
455 (with slope ~ 0.44).

456 Compared to other faulting regimes, subduction-interface events are associated
457 with much larger *W* for a given M_W. Normal-faulting and strike-slip earthquakes (in this
458 order) have larger *W* than the crustal reverse-faulting earthquakes for lower magnitudes,
459 but smaller *W* for larger magnitudes. This transition of regimes comes at M_W~6.5 and
460 M_W~7.2 for strike-slip and normal slip events, respectively, relating to the differences in
461 the slope of the scaling relationships: 0.44 (reverse-faulting), 0.32 (normal faulting), and
462 0.26 (strike-slip).

463 An important question is whether rupture models for mega-thrust events (M_W >
464 8.5) saturate in *W* (owing to finite down-dip seismogenic width). Several lines of
465 arguments can be made to address this issue. Firstly, we have very few events (only four)
466 in this magnitude range, although a median estimate of $W \sim 200$ *km* is consistent. Similar
467 median values across a narrow range of magnitude are not unusual, considering the
468 inherent uncertainties of *W* estimates. Secondly, compared to the global distribution of
469 average seismogenic depth (Herrendörfer *et al*., 2015), these estimates of *W* are within
470 the bounds of the down-dip seismogenic depth, except for the 2011 Tohoku earthquake.
471 In addition, the fault-dip and down-dip seismogenic depth vary across different
472 seismotectonic regions (Pacheco *et al*., 1993; Llenos and McGuire, 2007). Thirdly,
473 earthquake ruptures have been observed to extend down-dip into the aseismic regions.
474 Hence, *W* may not be constrained by the seismogenic depth only (*e.g*., Kanamori and

McNally, 1982; Strasser *et al.*, 2010; Jiang and Lapusta, 2016). Based on these factors, we conclude that a width saturation of mega-thrust earthquakes is currently not evident, specifically at the global scale, although it may occur in specific subduction zones (even at segments of subduction zone). Previously, Skarlatoudis *et al*. (2016) arrived at a similar conclusion.

Magnitude *versus* Rupture Length

Figure 5 depicts the regression analysis between M_W and $\log_{10} L$ for different faulting regimes. In Figure S3, we provide separate plots for each faulting regime. Statistical tests support normally distributed residuals (Figure S4). The linear relationships for crustal reverse-faulting events and subduction-interface events have similar slopes ($b \sim 0.6$) that are inconsistent with self-similar scaling.

Our scaling relationship for subduction-interface events is more consistent with very long rupture (~1000 km) associated with the M_W~9.1 2004 Sumatra earthquake, compared to rupture length (~350 km) associated with the 2011 M_W~9.0 Tohoku earthquake (although the regression analysis include both). However, the Tohoku earthquake has been associated with exceptionally complicated rupture processes, with possible repeated rupturing of asperities (*e.g.*, Lee e*t al*., 2011; Galvez *et al*., 2016).

Interestingly, the scaling of L for normal-faulting events supports self-similar scaling. This observation is statistically consistent even when excluding outer-rise and inslab events. Our analysis leads us to speculate that self-similar scaling occurs at smaller magnitudes (M_W<5.5) for strike-slip, normal-faulting and reverse-faulting earthquakes.

Such convergence to self-similar scaling could occur at $M_W < 7.0$ for the subduction-interface earthquakes.

With slope ~0.7 in the scaling relationship (close to that implied by the *L*-model), we find that length *L* of strike-slip events grows much faster with M_W compared to other faulting regimes (Figure 5). The scaling relationship developed using all strikes-slip events (Figure 4) does not show statistically significant differences from that obtained using only the continental events (Figures A1 and A2). Additionally, the 2012 M_W ~8.7 Sumatra earthquake had a very complex rupture mechanism, which consists of multiple individual ruptures (Yue *et al*., 2012). However, exclusion of this outlier event does not significantly impact the regressions.

Magnitude *versus* Rupture Area

Although the scaling of *W* and *L* with respect to M_W often deviates from self-similar scaling, the scaling of *A* is overall statistically consistent with self-similarity, except for normal-faulting earthquakes (Figures 6, S5 and S6). Generally, the growth of *W* with increasing M_W is slower than predicted by self-similar scaling, which however is compensated by a more rapid growth of *L* with increasing M_W, leading in combination to self-similar scaling. However, this is not the case for normal-faulting events, which show self-similar scaling of *L* but not of *W*.

For a given magnitude, subduction-interface earthquakes generally occupy the largest rupture area, while shallow crustal reverse-faulting earthquakes are the smallest. The scaling relationships also predict that strike-slip and normal-faulting events with

519 larger magnitudes (M_W>7.5) occupy a rupture area that is comparable (or smaller) than
520 that of shallow crustal reverse-faulting events.
521
522 **Scaling of Average Slip**
523 Let us examine how *D* relates with *W*, *L*, *A*, and M_W. The scaling coefficients
524 obtained from the GOR analysis are given in Table 2. The correlations (indicated by the
525 correlation coefficient) are poor between $\log_{10} W$ and $\log_{10} D$, except for shallow crustal
526 reverse-faulting events, but are somewhat higher between $\log_{10} L$ and $\log_{10} D$ (see Figs.
527 S7 and S8 in the electronic supplement). As shown in Figure 7, the relationships between
528 $\log_{10} A$ and $\log_{10} D$ generally agree with self-similar scaling of *A*, and are consistent with
529 the definition of M_0 such that $D \propto A^{0.5}$. However, normal-faulting events tend to deviate
530 from self-similar scaling. Thus, for a specific faulting regime, the scaling of *D* with *A* can
531 be identified with how *A* scales with M_W.
532 Likewise, the regressions between M_W and $\log_{10} D$ are statistically consistent
533 with self-similar scaling with slope b ~0.5, except for the normal-faulting events (see
534 Figure S9 in the electronic supplement). We note that the average slip associated with the
535 2011 Tohoku earthquake was exceptionally large. In general, the scatter associated with
536 the scaling of *D* (either with respect to *A* or M_W) suggests possible variability of stress-
537 drop within each faulting regime.
538
539 **Comparisons with Independent Dataset and Previous studies**
540 To evaluate our new empirical scaling laws against independent data, we use the
541 compilation by Blaser *et al*. (2010) whose original data sources are Wells and

542 Coppersmith (1994), Geller (1976), Scholz (1982), Mai and Beroza (2000), Konstantinou
543 *et al*. (2005), and several other authors. To completely decouple it from the present
544 database, we exclude the data used by Mai and Beroza (2000). We also exclude the data
545 for events prior to 1964 for which we consider the source-parameter estimates to be much
546 less accurate (*e.g.*, Blaser *et al*., 2010). Instead of conducting additional regressions with
547 this alternative dataset, we calculate residuals (difference between actual and predicted
548 value) by applying our empirical scaling relationships to this dataset.

549 Figure 8 shows the distributions of residuals with respect to magnitude. For M_W
550 versus $\log_{10} L$, the scaling relationships agree reasonably well with the dataset (indicated
551 by the mean trend close to 0), except for subduction-interface events with mostly
552 negative residuals (Fig. 8a). In case of M_W versus $\log_{10} W$, our scaling laws generally
553 predict larger W. The residuals are negatively biased for strike-slip earthquakes and
554 strongly for subduction-interface and normal-faulting events (Fig. 8b).

555 Our analysis of residuals suggests that aftershock maps generally produce smaller
556 W compared to the source inversions. This difference is remarkable for subduction-
557 interface and normal-faulting events, especially for those located in the oceanic crust.
558 Taking into account the aspects of data quality and inherent statistical scatter, we
559 conclude that our new empirical scaling laws are compatible with the independent dataset
560 of Blaser *et al*. (2010).

561 For reverse-faulting shallow crustal events, the present study generally agrees
562 with previous ones in predicting W, L and A from magnitude (Table S2, Figure S10).
563 However, we do not corroborate the scaling coefficients for W (specifically, slope) given
564 by Wells and Coppersmith (1994) and Leonard (2010). Furthermore, the new scaling

565 laws predict shorter L compared to these studies, including Blaser et al. (2010), but
566 longer L for a given magnitude compared to Mai and Beroza (2000). Nevertheless, the
567 scaling of A is consistent with self-similar scaling (Somerville *et al*., 1999; Thingbaijam
568 and Mai, 2016).

569 Likewise, for subduction-interface events the comparison with previous studies
570 reveals an interesting pattern with more recent studies revealing longer W and L (Table
571 S3, Figure S11). In this respect, our new scaling relationships are close to those given by
572 Goda *et al*. (2016), and Skarlatoudis *et al*. (2016). However, our scaling relationship
573 between M_W and $\log_{10} W$ for subduction-interface events overall differs from the previous
574 studies. The scaling of L compares well with Leonard (2010), but predicts longer L
575 compared to Strasser *et al*. (2010) and Blaser *et al*. (2010). Considering scaling
576 relationships of A and W with respect to M_W (Skarlatoudis *et al*., 2016), we find that their
577 scaling relationship for L approximates the L-model (M_W–$\log_{10} L$ scaling with slope~0.7),
578 different to this study. The present study also corroborates self-similar scaling for A for
579 the subduction-interface events (*e.g*., Murotani *et al*., 2013; Thingbaijam and Mai, 2016;
580 Skarlatoudis *et al*., 2016).

581 For normal-faulting events, the new scaling coefficients suggest longer W, and
582 consequently larger A, compared to previous studies (Table S4, Figure S12). As the
583 scaling relationship given by Blaser *et al*. (2010) predicts longer L for a given magnitude,
584 we find that it predicts A similar to the new relationship, especially at larger magnitudes
585 (M_W>6.5). We note that the scaling relationships between M_W and A deviate from the self-
586 similar one, and can be attributed to slower growth of W with increasing M_W.

587 Regarding strike-slip events, for given magnitude the new empirical scaling laws
588 predict larger *W* than previous studies (Table S5, Figure S13). However, there is a
589 general agreement in the prediction of *L* with Wells and Coppersmith (1994) and Blaser
590 *et al*. (2010). The empirical scaling law for *L* is inclined towards the *L*-model, and hence
591 differs from Mai and Beroza (2000) and Leonard (2010). Our relations also differ from
592 those of Hanks and Bakun (2002, 2008) – although the authors adopted *L*-model scaling
593 – as we find that the scaling of *A* is not strongly affected by the finite seismogenic depth.
594 In our finding, the growth of *L* is more rapid, but that of *W* is restricted (but not saturated)
595 with the increasing M_W.

596 The differences between our current study and the work of Mai and Beroza
597 (2000) can be explained considering the computation of effective source dimensions. Mai
598 and Beroza (2000) computed the effective source dimensions based on the
599 autocorrelation widths of the along-strike- and down-dip averaged slip distribution. Here,
600 we apply adjustments to the autocorrelation width following Thingbaijam and Mai
601 (2016), which provide larger source dimensions. Additionally, the data used in the
602 present study significantly differs from Mai and Beroza (2000) in terms of magnitude
603 coverage and number of events.

604 To further compare with previous studies, not only the use of different datasets
605 needs to be accounted for, but also the regression techniques (including possible
606 constraints on the slope). The different regression techniques treat the errors-with-
607 variables either implicitly or explicitly (as discussed previously), however, whether or not
608 the estimated coefficients agree or differ statistically would depend largely on the data
609 scatter. For instance, Goda *et al*. (2016) obtained scaling coefficients using linear

610 regressions different from the present study based on GOR, although they used almost the
611 same dataset. Hence, these differences are due to the applied regression techniques.

612 In this context, we make a brief note on the regression techniques. GOR generally
613 provides a larger slope compared to ordinary least squares regression, depending on the
614 error variance ratio between two variables. For significantly smaller measurement errors
615 of x (compared to those of y), the slopes estimated by the two techniques could be
616 comparable. However, in the present analyses, measurement errors of x (*i.e.*, M_W) are
617 larger than those of y (*i.e.*, $\log_{10} W$ or $\log_{10} L$, as explained in Section Regression
618 Analysis). Nevertheless, a key factor in the contrasts between different regression
619 techniques would be wide data scatter. Narrowly scattered data would produce similar
620 regressions, irrespective of the applied techniques.

621 Similarly, our source-scaling relationships for strike-slip events deviate from that
622 of Blaser *et al*. (2010), possibly due to differences in the regression technique and/or the
623 absence of very-large events in their database. They applied orthogonal regression that
624 assumes a unit error-variance ratio of both variables (*e.g.*, M_W and $\log_{10} L$). However, the
625 definition of M_W implies that the measurement errors of M_W are larger than those for $\log_{10}$
626 L (or $\log_{10} W$), and hence the error-variance ratio is not unity. Thingbaijam and Mai
627 (2016) also used orthogonal regressions, but for regressions between $\log_{10} M_0$ and $\log_{10}$
628 A. In this regard, the present scaling laws supersede our previous ones. Nevertheless,
629 these differences do not affect the key results of Thingbaijam and Mai (2016) that
630 earthquake-slip distributions following a truncated-exponential law.

631 A closer agreement of our scaling relations with the ones given by Strasser *et al*.
632 (2010) could be due to more similar dataset, as they include rupture models from a

633 previous version of the SRCMOD database. We also note that Blaser *et al*. (2010) and
634 Leonard (2010) did not differentiate reverse-faulting events from shallow crustal and
635 subduction-interface events, but considered them as a single category. We attribute this
636 similarity in source-scaling coefficients (between shallow crustal and subduction-
637 interface events) to their datasets.
638
639 **Impact of Data used for Source-Inversions**
640 Different kinds of data and methods have been used in finite-fault source
641 inversions to generate the rupture models that eventually form the dataset used in our
642 study. Therefore, we examine how this affects model resolution and consequently the
643 effective source dimensions. Geodetic data (GPS and InSAR observations) are known to
644 have limited sensitivity to slip on the deeper parts of the faults (*e.g*., Page *et al*., 2009).
645 Similar limitations apply to near-field strong-motion data (*e.g*., Zhou *et al.* 2004).
646 Teleseismic recordings allow constraining the overall rupture properties at larger scales,
647 but are poor in resolving the temporal details. Strong-motion data help resolve the finer
648 details of the rupture process, but their spatial distribution strongly affects the inversion
649 results. Joint inversion (*e.g.*, combination of seismic and geodetic data) produces robust
650 rupture models, but often degrades the data fits for the individual datasets. These effects
651 on the rupture models require further evaluation, specifically in terms of possible bias
652 introduced by any of the source-inversion aspects.
653 Figure 9 displays box-plots that depict the distributions of the differences between
654 parameter values ($\log_{10} W$ and $\log_{10} L$) predicted by our empirical scaling laws and those
655 given by a specific rupture model. The rupture models are grouped according to four

656 broad data categories used in source inversions – strong-motion data, teleseismic
657 recordings, geodetic data (including tsunami data), and joint (combination of seismic and
658 geodetic data). Unlike the regression analyses, we perform this assessment on each
659 rupture model even if multiple source models exist for the same earthquake. Thus, the
660 box-plots capture both inter- and intra-event variability of the rupture models with respect
661 to the empirical scaling laws. For the empirical scaling laws, we anticipate that the inter-
662 event and intra-event variability are comparable in predicting the parameters required for
663 seismic hazard analysis. This conjecture is well attested by the observed intra-event
664 variability (Figures 5, 6, and 7, see also Gomberg *et al*., 2016), and from the exercises of
665 the source inversion validation project (Mai *et al*., 2016).

666 Figure 9 shows that the variability in estimates of $\log_{10} W$ and/or $\log_{10} L$ –
667 considering the entire range of the distribution (described by the box-plots) - increases
668 with the number of rupture models, and typically does not depend on the data used for the
669 inversions. Furthermore, the distributions between the first and third quartiles (*i.e*., 50%
670 of the data) generally overlap each other, indicating that statistically the different data
671 sets used in the inversions do not strongly affect the inferred source-scaling properties.
672 However, this observation does not hold for the geodetic inversions (of strike-slip
673 events), which provide smaller W compared to the seismic and joint inversions.
674 Nevertheless, with only six geodetic inversions (out of a total of 75 rupture models) for
675 the strike-slip events, the empirical scaling laws are hardly affected.

676

677 **Scaling of Oblique-slip Events**

678 When considering the dominant faulting types to classify the earthquake
679 mechanism, the presence of oblique-slip components is in many cases neglected. Here,

680 we examine three exceptional oblique-slip events that were excluded from the regression
681 analyses in terms of how the fit into the derived scaling relations (Fig. 10). The 2008
682 Wenchuan earthquake occurred on a thrust fault, initiated as reverse-faulting rupture, but
683 progressively transitioned into a strike-slip mode (Yagi *et al*., 2012; Fielding *et al*.,
684 2013). The estimated rupture dimensions of this event, especially *L*, follow the scaling
685 laws of strike-slip events. On the other hand, the estimated length *L* of the 1989 Loma
686 Prieta earthquake agrees with the scaling relationships for reverse-faulting events, while
687 the estimated *W* agrees more with strike-slip events than reverse-faulting ones. The 1978
688 Tabas earthquake, although classified as a thrust-faulting earthquake (Hartzell and
689 Mendoza, 1991), reveals a rupture length *L* consistent with the scaling of strike-slip
690 events, while its rupture width *W* is exceptionally large and does not match with the
691 scaling law. However, the estimated rupture dimensions for this event may be poorly
692 constrained.

693 An ad-hoc approach to emulate the scaling of *L* for oblique-slip events may be to
694 combine the scaling laws for different faulting types with appropriate weights. For
695 instance, strike-slip scaling of *L* would be more appropriate if rupture grows primarily
696 along strike, involving also strike-slip faulting, as observed during (or in) the Wenchuan
697 earthquake. Also, in case of steep fault-dip ($\delta \geq 70°$), the scaling of *W* for strike-slip
698 events would be more applicable to account for restricted growth of *W* (with increasing
699 M_W) due to the finite seismogenic depth. Thus, we find that the source-scaling laws for
700 the dominant faulting types can be used to describe the source parameters of oblique-slip
701 events.
702

Scaling of Fault-segments

Large earthquakes, especially those on strike-slip faults, are typically associated with along-strike rupturing of multiple fault-segments. The characteristics of fault-segments play an important role for rupture propagation and arrest, slip distributions and source-scaling properties (Manighetti *et al*., 2005, 2007; Wesnousky, 2006, 2008; Kase, 2010; Wesnousky and Biasi, 2011; Carpenter *et al*., 2012). Here, we analyze the rupture models for the scaling behavior of their along-strike fault-segments in terms of relationships between segment-specific width W^S, length L^S, area A^S, and moment magnitude M_W^S, calculated for each fault-segment individually.

The bulk of rupture models with along-strike segmentation belongs to strike-slip regimes, with 14 events (out of which 13 are continental events). For other faulting regimes, the models available comprise only three reverse-faulting events, a subduction-interface event, and three normal slip events (two of which occurred at depth>50 km). Owing to the data availability, we focus on the continental strike-slip events. As such, along-strike fault segmentation is far more common with strike-slip events compared to other faulting regimes.

Figure 11 illustrates an example for the computation of source parameters specific to each fault-segment. Note that we compute effective source dimensions for each fault-segment in the same manner as for single-segment rupture models. As discussed previously, the slip distributions generally taper to zero (or very low slip values) at the fault edges. For multi-segment faults, this slip-tapering behavior can be expected at fault-segments associated with rupture terminations. Therefore, we classify the fault-segment into two groups: exterior (associated with rupture terminations) and interior ones.

726 Furthermore, we avoid direct regressions (due to the small sample size), and apply
727 both empirical and theoretical constraints on the slope to avoid bias also due to multiple
728 rupture models for the same events. Therefore, we investigate whether the relationships
729 for fault-segment based source parameters are consistent with those for the entire rupture
730 (that is, combining all fault-segments), or whether they conform to either self-similar
731 scaling or *W*-model scaling.

732 Figure 12 shows that the relationships between M_W^S and W^S are very similar to the
733 scaling relationship for the overall rupture width. However, we observe that W^S tends to
734 saturate for larger magnitudes (M_W^S>7.0). On the other hand, the scaling of L^S with
735 respect to M_W^S indicates that fault-segments have significantly shorter rupture length (L^S)
736 for a given moment magnitude compared to that given by the scaling law for overall
737 rupture length. Furthermore, for the same M_W^S, exterior fault-segments show larger L^S
738 than the interior ones, consistent with slip-tapering behavior at the rupture terminations.
739 However, we find that the scaling of L^S with M_W^S for the interior fault-segments is
740 consistent with the *W*-model scaling (slope ~1.0; Leonard, 2010), in agreement with the
741 saturation of W^S.

742 Therefore, the scaling behavior is better explained by relationships between M_W^S
743 and $\log_{10} A^S$. The entire rupture-area, for a given magnitude (*i.e.*, $M_W = M_W^S$), is ~1.8
744 times larger than the exterior fault-segment area (for the same magnitude), and ~3.1 times
745 larger than the interior fault-segment area (for the same magnitude). Thus, fault-segments
746 (both exterior and interior) accommodate significantly larger average slips per segment-
747 length, and consequently also over the segment-area, compared to the total average slip
748 over the entire fault. One possible explanation for this observation is that segmented

faults have higher strength since joints or kinks behave as barriers, which require higher stress level to break.

Discussions

Next, we discuss the implications of the proposed scaling laws on earthquake mechanics, focusing on the differences of source-scaling properties and variability of average stress-drop across different faulting regimes. Additionally, we appraise the new empirical scaling laws in terms of their practical applications.

Variability of Source-scaling Properties

Our analysis reveals that source-scaling properties for different faulting regimes show statistically significant differences (Figs. 4, 5, and 6). These differences are exhibited through the variability of the average fault-aspect ratios (L/W), as shown in Figure 13. A power-law relationship between L and W is naturally given by the scaling of L and W with respect to M_W, such that $L \propto W^{\beta}$. Our observed variability in this relationship contradicts with Leonard (2010), who proposed β ~1.5, irrespective of faulting style (except for width-saturated strike-slip events). We observe that the average power-index β varies from 1.3 (for reverse-faulting shallow crustal events), 1.5 (for normal-faulting events) and 1.6 (for subduction-interface) to 2.6 (for strike-slip events).

A consistent observation is that L grows more rapidly than W with increasing M_W. This feature is most prominent for strike-slip events. A possible physical explanation for this observation is non-uniform distribution of frictional resistance (fault strength) and stress concentrations (*e.g.*, Rivera and Kanamori, 2002). The influence of varying fault-

772 strength on source-scaling properties has been often discussed (*e.g*., Das and Scholz,
773 1983; Strehlau, 1986; Bodin and Brune, 1996; Mai and Beroza, 2000; Shaw and Scholz,
774 2001; Miller, 2002; Wesnousky, 2006; Lozos *et al*., 2015). The fault-strength tends to
775 increase with depth, which in turn would restrict down-dip seismic slip (Das and Scholz,
776 1983; Strehlau, 1986). On the other hand, longer ruptures are associated with along-strike
777 zones of low fault-strength or high shear stress (Wesnousky, 2006; Lozos *et al*., 2015).

778 Another argument for the differences in the scaling of fault-aspect ratio relates to
779 the finite seismogenic depth, and hence is a manifestation of the *W*-model. The scaling of
780 fault-aspect ratio correlates with average fault-dip, which is steepest for strike-slip events
781 ($\delta \sim 70°–90°$) and shallowest for subduction-interface events ($\delta \sim 10°–30°$). The impact
782 of seismogenic depth on the scaling relationships would depend on the average fault-dip
783 such that steeper faults are more affected. Figure 14 depicts the ratio between $\log_{10} L$ and
784 $\log_{10} W$ (considering a power-law relationship between the two parameters) with respect
785 to fault-dip angles. Figure S14 provides a similar plot but between $\log_{10} L/W$ and fault-
786 dip angles. In general, fault-aspect ratio tends to increase with earthquake magnitude. We
787 consider only large events ($M_W \geq 7.0$), and find an overall positive correlation between the
788 fault-aspect ratio and fault-dip angles – for steeper faults, the aspect ratio is larger. Thus,
789 it could be combination of these factors (favorably aligned frictional strength, and effects
790 of finite seismogenic depth) that control the scaling of fault-aspect ratio.

791 Apart from the differences in the fault-aspect ratio, we find that for a given
792 magnitude the subduction-interface events show larger *W* than other faulting regimes
793 (Figure 4). Obviously, subduction-interface zones tend to reach larger rupture width,
794 possibly due to the gentle fault-dip, relatively higher tectonic stress on the fault indicated

795 by more frequent seismic activity (*e.g.*, Schorlemmer *et al.*, 2005), and the thermal and
796 structural properties (*e.g.*, Hyndman *et al.*, 1995; Oleskevich *et al.*, 1999).

797 Another consistent observation is that empirical scaling laws between M_W and A
798 generally agree with self-similar scaling, except for normal-faulting events. As noted
799 earlier, this scaling is consistent with the expectation from a circular shear-crack
800 (Kanamori and Anderson, 1975; Hanks and Bakun, 2002). Most of the earlier studies
801 combined reverse and normal dip-slip events into a single faulting regime (*e.g.*, Mai and
802 Beroza, 2000; Henry and Das, 2001; Leonard, 2010; Yen and Ma, 2011). Here, we
803 differentiate between normal and reverse dip-slip earthquakes whose rupture mechanisms
804 are distinctly different due to the acting tectonic stress regime (reverse: upward
805 dislocation of the hanging wall associated with crustal shortening; and normal faulting:
806 down-dip collapse of the hanging wall resulting in crustal extension). Additionally,
807 normal-faulting earthquakes generally occur on steeper fault (δ~50°–60°) compared to
808 reverse-faulting earthquakes (δ~ 40°–50°). Consequently, the variations in source-scaling
809 properties between normal and reverse dip-slip earthquakes are driven by a combination
810 of geometrical effects and acting stresses.

811 The inhibited growth of W for normal-faulting events is not accompanied by rapid
812 growth of L, as observed for strike-slip events. However, normal-faulting earthquakes are
813 more often associated with listric faults (whose dip decreases with increasing depth) than
814 other faulting regimes. In this context, either the scaling relationship for W requires
815 correction for the down-dip geometrical complexity of the fault, or slip is negligible at
816 the deeper parts of listric faults due to increasingly shallower fault-dip (*e.g.*, Williams and
817 Vann, 1987). These aspects warrant further research; however, a few recent studies of

818 listric faults suggest that slip is insignificant at deeper parts of the fault where fault-dip is
819 almost horizontal (*e.g.*, Zhang *et al.*, 2010; Fielding *et al.*, 2013; Jolivet *et al.*, 2014).

820 For strike-slip earthquakes, the expected saturation of *W*, and hence the proposed
821 *W*-model scaling, is not observed (*e.g.*, Scholz, 1982; Romanowicz, 1992), although a
822 finite seismogenic depth would predict such behavior. However, there is considerable
823 variation of seismogenic depth globally, depending on the seismotectonics of the region,
824 which could obfuscate any *W*-scaling. Note also that regional variations of seismogenic
825 depth correlate with observed maximum earthquake magnitude (Martínez-Garzón *et al.*,
826 2015). It has been also suggested that large strike-slip earthquakes may penetrate deeper
827 than the seismogenic layer, albeit at lower slip-rates and with smaller moment release,
828 driven by the particular rupture dynamics (Shaw and Scholz, 2001; Shaw and
829 Wesnousky, 2008; Jiang and Lapusta, 2016). Therefore, *W*-model scaling may not be
830 immediately apparent for a global dataset, but it may be discernable at regional scale. We
831 will return to this aspect in the context of applicability of the scaling laws.

832

833 **Variability of Average Stress-drop**

834 Our observed source-scaling properties suggest that subduction-interface
835 earthquakes are associated with lower average static stress-drop than earthquakes of other
836 faulting regimes (especially shallow crustal reverse-faulting events). In case of strike-slip
837 and normal-faulting events, *W* grows slowly but *D* grows faster with increasing M_W,
838 which implies that smaller magnitude events have lower stress-drop than larger
839 earthquakes. The inferred variability of stress-drop conforms to the scaling differences
840 between intraplate and interplate earthquakes, and also to the dependence of stress-drop

of the faulting regimes (*e.g.*, Scholz *et al*., 1986; Mai and Beroza, 2000; Allmann and Shearer, 2009; Konstantinou, 2014), as for instance between shallow crustal reverse-faulting (dominantly intraplate) and subduction-interface (interplate) events.

To investigate scale-dependence of average stress-drop, we consider that the static stress-drop for a uniform stress-drop shear crack can be defined as,

$$\Delta\sigma = C\mu\frac{D}{L_c} \qquad (10)$$

where L_C is a characteristic length (usually the smallest dimension, hence typically W) of the earthquake, and C is a constant of order unity (Kanamori and Anderson, 1975). However, the length scales that control $\Delta\sigma$ for the actual rupture (also as imaged by the source-inversions) are expected to be shorter than the length or width or the entire rupture, owing to the spatially variable slip. Therefore, $\Delta\sigma$ given by Eq. (10) serves as an approximation to understand source-scaling properties, but not as an accurate measure of the stress change occurring during the earthquake.

Figure 15 depicts distributions of D/W over M_W for the different faulting types; the quantity D/W is related to the strain change, and is regarded as a proxy for $\Delta\sigma$ (Eq. 10). We find that for the reverse-faulting events D/W is almost independent of M_W, indicating scale invariant $\Delta\sigma$. The figure also provides strong evidence of lower $\Delta\sigma$ for subduction-interface events, compared to other faulting types. At the same time, we observe an apparent increase of the stress-drop proxy with magnitude. However, this pattern could be due to paucity of data at higher magnitude (M_W> 8.5). Furthermore, considerable variability exists for $\Delta\sigma$ across different subduction zones and even across

different segments of a subduction-interface (*e.g.*, Seno, 2014). Thus, the scale invariance property of $\Delta\sigma$ for subduction-interface events cannot be concluded.

We remark that Bilek and Lay (1999) observed that constant stress drop of earthquakes in subduction zones can be derived by considering depth-variability of crustal rigidity. Ripperger and Mai (2004) also discussed the effect of depth-dependent rigidity such that absolute stress-changes decrease in the uppermost low-strength part of the fault. More recently, Ye *et al*. (2016) considered depth-dependent rigidity in source inversions for mega-thrust events in subduction zones. They observed that $\Delta\sigma$ associated with subduction-interface events does not correlate with earthquake magnitude. Thus, there are complications in relating slip, stress-drop, and seismic moment, especially for near-surface rupture in subduction zones where the rigidity could be significantly small.

On the other hand, a positive correlation can be observed between the stress-drop proxy and magnitude, for the normal-faulting and strike-slip events. In case of normal-faulting events, this positive correlation provides strong evidence of increasing $\Delta\sigma$, and could be related to the restricted growth of W with M_W. This inference is in line with observations of $\Delta\sigma$ increasing with M_W made by recent studies on normal-faulting earthquakes (*e.g.*, Calderoni *et al*., 2013; Konstantinou, 2014; Pacor *et al*., 2016).

It is also important to note that the free-surface effect (when the rupture is close to the free-surface) may cause relatively large slip, especially for ruptures on near-vertical faults (Archuleta and Frazier, 1978; Brune and Anooshehpoor, 1998; Shi *et al*., 2003). Such cases can be accounted for using a mirror image of the slip distribution above the free surface (Steketee, 1958) in the stress-change calculations, which results in small stress differences of 1 - 2 % (Ripperger and Mai, 2004).

887 Based on fundamental relationship between magnitude and radiated energy,
888 Kanamori and Riviera (2004) argued that stress drop is necessarily scale-dependent.
889 Previously, Mai and Beroza (2000) reported that scale-dependent behavior of the average
890 stress-drop for strike-slip events could be gleaned from a small database of rupture
891 models. Abercrombie and Rice (2005) also observed that stress drop increases slightly
892 with earthquake size. Mai *et al*. (2006) made similar observations based on dynamic
893 rupture simulations. Likewise, Dalguer *et al*. (2008) studied dynamic simulations and
894 reported that the average stress drop is independent of earthquake size for buried
895 earthquakes, but scale dependent for surface-rupturing earthquakes. From assessment of
896 kinematic rupture models, Causse *et al.* (2014) also observed that stress-drop tends to
897 increase with magnitude. More recently, Archuleta and Ji (2016) also suggested possible
898 weak scaling of stress-drop with earthquake magnitude.

899 The scale-dependent $\Delta\sigma$ can be linked to scaling of D such that it increases with
900 L, and therefore complies with L-model scaling. It has been suggested that large ruptures
901 on long and narrow faults require higher stress-drop to propagate (Heaton, 1990; Mai and
902 Beroza, 2000). Our observation of larger D, and therefore larger $\Delta\sigma$, within fault-
903 segments compared to single-segment rupture (Fig. 12) supports this conjecture.
904 Dynamic rupture simulations also indicate that fault interactions (*e.g.*, ruptures on
905 multiple fault segments) result in higher $\Delta\sigma$ at each fault-segment (Kase, 2010).
906 However, we note that if W saturates then the scaling of L becomes more consistent with
907 the W-model, weakening the correlation between D and L.

908 Average stress-drop is strongly connected with source scaling properties: a
909 constant or scale-invariant $\Delta\sigma$ implies self-similar earthquake source scaling. Our result

910 of $\Delta\sigma$ being positively correlated with M_W is consistent with observed departures from
911 self-similar earthquake scaling. This scale-dependent behavior implies an upper limit of
912 average stress-drop once the maximum possible magnitude is reached for a given fault
913 system. On the other hand, the inferred variability of $\Delta\sigma$ across different faulting regimes
914 may indicate corresponding differences in the slip heterogeneity (Liu-Zeng *et al*., 2005),
915 the underlying fault-strength and roughness of the fault-surface (Miller, 2002; Candela *et*
916 *al*., 2011) and the slip accumulation rate (Anderson *et al*., 1996). These factors may be
917 interrelated, and are being actively investigated (*e.g*., Zielke *et al*., 2017).
918
919 **Applying the Scaling Laws**
920 Let us focus now on the practical aspects of empirical scaling laws. Owing to the
921 use of general orthogonal regressions, our relationships are invariant under interchange of
922 variables. Therefore, the same relationship can be applied to predict either of the two
923 variables; for instance, $\log_{10} L$ can be predicted from M_W, and likewise, M_W from $\log_{10} L$.
924 In deciding a specific relationship, it is not only important to consider the
925 underlying faulting regimes, but also the applicable data range (magnitude, length, width
926 and area) listed in Table 1. However, for smaller magnitudes that are not well represented
927 in the database used in this study (approximately $M_W < 5.5$ for strike-slip, normal-faulting
928 and reverse-faulting earthquakes, and $M_W < 7.0$ for subduction-interface earthquakes), we
929 suggest that self-similar scaling is applicable based on M_W-$\log_{10} A$ (for instance,
930 Kanamori and Anderson, 1975).
931 We find that an important discriminating feature between shallow crustal reverse
932 faulting events and subduction-interface events is the average fault-dip. The average

933 fault-dip is significantly shallower in the former faulting regime (Figs. 1 and 14). This
934 distinction is important in deciding the pertinent scaling laws.

935 For mega-thrust (M_W > 8.5) subduction events, potential constraints of finite
936 seismogenic depth on the down-dip rupture-width can be achieved by adopting higher
937 confidence on the scaling relationship between M_W and $\log_{10} A$, thereby overruling the
938 scaling between M_W and $\log_{10} L$. In the light of the remarkable 2011 Tohoku earthquake,
939 the possibility of very high $\Delta\sigma$ may be considered (taking into account - subduction
940 geometry, convergence rate, age and temperature of the subducting plate; Fry and Ma,
941 2016). Accordingly, the scaling laws for shallow crustal reverse-faulting events or those
942 given by Goda *et al*. (2016) for tsunamigenic events could be applied to predict
943 exceptionally large M_W from smaller rupture dimensions (or vice versa), in combination
944 with those for subduction-interface events using suitable weights.

945 For strike-slip earthquakes, the empirical relationship between M_W and $\log_{10} L$ are
946 more consistent with the *L*-model, and would allow for more conservative estimates of
947 M_W from *L*. However, for the regions where the distribution of seismogenic depth is well
948 established (*e.g*., Nazareth and Hauksson, 2004), and the upper limit of *W* can be fixed,
949 the scaling relationship between M_W and $\log_{10} A$ can be applied. With increasing M_W, the
950 scaling of *L* becomes more aligned to the *W*-model (*e.g*., Leonard, 2010). This
951 consideration also applies to the scaling of fault-segments associated with strike-slip
952 events.

953

954

955

Conclusions

We developed new empirical scaling laws for earthquake-rupture geometry based on a large database of finite-fault rupture models, containing earthquake source models over a wide magnitude range (from M_W 5.4 to M_W 9.2). Our study provides important updates on earthquake source-scaling laws, addressing a primary concern for improving seismic-tsunami hazard analysis and engineering applications.

Being empirical, the scaling laws preserve the complexities manifested by the data, and allow correspondingly for physical interpretations. We observe that rupture length grows more rapidly with magnitude compared to rupture width. On the other hand, subduction-interface earthquakes have significantly larger rupture width (and therefore rupture area), compared to other faulting regimes. On the global scale, the saturation of rupture width is not evident with large strike-slip earthquakes, but inhibited growth of rupture width with magnitude can be perceived. In this case, rupture length exhibits a scaling behavior that is implied by the *L*-model. However, at regional scales where seismogenic depth is more or less fixed, the scaling behavior close to the *W*-model is expected. In general, the scaling of rupture area agrees with self-similar scaling behavior, except for normal-faulting events. Interestingly, the scaling laws imply a strong likelihood of scale-dependent average stress-drop, especially with normal-faulting and strike-slip events.

Finally, we note that there are statistically significant differences amongst the source-scaling properties of the different faulting regimes. Such differences are consistent with the variability of geological and seismological factors (*e.g.*, fault-dip, fault-strength, stress-drop and rupture mechanics) across different faulting regimes.

Data and Resources

The rupture models used in this study were extracted from the SRCMOD database (http://equake-rc.info/srcmod, last accessed December 2016). The dataset provided by Blaser *et al.* (2010) is available in the electronic supplement of their article.

Acknowledgements

We are thankful to all our colleagues for sharing their rupture models with the SRCMOD database. It is due to their generosity that the present and similar studies are possible. Careful and constructive comments by Shiro Hirano, and two anonymous reviewers helped improve the manuscript. The research presented in this article is supported by King Abdullah University of Science and Technology (KAUST) in Thuwal, Saudi Arabia by grants BAS/1/1339-01-1 and URF/1/2160-01-01.

References

Abercrombie, R. E., and J. R. Rice (2005). Can observations of earthquake scaling constrain slip weakening? *Geophys. J. Int.* **162**, 406–424.

Aki, K. (1966). Generation and propagation of G waves from the Niigata earthquake of June 16, 1964: Part 2. Estimation of earthquake moment, released energy and stress drop from the G wave spectra, *Bull. Earthq. Res. Inst., Univ. Tokyo* **44**, 73–88.

Allmann, B. B., and P. M. Shearer (2009). Global variations of stress drop for moderate to large earthquakes, *J. Geophys. Res*. **114**, doi: 10.1029/2009JB005821.

Anderson, J.G., S. G., Wesnousky, and M. W. Stirling (1996). Earthquake size as a function of fault slip rate. *Bull. Seismol. Soc. Am*. **86**, 683–690.

1003 Archuleta, R. J., and G. A. Frazier (1978). Three-dimensional numerical simulation of
1004 dynamic faulting in a half-space, *Bull. Seismol. Soc. Am*. **68**, 541–572.
1005 Archuleta, R. J., *and* C. Ji (2016). Moment rate scaling for earthquakes $3.3 \leq M \leq 5.3$ with
1006 implications for stress drop, *Geophys. Res. Lett.* **43**, 12004–12011,
1007 *doi:*10.1002/2016GL071433.
1008 Avouac, J.P., F. Ayoub, S. Wei, J.P. Ampuero, L. Meng, S. Leprince, R. Jolivet, Z.
1009 Duputel, and D. Helmberger (2014). The 2013, Mw 7.7 Balochistan earthquake,
1010 energetic strike-slip reactivation of a thrust fault. *Earth Planet. Sci. Lett.* **391**, 128–
1011 134.
1012 Beresnev, I.A. (2003). Uncertainties in finite-fault slip inversions: to what extent to
1013 believe? (a critical review). *Bull. Seismol. Soc. Am.* **93**, 2445–2458.
1014 Bilek, S. L. and T. Lay (1999). Rigidity variations with depth along interplate megathrust
1015 faults in subduction zones, *Nature* **400**, 443–446.
1016 Blaser, L., F. Krüger, M. Ohrnberger, and F. Scherbaum (2010). Scaling relations of
1017 earthquake source parameter estimates with special focus on subduction environment.
1018 *Bull. Seismol. Soc. Am.***100**, 2914–2926.
1019 Bodin, P., and J. N. Brune (1996). On the scaling of slip with rupture length for shallow
1020 strike-slip earthquakes: quasistatic models and dynamic rupture propagation, *Bull.*
1021 *Seismol. Soc. Am.* **86**, 1292–1299.
1022 Bonilla, M. G., R.K. Mark and J.J. Lienkaemper (1984). Statistical relations among
1023 earthquake magnitude, surface rupture length, and surface fault displacement. *Bull.*
1024 *Seismol. Soc. Am*. **74**, 2379–2411.

1025 Brune, J. N., and A. Anooshehpoor (1998). A physical model of the effect of a shallow
1026 weak layer on strong ground motion for strike-slip ruptures, *Bull. Seismol. Soc. Am.*
1027 **88**, 1070–1078.
1028 Calderoni, G., Rovelli, A. and Singh, S.K. (2013). Stress drop and source scaling of the
1029 2009 April L'Aquila earthquakes. *Geophys. J. Int.* **192**, 260–274.
1030 Candela, T., F. Renard, M. Bouchon, J. Schmittbuhl, and E.E. Brodsky (2011). Stress
1031 drop during earthquakes: effect of fault roughness scaling. *Bull. Seismol. Soc. Am.*
1032 **101**, 2369-2387.
1033 Carpenter, N.S., S.J. Payne, and A.L. Schafer (2012). Toward reconciling magnitude
1034 discrepancies estimated from paleoearthquake data. *Seism. Res. Lett.* **83**, 555–565.
1035 Carroll, R.J., and D. Ruppert (1996). The use and misuse of orthogonal regression
1036 estimation in linear errors-in-variables models, *The American Statistician* **50**, 1–6.
1037 Castellaro, S., F. Mulargia, and Y.Y Kagan (2006). Regression problems for magnitudes,
1038 *Geophys. J. Int.* **165**, 913–930.
1039 Causse, M., L. A. Dalguer, and P. M. Mai (2014) Variability of dynamic source
1040 parameters inferred from kinematic models of past earthquakes. *Geophys. J Int.* **196**,
1041 1754–1769.
1042 Dalguer, L.A., H. Miyake, S.M. Day, and K. Irikura (2008). Surface rupturing and buried
1043 dynamic-rupture models calibrated with statistical observations of past earthquakes.
1044 *Bull. Seismol. Soc. Am*. **98**, 1147–1161.
1045 Das, S., and C. Scholz (1983). Why large earthquakes do not nucleate at shallow depths.
1046 *Nature* **305**, 621–623.

1047 De Risi, R., and K. Goda (2016). Probabilistic earthquake-tsunami multi-hazard analysis:
1048 application to the Tohoku region, Japan, *Front. Built Environ.* **2**, 25, doi:
1049 10.3389/fbuil.2016.00025.
1050 Efron B. (1982). *The jackknife, the bootstrap, and other resampling plans*, Society for
1051 Industrial and Applied Mathematics, Philadelphia, doi:
1052 http://dx.doi.org/10.1137/1.9781611970319.
1053 Fielding, E. J., A. Sladen, Z. Li, J.-P. Avouac, R. Bürgmann, and I. Ryder (2013).
1054 Kinematic fault slip evolution source models of the 2008 M7.9 Wenchuan earthquake
1055 in China from SAR interferometry, GPS and teleseismic analysis and implications for
1056 Longmen Shan tectonics. *Geophys. J. Int.* doi:10.1093/gji/ggt155.
1057 Fry, B. and K. F. Ma (2016). Implications of the great Mw 9.0 Tohoku-Oki earthquake
1058 on the understanding of natural hazard in Taiwan and New Zealand, *Seism. Res. Lett.*
1059 **87**, 1254–1258.
1060 Fuller, W. A. (1987). *Measurement error models.* John Wiley & Sons, New York
1061 Galvez, P., L.A. Dalguer, J.P. Ampuero, and D. Giardini (2016). Rupture reactivation
1062 during the 2011 Mw 9.0 Tohoku earthquake: dynamic rupture and ground-motion
1063 Simulations, *Bull. Seismol. Soc. Am.* **106**, 819–831.
1064 Geller, R.J. (1976). Scaling relations for earthquake source parameters and magnitudes,
1065 *Bull. Seismol. Soc. Am.* **66**, 1501–1523.
1066 Ghasemi, A. and S. Zahediasl (2012). Normality tests for statistical analysis: a guide for
1067 non-statisticians, *Int. Jour. Endo. Meta.* **10**, 486–489.

1068 Goda, K., T. Yasuda, N. Mori, and T. Maruyama (2016). New scaling relationships of
1069 earthquake source parameters for stochastic tsunami simulation, *Coast. Eng. Jour*. **58**,
1070 doi: http://dx.doi.org/10.1142/S0578563416500108
1071 Gomberg, J., A. Wech, K. Creager, K. Obara, and D. Agnew (2016). Reconsidering
1072 earthquake scaling, *Geophys. Res. Lett.* **43**, 6243–6251, doi:10.1002/2016GL069967.
1073 Hanks, T. C., and H. Kanamori (1979). A moment magnitude scale, *J. Geophys. Res*.,
1074 **84**(B5), 2348–2350, doi:10.1029/JB084iB05p02348.
1075 Hanks, T. C., and W. H. Bakun (2002). A bilinear source-scaling model for M-log A
1076 observations of continental earthquakes, *Bull. Seismol. Soc. Am.* **92**, 1841–1846.
1077 Hanks, T. C., and W. H. Bakun (2008). M-log A observations of recent large
1078 earthquakes. *Bull. Seismol. Soc. Am.* **98**, 490–494.
1079 Hartzell, S., and C. Mendoza (1991). Application of an iterative least-squares wave-form
1080 inversion of strong-motion and teleseismic records to the 1978 Tabas, Iran,
1081 Earthquake. *Bull. Seismol. Soc. Am* **81** (2), 305–331.
1082 Heaton, T.H. (1990). Evidence for and implications of self-healing pulses of slip in
1083 earthquake rupture. *Phys. Earth and Planet. Int*. **64**, 1-20.
1084 Henry, C., and S. Das (2001). Aftershock zones of large shallow earth- quakes: fault
1085 dimensions, aftershock area expansion and scaling relations, *Geophys. J. Int.* **147**,
1086 272–293.
1087 Henry, C., S. Das, and J. H. Woodhouse (2000). The great March 25, 1998, Antarctic
1088 Plate earthquake: moment tensor and rupture history, *J. Geophys. Res.* **105**, 16097–
1089 16119.

1090 Herrendörfer, R., Y. van Dinther, T. Gerya, and L. A. Dalguer (2015). Earthquake
1091 supercycle in subduction zones controlled by the width of the seismogenic zone. *Nat.*
1092 *Geosci.* **8**, 471–474.
1093 Hyndman, R.D., K, Wang and M. Yamano (1995). Thermal constraints on the
1094 seismogenic portion of the southwestern Japan subduction thrust, *Jour. Geophys. Res*.
1095 **100**, 15373–15392.
1096 Jiang, J., and N. Lapusta (2016) Deeper penetration of large earthquakes on seismically
1097 quiescent faults, *Science* **352**, 1293–1297.
1098 Johnston, A. C., and L. R. Kanter (1990). Stable continental earthquakes. *Sci. Am.* 262,
1099 68–75.
1100 Jolivet, R., Z. Duputel, B. Riel, M. Simons, L. Rivera, S. E. Minson, H. Zhang, M.A.G.
1101 Aivazis, F. Ayoub, S. Leprince, S. Samsonov,(2014). The 2013 Mw 7.7 Balochistan
1102 earthquake: Seismic potential of an accretionary wedge. *Bull. Seismol. Soc. Am* **104**,
1103 1020–1030.
1104 Kanamori, H. and K. C. McNally (1982). Variable rupture mode of the subduction zone
1105 along the Ecuador-Colombia coast. *Bull. Seism. Soc. Am* **72**, 1241–1253.
1106 Kanamori, H., and D. L. Anderson (1975). Theoretical basis of some empirical relations
1107 in seismology. *Bull. Seismol. Soc. Am.* **65**, 1073–1095.
1108 Kanamori, H. and L. Rivera (2004). Static and dynamic scaling relations for earthquakes
1109 and their implications for rupture speed and stress drop. *Bull. Seismol. Soc. Am.* **94**,
1110 314–319.
1111 Kase, Y. (2010). Slip-length scaling law for strike-slip multiple segment earthquakes
1112 based on dynamic rupture simulations. *Bull. Seismol. Soc. Am* **100**, 473–481.

1113 King, G.C. and S.G. Wesnousky (2007). Scaling of fault parameters for continental
1114 strike-slip earthquakes. *Bull. Seismol. Soc. Am* **97**, 1833–1840.
1115 Konstantinou, K.I. (2014). Moment magnitude–rupture area scaling and Stress-drop
1116 Variations for earthquakes in the Mediterranean region. *Bull. Seismol. Soc. Am*. **104**,
1117 2378–2386.
1118 Konstantinou, K.I., G.A. Papadopoulos, A. Fokaefs and K. Orphanogiannaki (2005).
1119 Empirical relationships between aftershock area dimensions and magnitude for
1120 earthquakes in the Mediterranean sea region, *Tectonophysics* **403**, 95–115
1121 Lee, S.-J., B.-S. Huang, M. Ando, H.-C. Chiu, and J.-H. Wang (2011). Evidence of large
1122 scale repeating slip during the 2011 Tohoku-Oki earthquake, *Geophys. Res. Lett*. **38**,
1123 L19306, doi:10.1029/2011GL049580.
1124 Leonard, M. (2010). Earthquake fault scaling: relating rupture length, width, average
1125 displacement, and moment release. *Bull. Seismol. Soc. Am*. **100**, 1971–1988.
1126 Leonard**,** M. (2014). Self-consistent earthquake fault-scaling relations: update and
1127 extension to stable continental strike-slip faults, *Bull. Seismol. Soc. Am* **104**, 2953–
1128 2965.
1129 Lilliefors, H. W. (1967). On the Kolmogorov-Smirnov test for normality with mean and
1130 variance unknown, *Jour. Am. Stat. Assoc*. **62**, 399–402.
1131 Liu-Zeng, J., T. Heaton, and C. DiCaprio (2005). The effect of slip variability on
1132 earthquake slip-length scaling, *Geophys. J. Int.* **162**, 841–849.
1133 Llenos, A. L., and J. J. McGuire (2007). Influence of fore-arc structure on the extent of
1134 great subduction zone earthquakes, *J. Geophys. Res*. **112**, B09301,
1135 doi:10.1029/2007JB004944.

1136 Lozos, J. C., D. D. Oglesby, J. N. Brune, and K. B. Olsen (2015). Rupture and ground-
1137 motion models on the northern San Jacinto fault, incorporating realistic complexity.
1138 *Bull. Seismol. Soc. Am*. **105**, 1931–1946.
1139 Mai, P. M., and G. C. Beroza (2000). Source scaling properties from finite-fault-rupture
1140 models. *Bull. Seismol. Soc. Am*. **90**, 604–615.
1141 Mai, P. M., and K. K. S. Thingbaijam (2014). SRCMOD: an online database of finite-
1142 fault rupture models. *Seism. Res. Lett.* **85**, 1348–1357.
1143 Mai, P. M., D. Schorlemmer, M. Page, J- P. Ampuero, K. Asano, M. Causse, S. Custodio,
1144 W. Fan, G. Festa, M. Galis, *et al*. (2016). The earthquake-source inversion validation
1145 (SIV) project. *Seism*. *Res*. *Lett*. **87**, doi: 10.1785/0220150231.
1146 Mai, P. M., P. Somerville, A. Pitarka, L. Dalguer, S. Song, G. Beroza, H. Miyake, and K.
1147 Irikura (2006). On scaling of fracture energy and stress drop in dynamic rupture
1148 models: Consequences for near-source ground-motions. *Earthquakes: Radiated*
1149 *Energy and the Physics of Faulting, Geophysical Monograph Series, American*
1150 *Geophysical Union* **170**, 283–293.
1151 Mai, P. M., P. Spudich and J. Boatwright (2005). Hypocenter locations in finite-source
1152 rupture models. *Bull. Seismol. Soc. Am.* **95**, 965–980.
1153 Mai, P.M., J. Burjanek, B. Delouis, G. Festa, C. Francois-Holden, D. Monelli, T. Uchide,
1154 and J. Zahradnik (2007). Earthquake source inversion blindtest: Initial results and
1155 further developments, *Eos Trans. AGU* 88, no. 52, Fall Meet. Suppl., Abstract S53C-
1156 08.

1157 Manighetti, I., M. Campillo, C. Sammis, P. M. Mai, and G. King (2005), Evidence for
1158 self-similar, triangular slip distributions on earthquakes: Implications for earthquake
1159 and fault mechanics, *J. Geophys. Res*., **110**, B05302, doi:10.1029/2004JB003174.
1160 Manighetti, I., M. Campillo, S. Bouley, and F. Cotton (2007). Earthquake scaling, fault
1161 segmentation, and structural maturity. *Earth Planet. Sci. Lett.* **253**, 429-438.
1162 Martínez-Garzón, P., M. Bohnhoff, Y. Ben-Zion, and G. Dresen (2015). Scaling of
1163 maximum observed magnitudes with geometrical and stress properties of strike-slip
1164 faults, *Geophys. Res. Lett.* **42**, doi:10.1002/ 2015GL066478.
1165 Miller, S.A. (2002). Earthquake scaling and the strength of seismogenic faults,
1166 *Geophysis. Res. Lett.* **29**, doi:10.1029/2001GL014181.
1167 Murotani, S., H. Miyake, and K. Koketsu (2008). Scaling of characterized slip models for
1168 plate-boundary earthquakes. *Earth, planets and space* **60**, 987–991.
1169 Murotani, S., K. Satake and Y. Fujii (2013). Scaling relations of seismic moment, rupture
1170 area, average slip, and asperity size for M~ 9 subduction-zone earthquakes. *Geophys.*
1171 *Res. Lett.* **40**, 5070–5074.
1172 Nazareth, J.J. and E. Hauksson (2004). The seismogenic thickness of the southern
1173 California crust, *Bull. Seismol. Soc. Am.* **94**, 940–960.
1174 Oleskevich, D. A., R. D. Hyndman, and K. Wang (1999). The updip and downdip limits
1175 to great subduction earthquakes: Thermal and structural models of Cascadia, south
1176 Alaska, SW Japan, and Chile, *J. Geophys. Res*. **104**, 14965–14991.
1177 Pacheco, J. F., L. R. Sykes, and C. H. Scholz (1993), Nature of seismic coupling along
1178 simple plate boundaries of the subduction type, *J. Geophys. Res.*, **98**(B8), 14133–
1179 14159, doi:10.1029/93JB00349.

1180 Pacor, F., D. Spallarossa, A. Oth, L. Luzi, R. Puglia, L. Cantore, A. Mercuri, M.
1181 D'Amico, M., and D. Bindi (2016). Spectral models for ground motion prediction in
1182 the L'Aquila region (central Italy): evidence for stress-drop dependence on magnitude
1183 and depth, *Geophys. J. Int*. **204**, 697–718.
1184 Page, M. T., S. Custódio, R. J. Archuleta, and J. M. Carlson (2009). Constraining
1185 earthquake source inversions with GPS data: 1. Resolution-based removal of artifacts,
1186 *J. Geophys. Res*. **114**, B01314, doi:10.1029/2007JB005449.
1187 Papazachos, B.C., E.M. Scordilis, D.G. Panagiotopoulos, C.B. Papazachos and G.F.
1188 Karakaisis (2004). Global relations between seismic fault parameters and moment
1189 magnitudes of earthquakes, *Bull. Geo. Soc. Greece* **36**, 1482–1489.
1190 Pegler, G., and S. Das (1996). Analysis of the relationship between seismic moment and
1191 fault length for large crustal strike-slip earthquakes between 1977–1992, *Geophys.*
1192 *Res. Lett*. **23**, 905–908.
1193 Ramírez-Gaytán, A., J. Aguirre, M. A. Jaimes, and V. Huérfano (2014). Scaling
1194 relationships of source parameters of Mw 6.9–8.1 earthquakes in the Cocos–Rivera–
1195 North American subduction zone. *Bull. Seismol. Soc. Am.* **104**, 840–854.
1196 Ripperger, J., and P. M. Mai (2004). Fast computation of static stress changes on 2D
1197 faults from final slip distributions, *Geophys. Res. Lett.* **31**, L18610, doi:
1198 10.1029/2004GL020594.
1199 Rivera, L., and H. Kanamori (2002), Spatial heterogeneity of tectonic stress and friction
1200 in the crust, *Geophys. Res Lett*. **29**(6), doi:10.1029/2001GL013803.
1201 Rodríguez-Pérez, Q., and L. Ottemöller (2013). Finite-fault scaling relations in Mexico,
1202 *Geophys. J. Int.* **193**,1570–1588.

1203 Romanowicz, B. (1992). Strike-slip earthquakes on quasi-vertical transcurrent faults:
1204 Inferences for general scaling relations, *Geophys. Res. Lett*. **19**, 481–484**.**

1205 Romanowicz, B., and L. J. Ruff (2002). On moment-length scaling of large strike slip
1206 earthquakes and the strength of faults, *Geophys. Res. Lett.* **29**(12),
1207 doi:10.1029/2001GL014479, 2002.

1208 Scholz, C. H. (1982). Scaling laws for large earthquakes: consequences for physical
1209 models, *Bull. Seismol. Soc. Am.* **72**, 1–14.

1210 Scholz, C. H. (1994). A reappraisal of large earthquake scaling, *Bull. Seismol. Soc. Am.*
1211 **84**, 215–218.

1212 Scholz, C. H., C. A. Aviles, and S. G. Wesnousky (1986). Scaling differences between
1213 large interplate and large intraplate earthquakes, *Bull. Seism. Soc. Am*. **76**, 65–70,
1214 1986.

1215 Scholz, C.H. (2002). *The mechanics of earthquakes and faulting*, Cambridge University
1216 Press.

1217 Schorlemmer, D., S. Wiemer, and M. Wyss (2005). Variations in earthquake-size
1218 distribution across different stress regimes. *Nature* **437**, 539–542.

1219 Seno, T. (2014). Stress drop as a criterion to differentiate subduction zones where Mw 9
1220 earthquakes can occur. *Tectonophysics*, **621**,198–210.

1221 Shapiro, S. S., and M. B. Wilk (1965) An analysis of variance test for normality
1222 (complete samples), *Biometrika* **52**, 591–611.

1223 Shaw, B. E. (2009). Constant stress drop from small to great earthquakes in magnitude-
1224 area scaling, *Bull. Seismol. Soc. Am.* **99**, 871–875

1225 Shaw, B. E., and S .G. Wesnousky (2008). Slip-length scaling in large earthquakes: the
1226 role of deep penetrating slip below the seismogenic layer, *Bull. Seismol. Soc. Am.* **98**,
1227 1633–1641.
1228 Shaw, B.E. and C.H. Scholz (2001). Slip-length scaling in large earthquakes:
1229 Observations and theory and implications for earthquake physics. *Geophys. Res. Lett.*
1230 **28**, doi: 10.1029/2000GL012762.
1231 Shi, B., J.N. Brune, Y. Zeng, and A. Anooshehpoor (2003). Dynamics of earthquake
1232 normal faulting: two-dimensional lattice particle model. *Bull. Seismol. Soc. Am*. **93**,
1233 1179–1197.
1234 Skarlatoudis, A.A., P.G. Somerville, and H.K. Thio (2016). Source-scaling relations of
1235 interface subduction earthquakes for strong ground motion and tsunami simulation.
1236 *Bull. Seismol. Soc. Am* **106,** doi: 10.1785/0120150320
1237 Somerville, P. G., K. Irikura, R. Graves, S. Sawada, D. Wald, N. Abrahamson, Y.
1238 Iwasaki, T. Kagawa, N. Smith, and A. Kowada (1999). Characterizing crustal
1239 earthquake slip models for the prediction of strong ground motion, *Seism. Res. Lett.*
1240 **70**, 59–80.
1241 Stafford, P. J. (2014). Source-scaling relationships for the simulation of rupture geometry
1242 within probabilistic seismic-hazard analysis. *Bull. Seismol. Soc. Am*. **104**, 1620–1635.
1243 Stirling, M., T. Goded, K. Berryman, and N. Litchfield (2013). Selection of earthquake
1244 scaling relationships for seismic-hazard analysis, *Bull. Seismol. Soc. Am*. 103, 2993–
1245 3011

1246 Stock, S., and E.G.C. Smith (2000). Evidence for different scaling of earthquake source
1247 parameters for large earthquakes depending on fault mechanism. *Geophys. J. Int.* **143**,
1248 157–162.
1249 Strasser, F. O., M. C. Arango, and J. J. Bommer (2010). Scaling of the source dimensions
1250 of interface and intraslab subduction-zone earthquakes with moment magnitude.
1251 *Seism. Res. Lett.* **81**, 941–950.
1252 Steketee, J. A. (1958). On Volterra's dislocation in a semi-infinite elastic medium, *Can. J.*
1253 *Phys*. **36**, 192–205.
1254 Strehlau, J. (1986). A discussion of the depth extent of rupture in large continental
1255 earthquakes. *Earthquake Source Mechanism* 131–145.
1256 Thingbaijam, K. K. S. and P. M. Mai (2016). Evidence for truncated exponential
1257 probability distribution of earthquake slip, *Bull. Seismol. Soc. Am.* **106**, 1802–1816.
1258 Wells, D. L., and K. J. Coppersmith (1994). New empirical relationships among
1259 magnitude, rupture length, rupture width, rupture area, and surface displacement,
1260 *Bull. Seismol. Soc. Am.* **84**, 974–1002.
1261 Wesnousky, S. G. (2008). Displacement and geometrical characteristics of earthquake
1262 surface ruptures: Issues and implications for seismic-hazard analysis and the process
1263 of earthquake rupture, *Bull. Seismol. Soc. Am.* **98** (4), 1609–1632.
1264 Wesnousky, S. G. (2006). Predicting the endpoints of earthquake ruptures. *Nature* **444**,
1265 358–360.
1266 Wesnousky, S. G. and G. P. Biasi (2011). The length to which an earthquake will go to
1267 rupture. *Bull. Seismol. Soc. Am.* **101**(4), 1948–1950.

1268 Williams, G. D. and I. Vann (1987). The geometry of listric normal faults and
1269 deformation in the hanging walls, *J. Struct. Geol.* **9**, 789–795
1270 Yagi, Y., N. Nishimura, and A. Kasahara (2012). Source process of the 12 May 2008
1271 Wenchuan, China, earthquake determined by waveform inversion of teleseismic body
1272 waves with a data covariance matrix. *Earth, Planets and Space* **64**, e13-e16.
1273 Ye, L., T. Lay, H. Kanamori, and L. Rivera (2016). Rupture characteristics of major and
1274 great (Mw ≥ 7.0) megathrust earthquakes from 1990 to 2015: 1. Source parameter
1275 scaling relationships, *J. Geophys. Res.* **121**, 826–844, doi:10.1002/2015JB012426
1276 Yen, Y.-T. and K.-F. Ma (2011). Source-Scaling Relationship for M 4.6–8.1
1277 Earthquakes, Specifically for Earthquakes in the Collision Zone of Taiwan, *Bull.*
1278 *Seismol. Soc. Am.* **101**, 464–481.
1279 Yen, Y.-T., K.-F. Ma, and Y.-Y. Wen (2008). Slip partition of the 26 December 2006
1280 Pingtung, Taiwan (M 6.9, M 6.8) earthquake doublet determined from teleseismic
1281 waveforms, *Terr. Atmos. Ocean. Sci.* **19**, 567–578.
1282 Yue, H., T. Lay, and K. D. Koper (2012). En echelon and orthogonal fault ruptures of the
1283 11 April 2012 great intraplate earthquakes, *Nature* **490**, 245–249.
1284 Zhang, P., X. Wen, Z.-K. Shen, and J. Chen (2010). Oblique, high-angle, listric-reverse
1285 faulting and associated development of strain: The Wenchuan earthquake of May 12,
1286 2008, Sichuan, China. *Ann. Rev. Earth Planet. Sci.* **38**, 353–382.
1287 Zhou, S., K. Irikura, and X. Chen (2004). Analysis of the reliability and resolution of the
1288 earthquake source history inferred from waveforms, taking the Chi-Chi earthquake as
1289 an example. *Geophys. Jour. Int.***157**.**3**, 1217–1232.

Zielke, O., M. Galis, and P. M. Mai (2017). Fault roughness and strength heterogeneity control earthquake size and stress drop, *Geophys. Res. Lett.* **44**, 777–783.

Appendix A

Scaling of Continental Strike-Slip Earthquakes

Figure A1 shows the regression between M_W and $\log_{10} L$ using the entire data set for continental strike-slip earthquakes, which appears to follow $M_0 \propto L^2$ scaling (according to the obtained fit with slope ~ 0.68). On the other hand, W grows very slowly with increasing M_W. Residuals do not show any systematic trends, and the statistical tests do not reject their normality.

In Figure A2, we present a bilinear relationship between M_W and $\log_{10} L$, considering the transition regime of L between 45 km and 55 km (in the range adopted by Leonard, 2010). Here, L scales with slope ~ 0.6 for $M_W \leq 7.1$, and with slope ~0.9 for $M_W > 7.1$. This bilinear relationship is similar to that formulated by Leonard (2010). However, regression between M_W and $\log_{10} W$ negates the constant rupture width for $M_W > 7.1$. Instead, it shows a gradual growth of W with increasing M_W. The residuals given by the bilinear regressions do not exhibit any systematic trends. The distributions of residuals in A1 and A2 do not allow discriminating statistically which of the two models is superior.

Nevertheless, we find no evidence that W saturates with increasing M_W, and therefore, we favor the linear relationships over the bilinear ones to describe the source-scaling properties of large strike-slip ($M_W \geq 5.5$) earthquakes. Blaser *et al*. (2010) made similar observations based a different dataset. Additionally, empirical evidence and

numerical simulations suggest that W may extend below the locking depth of the fault (Shaw and Scholz, 2001; Jiang and Lapusta, 2016).

FIGURE CAPTIONS

Figure 1. The distribution of slip-centroid depth, average rake angles, average fault-dip, and magnitudes in the present dataset. The plots include, if available, multiple models for the same event. Two models for the 2013 Okhotsk Sea earthquake, a shallow-dip normal-faulting event with slip-centroid depth > 600 km are not depicted. A few exceptional events are annotated. These include the 2009 Padang, Indonesia earthquake (reverse faulting event, occurred at considerable depth > 80 km), the 2008 Pingtung, Taiwan earthquake (strike-slip event at depth > 50 km), and the 2012 M_W ~8.7 Sumatra earthquake. The color version of this figure is available only in the electronic edition.

Figure 2. A schematic diagram depicting different dip-slip regimes in oceanic-continental subduction collision zone. These dip-slip regimes differ from each other in terms of associated active tectonic loading and material properties.

Figure 3. Generalized orthogonal regressions carried out with randomly generated 100 synthetic datasets of magnitude M_W, and $\log_{10} Y$, where Y is either width W (km), length L (km) or area A (km^2) such that the error variance ratios are fixed with applied standard deviations for M_W, W and L equal to (a) 0.100, 0.075 and 0.075, (b) 0.100, 0.030 and 0.030, (c) 0.100, 0.030 and 0.095, and (d) 0.100, 0.095 and 0.095. The leftmost column depicts cross-plots between magnitude M_W, and $\log_{10} Y$ from a single dataset. The

1337 histograms show the distributions of the mean slope estimated with η =0.5625 using the
1338 realizations of datasets. The dashed line on each histogram indicates the true slope
1339 parameter.

1340
1341 **Figure 4.** The regressions between moment magnitude M_W and rupture width W; solid
1342 and dashed lines correspond to the linear fits given by general orthogonal regressions and
1343 the 95% confidence intervals, respectively. If multiple rupture models for the same event
1344 exist, the data-point corresponds to the mean of the logarithm-transformed data, while the
1345 bars indicate the corresponding ranges. The scaling coefficients are listed in Table 1. The
1346 growth of W with increasing M_W is different for the different faulting regimes. We also
1347 observe that W for strike-slip events does not saturate but grows very slowly with M_W.
1348 Detailed plots for each faulting regime and the analysis of the residuals can be found in
1349 the Electronic Supplement Figs. S1 and S2.

1350
1351 **Figure 5.** Same as Fig. 4 but for the regressions between moment magnitude M_W and
1352 rupture length L. We find that L grows much faster for strike-slip events with increasing
1353 M_W compared to other faulting regimes. The scaling coefficients are listed in Table 1.
1354 Detailed plots for each faulting regime and the analysis of the residuals can be found in
1355 the Electronic Supplement Figs. S3 and S4.

1356

1357 **Figure 6.** Same as Fig. 4 but for the regressions between moment magnitude M_W and
1358 rupture area A. Except for normal-faulting events, the scaling behavior is statistically
1359 consistent with self-similar scaling. Subduction-interface events have the largest rupture
1360 area, for a given magnitude. At the lower magnitude range (M_W < 6.5), reverse-faulting

(shallow crustal) events have smallest rupture area for a given magnitude. The scaling coefficients are listed in Table 1. Detailed plots for each faulting regimes and the analysis of the residuals can be found in the Electronic Supplement Figs. S5 and S6.

Figure 7. Regressions between rupture area A and average displacement D (in solid black lines, with the 95% confidences intervals shown by dashed lines) are more or less statistically consistent with self-similar scaling of $A \propto D^{0.5}$ (shown by the lighter lines), except for normal-faulting events, which tends to deviate from this scaling behavior. The scaling coefficients are listed in Table 2. The color version of this figure is available only in the electronic edition.

Figure 8. Histograms and distributions of the residuals (difference between actual and predicted value on $\log_{10}$-scale) with respect to moment magnitude M_W: (a) for rupture length and (b) for rupture width, classified according to the different faulting regimes. The actual values correspond to the dataset of Blaser *et al*. (2010), and predicted values are obtained by applying our new empirical scaling relationships. Note the general agreement between the mean residual (solid line) from the zero-mean trend (dashed lighter line), except for the scaling of rupture-width for subduction-interface, strike-slip, and normal-faulting events.

Figure 9. The box-plots depict the distributions of the differences between the parameter – rupture width W and rupture length L - predicted by the empirical scaling laws ($\log_{10} W_{pred}$ and $\log_{10} L_{pred}$) and that given by a specific rupture model ($\log_{10} W$ and $\log_{10} L$). We group the rupture models according to the data used for the source-inversions: S (strong-motion data), T (teleseismic recordings), G (geodetic data) and J (joint) inversions. The numbers in the brackets indicates the number of models in each category, while N is total number of models.

Figure 10. The rupture width and rupture length of three exceptional oblique-slip events compared to the empirical scaling laws – for strike-slip events denoted by the lighter lines and for reverse-faulting (shallow crust) events by the darker lines. Note that the scaling law for reverse-faulting events has been extended beyond the upper data limit (Table 1). Interestingly, the 2008 Wenchuan earthquake follows the scaling of strike-slip events. The 1978 Tabas earthquake appears to be an outlier for the rupture width, but it might be that the estimate is poorly constrained. The 1989 Loma Prieta earthquake agrees with the scaling of reverse-faulting events, but its rupture width correspond to the lower bounds predicted by the scaling laws. The color version of this figure is available only in the electronic edition.

Figure 11. An example depicting the computation of source parameters for the fault-segments, using the rupture model given by Avouac *et al*. (2014) for the 2013 Balochistan earthquake. The color version of this figure is available only in the electronic edition.

Figure 12. The plots depict the regression analyses for different parameters for exterior fault-segments (left column) and interior fault-segments (right column). The parameters are fault-segment width W^S, length L^S, area A^S, and moment magnitude $M_W{}^S$. The solid lighter lines denote the respective empirical scaling laws for strike-slip events (as listed in Table 1). The darker solid and dashed lines are given by the regressions with the slope fixed to the empirical scaling laws, and self-similar constraints. The dot-dashed lines on the plots between $M_W{}^S$ and $\log_{10} L^S$ represent a *W*-model scaling with slope ~ 1.0. The relationships between W^S and $M_W{}^S$ are roughly consistent with that of overall rupture width, but those between L^S and $M_W{}^S$, and A^S and $M_W{}^S$ are different from the overall scaling laws, with shorter length and smaller area associated with fault-segments for the same moment magnitude.

Figure 13. The regression analyses show that relationship between rupture length *W* and rupture length *L* depends on the faulting regime, with variable slope (or power-law index). The gray bars indicate the range of parameter values for events with multiple source models; the logarithmic mean of these values is used in the analysis.

Figure 14. The fault-dip angle and ratio between $\log_{10} L$ and $\log_{10} W$ shows a positive correlation (correlation coefficient ~ 0.80) for large events ($M_W \geq 7.0$). For this event subset, the linear orthogonal fit (dashed line) also reveals a positive correlation. The symbols and notations are the same as in Figure 4.

1432 **Figure 15.** Distribution of average slip *D* over rupture width *W*, related to average strain
1433 and hence stress-drop (Mai and Beroza, 2000), with respect to moment magnitude M_W.
1434 Subduction-interface events exhibit smallest average stress-drop. Except for shallow
1435 crustal reverse-faulting events, this "stress-drop proxy" tends to increase with M_W.
1436
1437 **FIGURES IN APPENDIX**
1438 **Figure A1.** The top panel plots the regression analysis between M_W and $\log_{10} L$, and M_W
1439 and $\log_{10} W$ using the entire dataset of 30 continental strike-slip events with 65 rupture
1440 models, covering M_W 5.5 - 8.0, L = 6.5 km to 200 km, and W = 6.5 - 32.0 km. The bottom
1441 panel shows the distribution of residuals. The statistical tests for normality, as annotated
1442 on each plot, support that residuals are normally distributed.
1443
1444
1445 **Figure A2.** Similar to Figure A1, but now the regression analysis adopts a bilinear model
1446 with crossover at L=55 km between M_W and $\log_{10} L$, and L= 45 km between M_W and $\log_{10}$
1447 W. In case of M_W vs. $\log_{10} L$, the slope changes from ~0.6 for $M_W \leq 7.1$ to ~0.9 for $M_W >$
1448 7.1. On the other hand, the scaling relationships between M_W and $\log_{10} W$ have slopes
1449 that do not differ statistically, and also from the fit on the entire data range (Fig. A1). The
1450 bilinear model (specifically for scaling of L) associate marginally lower average residual
1451 but more parameters. Therefore, we cannot conclude it to be better than the linear model.
1452
1453
1454

TABLES

Table 1. Scaling coefficients between rupture length, rupture width, rupture area, and moment magnitude.

Table 2. Scaling coefficients between average slip, rupture width, rupture length, rupture area, and moment magnitude.

Table

Table 1. Scaling coefficients between rupture length, rupture width, rupture area, and moment magnitude.

Faulting regime	Equation	*b (sb)*	*a (sa)*	σ	r^2	Data range	
						M_W	Dimension
Reverse-faulting (shallow crustal)	$\log_{10} L = a + b M_W$	0.614 (0.043)	-2.693 (0.292)	0.083	0.93	5.59 – 7.69	4.9 – 108.0 km
	$\log_{10} W = a + b M_W$	0.435 (0.050)	-1.669 (0.336)	0.087	0.90	5.59 – 7.69	4.8 – 45.0 km
	$\log_{10} A = a + b M_W$	1.049 (0.066)	-4.362 (0.445)	0.121	0.94	5.59 – 7.69	23.5 – 4860.0 km^2
Subduction-interface	$\log_{10} L = a + b M_W$	0.583 (0.037)	-2.412 (0.288)	0.107	0.85	6.68 – 9.19	29.2 –1420.0 km
	$\log_{10} W = a + b M_W$	0.366 (0.031)	-0.880 (0.243)	0.099	0.75	6.68 – 9.19	29.2 – 260.0 km
	$\log_{10} A = a + b M_W$	0.949 (0.049)	-3.292 (0.377)	0.150	0.86	6.68 – 9.19	852.6 – 318080.0 km^2
Normal-faulting	$\log_{10} L = a + b M_W$	0.485 (0.036)	-1.722 (0.260)	0.128	0.88	5.86 – 8.39	9.0 – 262.5 km
	$\log_{10} W = a + b M_W$	0.323 (0.047)	-0.829 (0.333)	0.128	0.77	5.86 – 8.39	6.0 – 112.5 km
	$\log_{10} A = a + b M_W$	0.808 (0.059)	-2.551 (0.423)	0.181	0.88	5.86 – 8.39	54.0 – 29531.3 km^2
Strike-slip	$\log_{10} L = a + b M_W$	0.681 (0.052)	-2.943 (0.357)	0.151	0.88	5.38 – 8.70	6.0 – 580.0 km
	$\log_{10} W = a + b M_W$	0.261 (0.026)	-0.543 (0.179)	0.105	0.75	5.38 – 8.70	6.5 – 50.0 km
	$\log_{10} A = a + b M_W$	0.942 (0.058)	-3.486 (0.399)	0.184	0.88	5.38 – 8.70	39.0 – 29000.0 km^2

- Scaling coefficients were obtained by general orthogonal regressions, except for the scaling relationships between moment magnitude and rupture area, which were calculated using those of rupture length and rupture width. The notations in the equations: L, W, A and M_W denote rupture length, rupture width rupture area, and moment magnitude. The slope and intercept are given by a and b, their standard errors by sa and sb, while standard deviation is given by σ. The correlation coefficient is denoted by r^2.

Table 2. Scaling coefficients between average slip, rupture width, rupture length, rupture area, and moment magnitude.

Faulting regime	Equation	*b (sb)*	*a (sa)*	σ	r^2
Reverse-faulting (shallow crustal)	$\log_{10} D = a + b M_W$	0.451 (0.093)	-3.156 (0.639)	0.149	0.77
	$\log_{10} D = a + b \log_{10} A$	0.429 (0.134)	-1.213 (0.379)	0.180	0.72
	$\log_{10} D = a + b \log_{10} L$	0.975 (0.203)	-1.456 (0.309)	0.132	0.78
	$\log_{10} D = a + b \log_{10} W$	0.767 (0.397)	-1.022 (0.522)	0.200	0.58
Subduction-interface	$\log_{10} D = a + b M_W$	0.552 (0.067)	-4.226 (0.526)	0.171	0.74
	$\log_{10} D = a + b \log_{10} A$	0.582 (0.136)	-2.375 (0.558)	0.257	0.35
	$\log_{10} D = a + b \log_{10} L$	1.092 (0.223)	-2.320 (0.477)	0.213	0.34
	$\log_{10} D = a + b \log_{10} W$	1.244 (0.577)	-2.438 (1.154)	0.213	0.25
Normal-faulting	$\log_{10} D = a + b M_W$	0.693 (0.066)	-4.967 (0.484)	0.195	0.86
	$\log_{10} D = a + b \log_{10} A$	0.858 (0.214)	-2.779 (0.683)	0.330	0.29
	$\log_{10} D = a + b \log_{10} L$	1.302 (0.303)	-2.302 (0.531)	0.252	0.43
	$\log_{10} D = a + b \log_{10} W$	2.512 (0.842)	-3.698 (1.216)	0.223	0.00
Strike-slip	$\log_{10} D = a + b M_W$	0.558 (0.054)	-4.032 (0.376)	0.227	0.77
	$\log_{10} D = a + b \log_{10} A$	0.593 (0.112)	-1.875 (0.342)	0.302	0.43
	$\log_{10} D = a + b \log_{10} L$	0.789 (0.144)	-1.473 (0.259)	0.276	0.48
	$\log_{10} D = a + b \log_{10} W$	2.391 (0.485)	-3.092 (0.602)	0.178	0.10

- Scaling coefficients were obtained by general orthogonal regressions. The notations are as in Table 1: D, W, L, A and M_W denote average slip (in m), rupture area (in km^2) and moment magnitude.

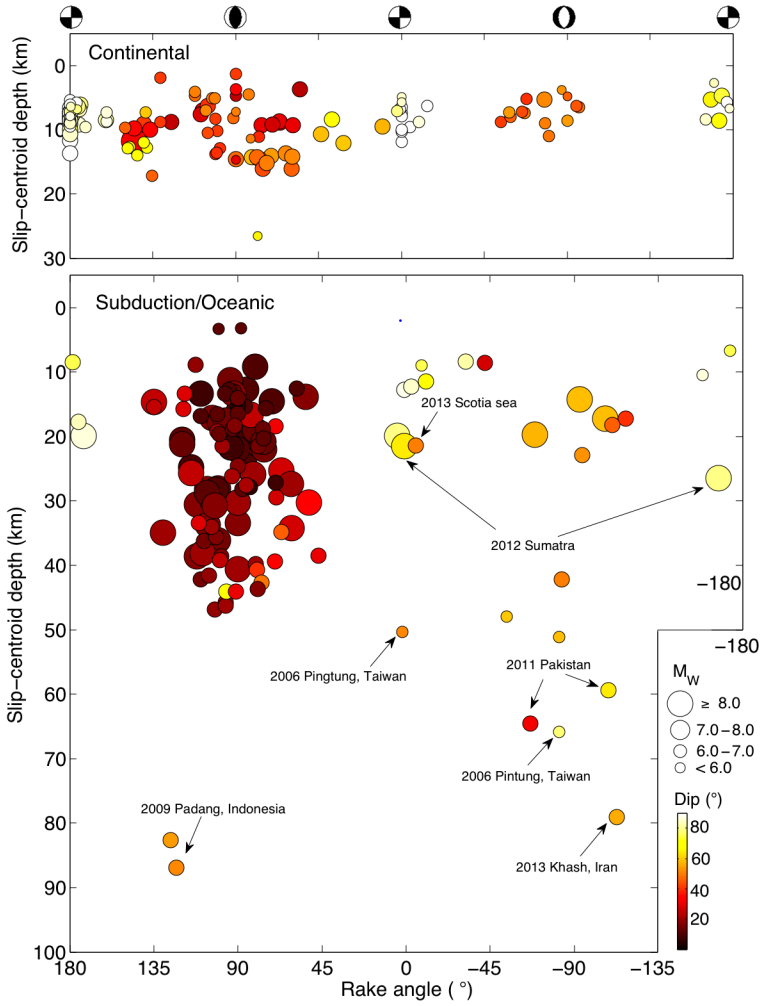

Figure 1. The distribution of slip-centroid depth, average rake angles, average fault-dip, and magnitudes in the present dataset. The plots include, if available, multiple models for the same event. Two models for the 2013 Okhotsk Sea earthquake, a shallow-dip normal-faulting event with slip-centroid depth > 600 km are not depicted. A few exceptional events are annotated. These include the 2009 Padang, Indonesia earthquake (reverse faulting event, occurred at considerable depth > 80 km), the 2008 Pingtung, Taiwan earthquake (strike-slip event at depth > 50 km), and the 2012 M_W ~8.7 Sumatra earthquake. The color version of this figure is available only in the electronic edition.

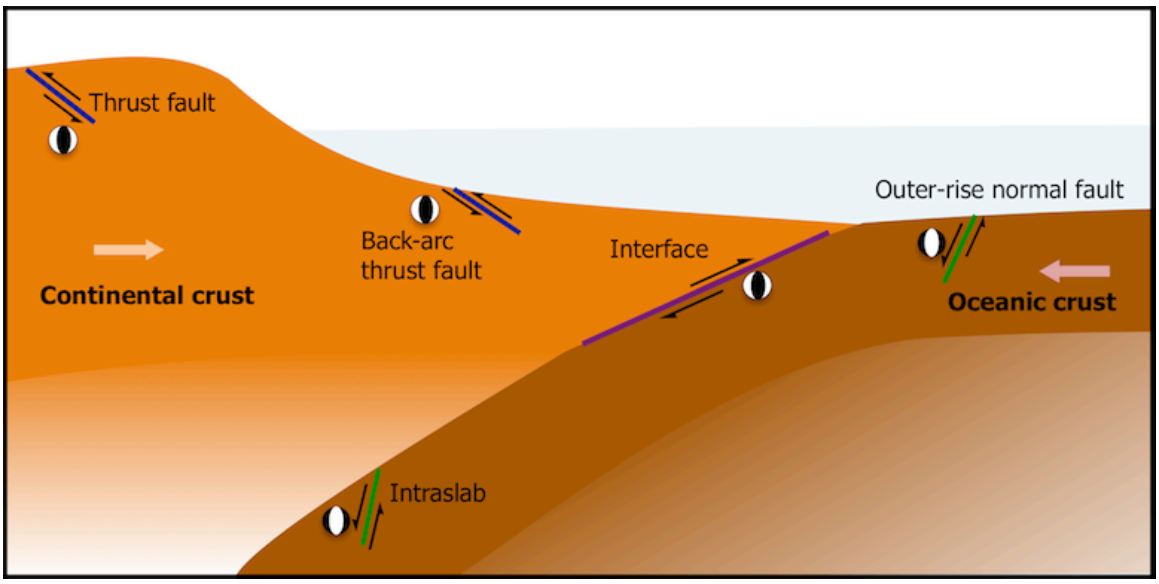

Figure 2. A schematic diagram depicting different dip-slip regimes in oceanic-continental subduction collision zone. These dip-slip regimes differ from each other in terms of associated active tectonic loading and material properties.

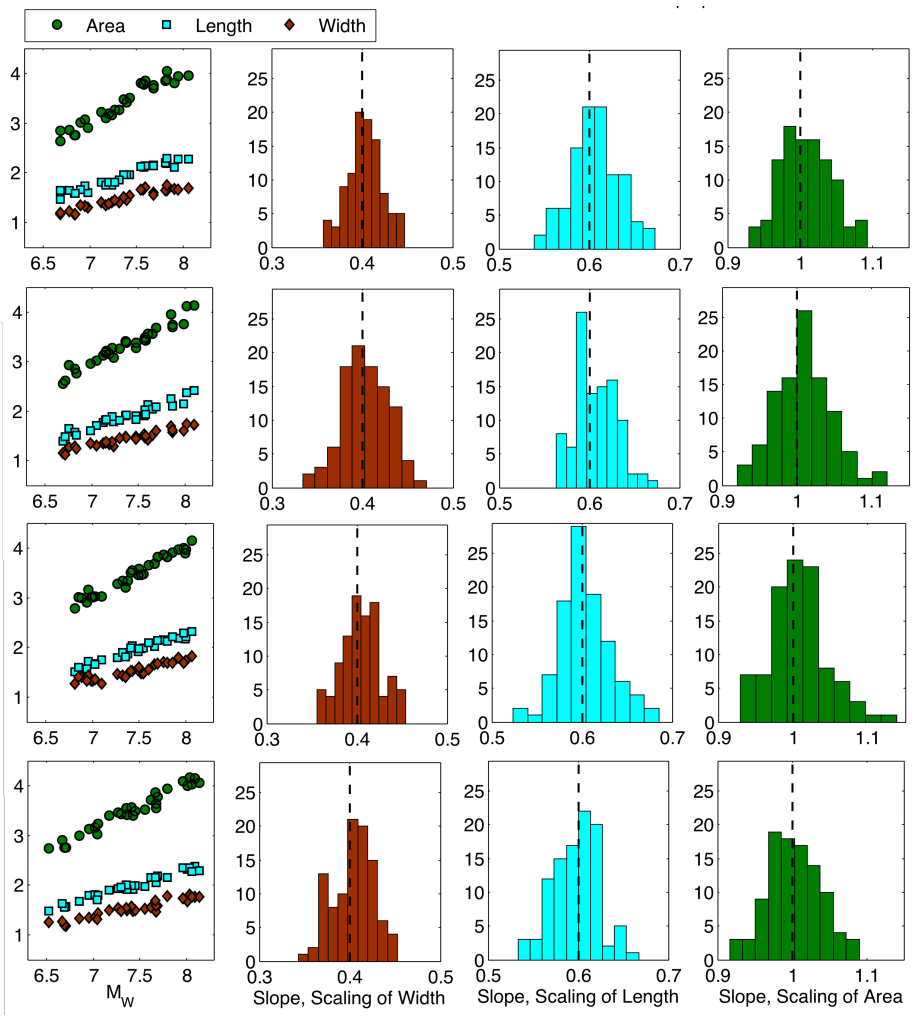

Figure 3. Generalized orthogonal regressions carried out with randomly generated 100 synthetic datasets of magnitude M_W, and $\log_{10} Y$, where Y is either width W (km), length L (km) or area A (km^2) such that the error variance ratios are fixed with applied standard deviations for M_W, W and L equal to (a) 0.100, 0.075 and 0.075, (b) 0.100, 0.030 and 0.030, (c) 0.100, 0.030 and 0.095, and (d) 0.100, 0.095 and 0.095. The leftmost column depicts cross-plots between magnitude M_W, and $\log_{10} Y$ from a single dataset. The histograms show the distributions of the mean slope estimated with η =0.5625 using the realizations of datasets. The dashed line on each histogram indicates the true slope parameter.

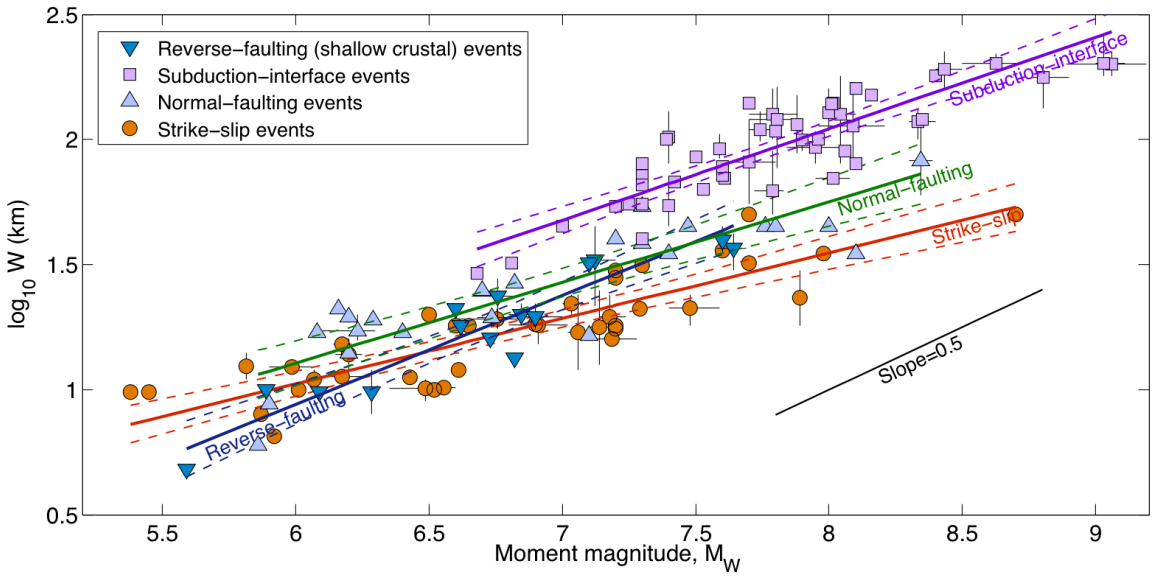

Figure 4. The regressions between moment magnitude M_W and rupture width W; solid and dashed lines correspond to the linear fits given by general orthogonal regressions and the 95% confidence intervals, respectively. If multiple rupture models for the same event exist, the data-point corresponds to the mean of the logarithm-transformed data, while the bars indicate the corresponding ranges. The scaling coefficients are listed in Table 1. The growth of W with increasing M_W is different for the different faulting regimes. We also observe that W for strike-slip events does not saturate but grows very slowly with M_W. Detailed plots for each faulting regime and the analysis of the residuals can be found in the Electronic Supplement Figs. S1 and S2.

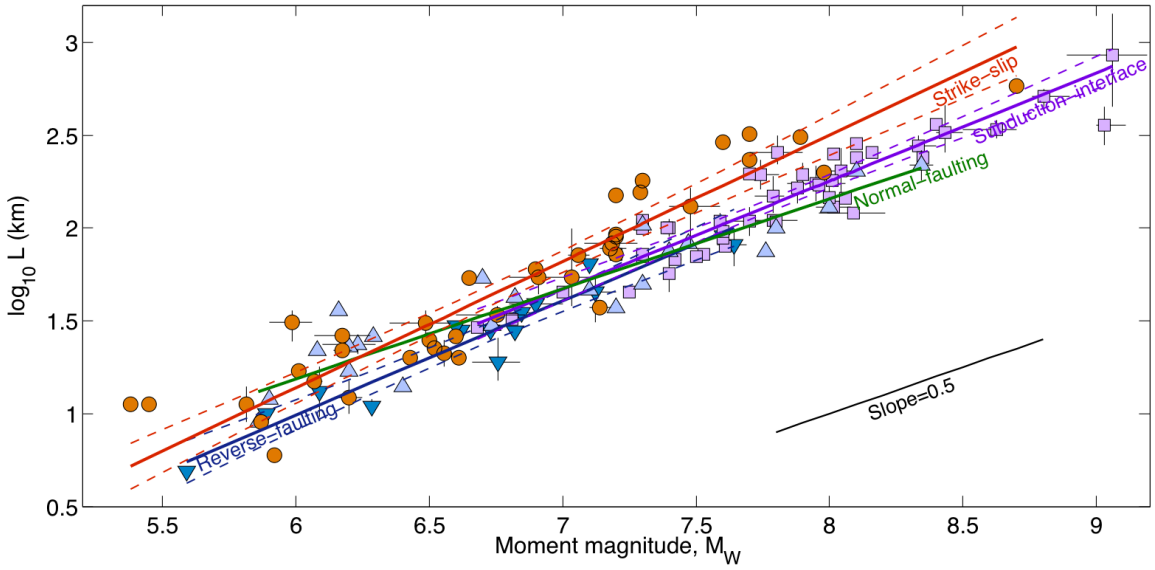

Figure 5. Same as Fig. 4 but for the regressions between moment magnitude M_W and rupture length L. We find that L grows much faster for strike-slip events with increasing M_W compared to other faulting regimes. The scaling coefficients are listed in Table 1. Detailed plots for each faulting regime and the analysis of the residuals can be found in the Electronic Supplement Figs. S3 and S4.

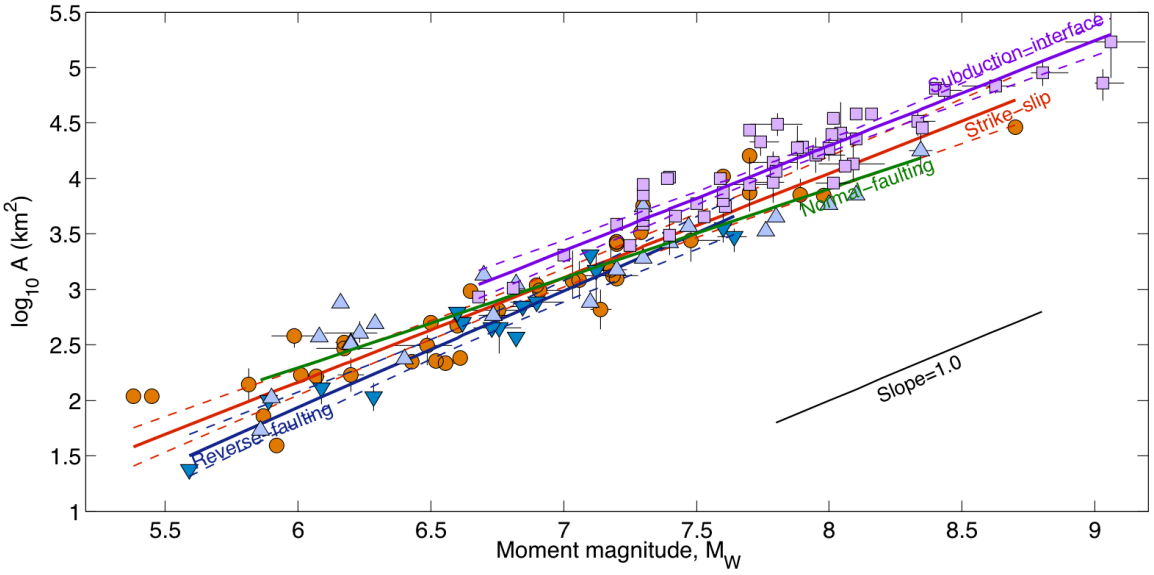

Figure 6. Same as Fig. 4 but for the regressions between moment magnitude M_W and rupture area A. Except for normal-faulting events, the scaling behavior is statistically consistent with self-similar scaling. Subduction-interface events have the largest rupture area, for a given magnitude. At the lower magnitude range ($M_W < 6.5$), reverse-faulting (shallow crustal) events have smallest rupture area for a given magnitude. The scaling coefficients are listed in Table 1. Detailed plots for each faulting regimes and the analysis of the residuals can be found in the Electronic Supplement Figs. S5 and S6.

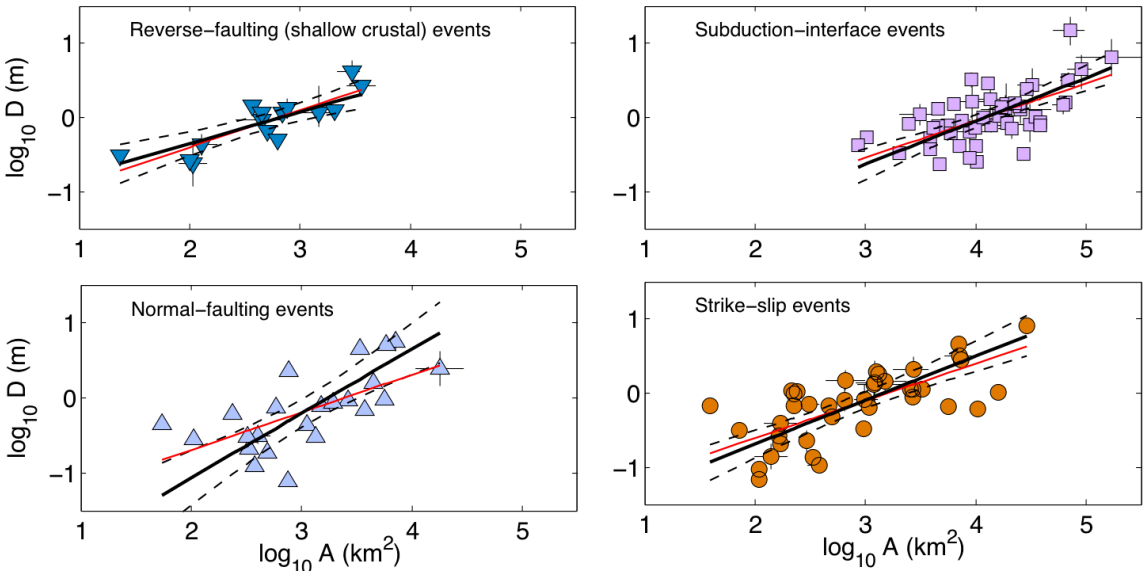

Figure 7. Regressions between rupture area A and average displacement D (in solid black lines, with the 95% confidences intervals shown by dashed lines) are more or less statistically consistent with self-similar scaling of $A \propto D^{0.5}$ (shown by the lighter lines), except for normal-faulting events, which tends to deviate from this scaling behavior. The scaling coefficients are listed in Table 2. The color version of this figure is available only in the electronic edition.

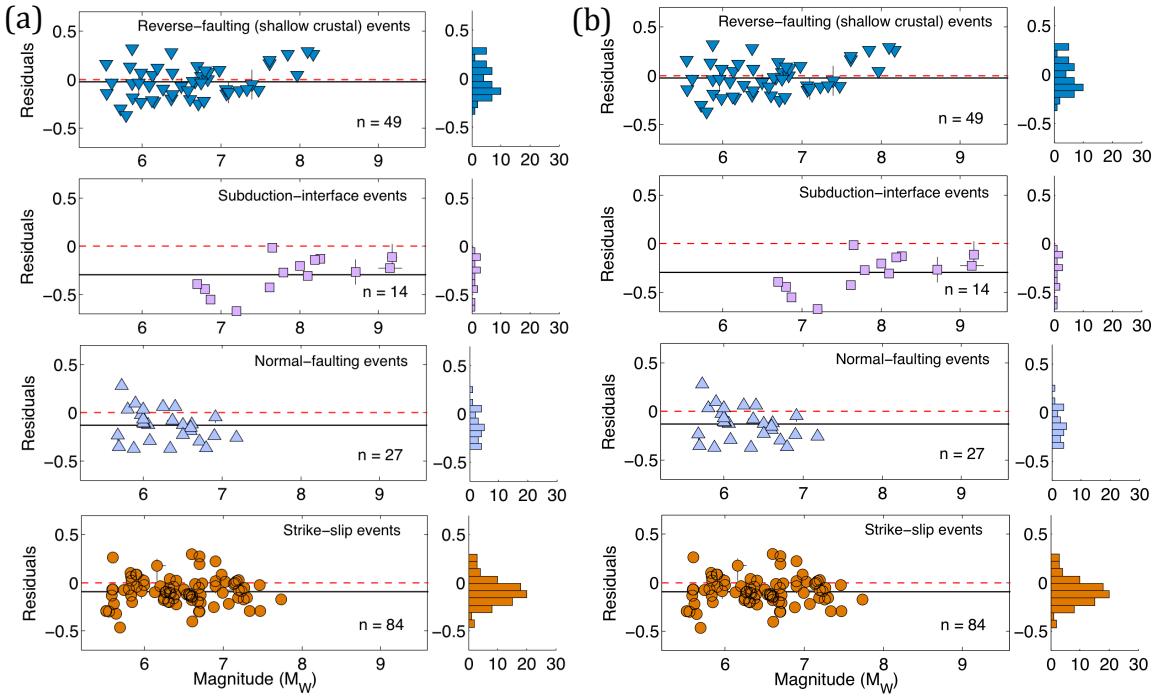

Figure 8. Histograms and distributions of the residuals (difference between actual and predicted value on $\log_{10}$-scale) with respect to moment magnitude M_W: (a) for rupture length and (b) for rupture width, classified according to the different faulting regimes. The actual values correspond to the dataset of Blaser *et al*. (2010), and predicted values are obtained by applying our new empirical scaling relationships. Note the general agreement between the mean residual (solid line) from the zero-mean trend (dashed lighter line), except for the scaling of rupture-width for subduction-interface, strike-slip, and normal-faulting events.

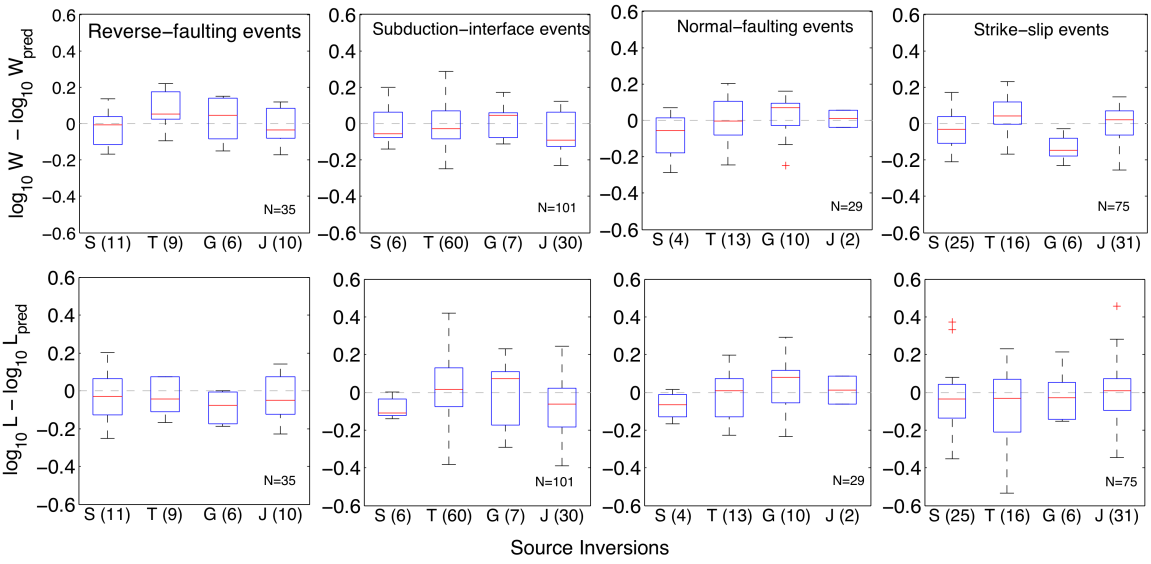

Figure 9. The box-plots depict the distributions of the differences between the parameter – rupture width W and rupture length L - predicted by the empirical scaling laws ($\log_{10} W_{\text{pred}}$ and $\log_{10} L_{\text{pred}}$) and that given by a specific rupture model ($\log_{10} W$ and $\log_{10} L$). We group the rupture models according to the data used for the source-inversions: S (strong-motion data), T (teleseismic recordings), G (geodetic data) and J (joint) inversions. The numbers in the brackets indicates the number of models in each category, while N is total number of models.

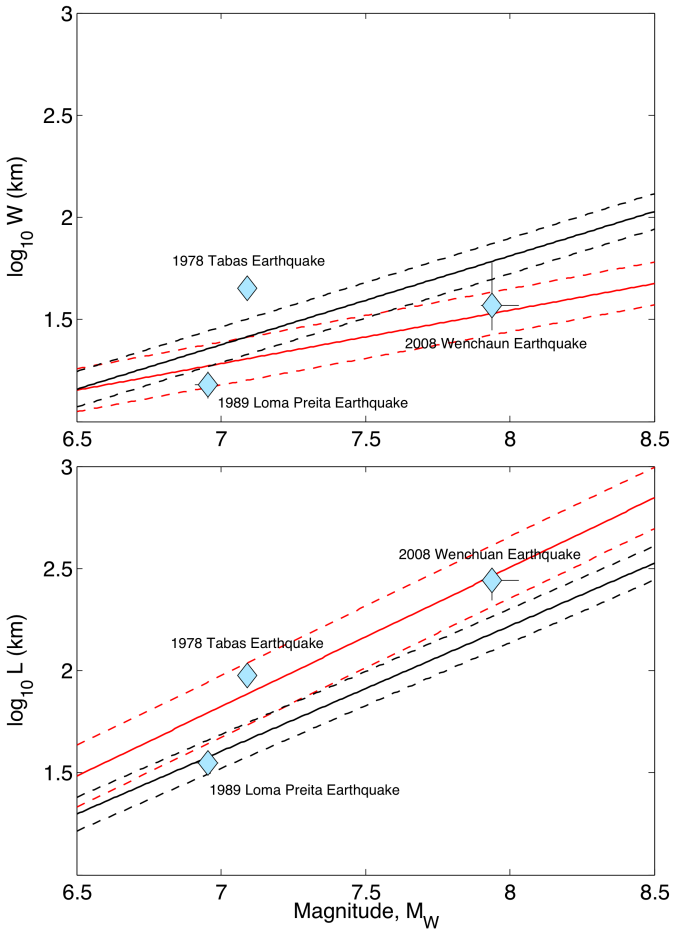

Figure 10. The rupture width and rupture length of three exceptional oblique-slip events compared to the empirical scaling laws – for strike-slip events denoted by the lighter lines and for reverse-faulting (shallow crust) events by the darker lines. Note that the scaling law for reverse-faulting events has been extended beyond the upper data limit (Table 1). Interestingly, the 2008 Wenchuan earthquake follows the scaling of strike-slip events. The 1978 Tabas earthquake appears to be an outlier for the rupture width, but it might be that the estimate is poorly constrained. The 1989 Loma Prieta earthquake agrees with the scaling of reverse-faulting events, but its rupture width correspond to the lower bounds predicted by the scaling laws. The color version of this figure is available only in the electronic edition.

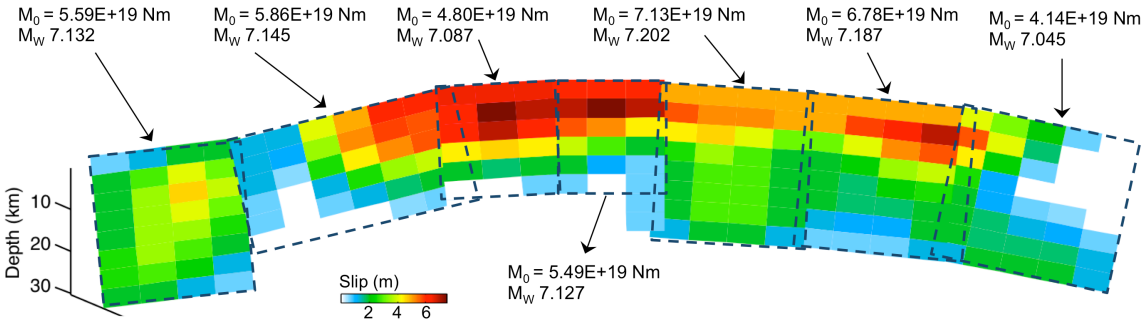

Figure 11. An example depicting the computation of source parameters for the fault-segments, using the rupture model given by Avouac *et al*. (2014) for the 2013 Balochistan earthquake. The color version of this figure is available only in the electronic edition.

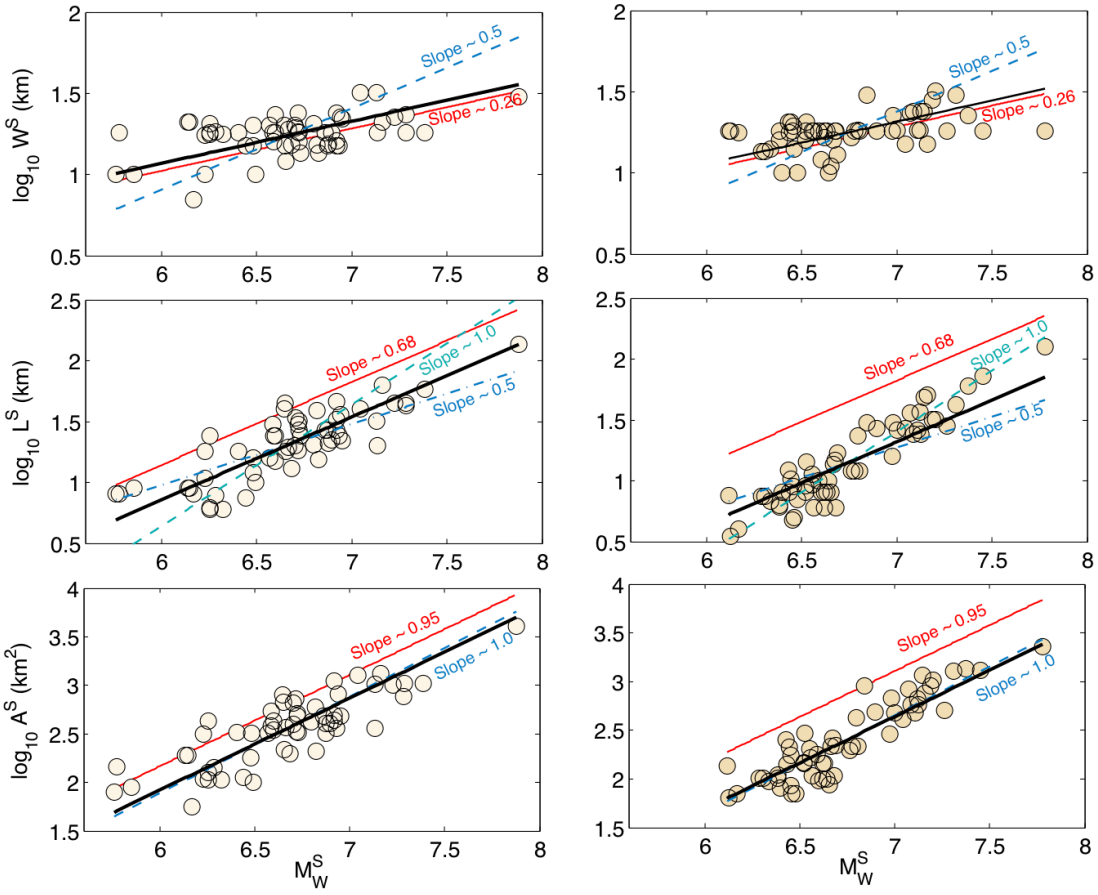

Figure 12. The plots depict the regression analyses for different parameters for exterior fault-segments (left column) and interior fault-segments (right column). The parameters are fault-segment width W^S, length L^S, area A^S, and moment magnitude $M_W{}^S$. The solid lighter lines denote the respective empirical scaling laws for strike-slip events (as listed in Table 1). The darker solid and dashed lines are given by the regressions with the slope fixed to the empirical scaling laws, and self-similar constraints. The dot-dashed lines on the plots between $M_W{}^S$ and $\log_{10} L^S$ represent a W-model scaling with slope ~ 1.0. The relationships between W^S and $M_W{}^S$ are roughly consistent with that of overall rupture width, but those between L^S and $M_W{}^S$, and A^S and $M_W{}^S$ are different from the overall scaling laws, with shorter length and smaller area associated with fault-segments for the same moment magnitude.

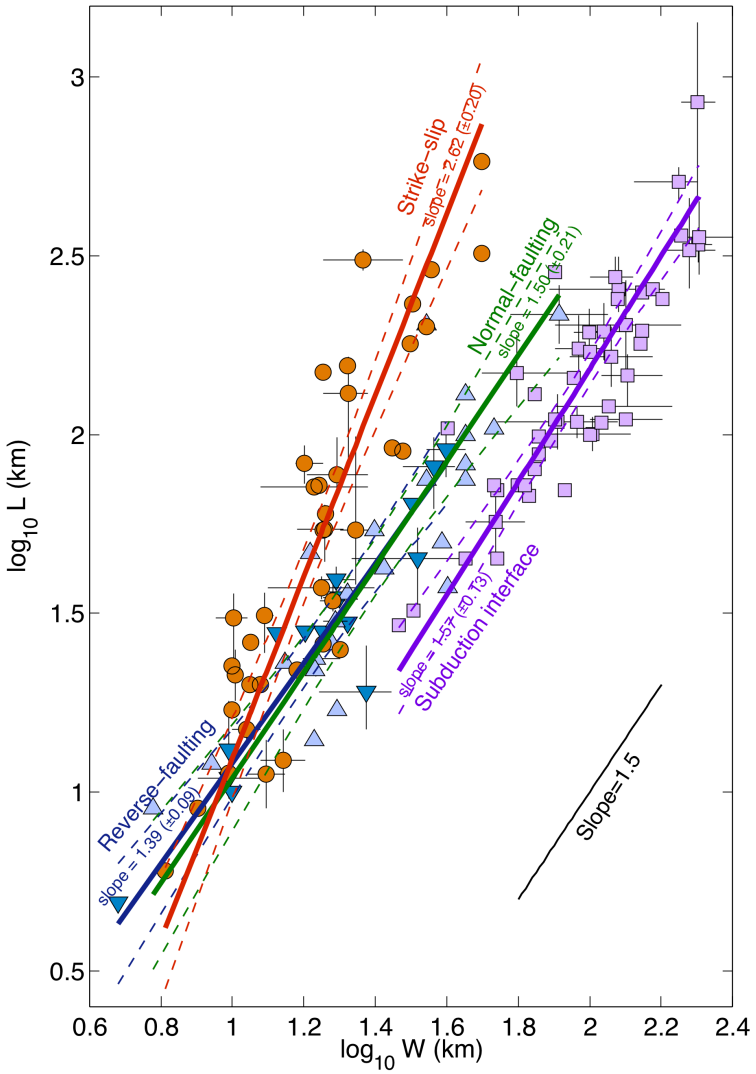

Figure 13. The regression analyses show that relationship between rupture length *W* and rupture length *L* depends on the faulting regime, with variable slope (or power-law index). The gray bars indicate the range of parameter values for events with multiple source models; the logarithmic mean of these values is used in the analysis.

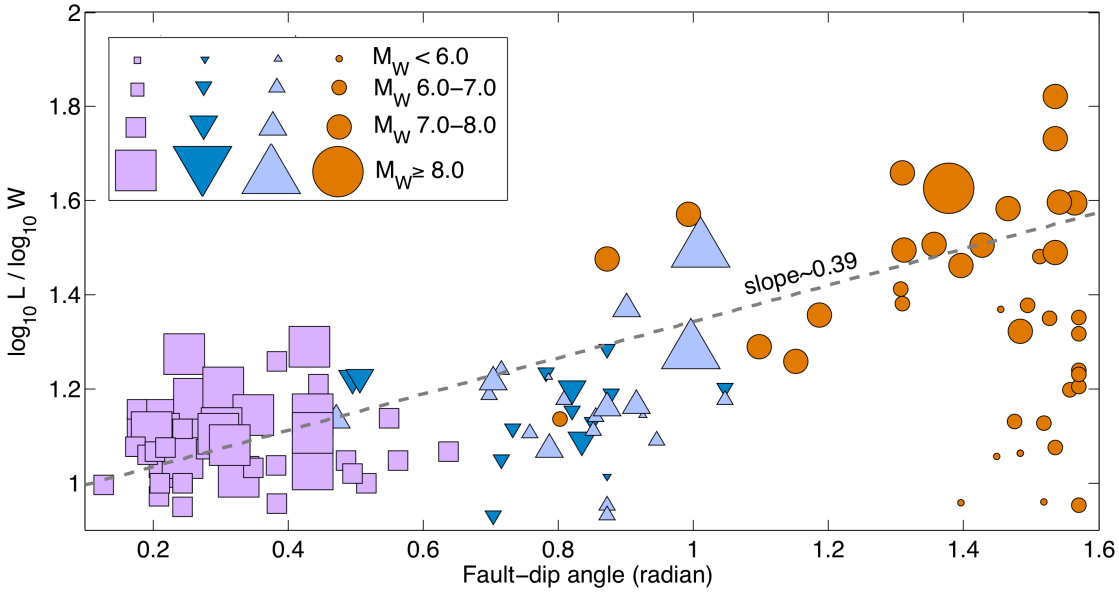

Figure 14. The fault-dip angle and ratio between $\log_{10} L$ and $\log_{10} W$ shows a positive correlation (correlation coefficient ~ 0.80) for large events ($M_W \geq 7.0$). For this event subset, the linear orthogonal fit (dashed line) also reveals a positive correlation. The symbols and notations are the same as in Figure 4.

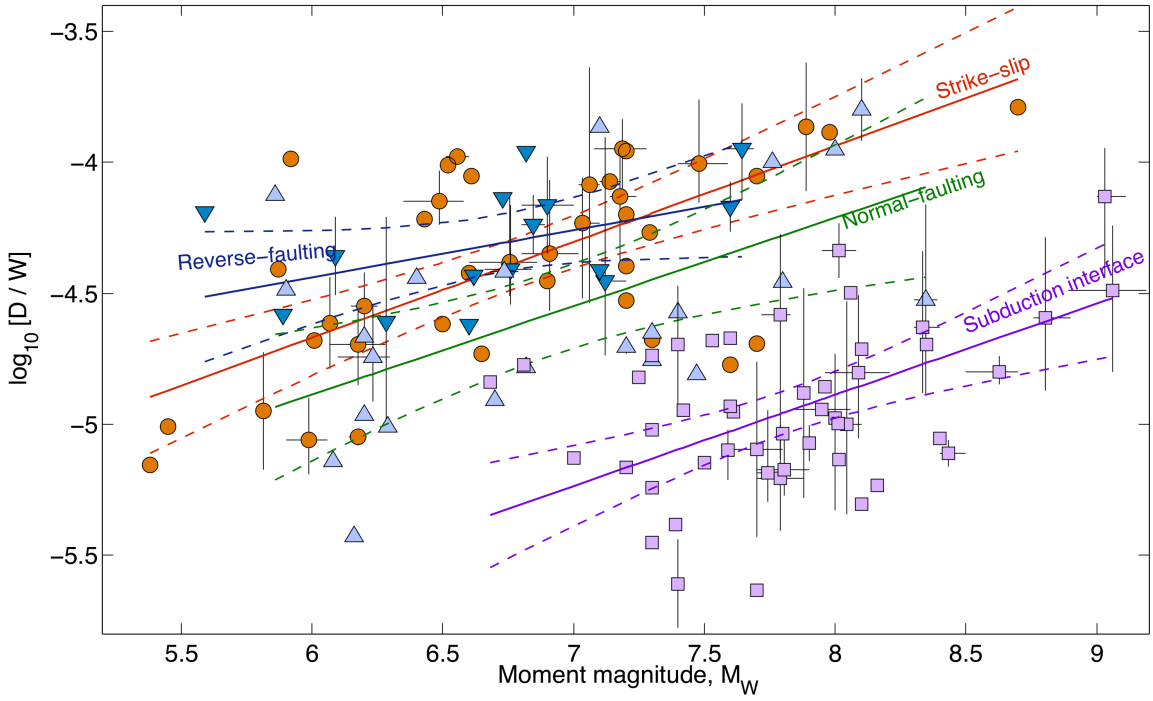

Figure 15. Distribution of average slip D over rupture width W, related to average strain and hence stress-drop (Mai and Beroza, 2000), with respect to moment magnitude M_W. Subduction-interface events exhibit smallest average stress-drop. Except for shallow crustal reverse-faulting events, this "stress-drop proxy" tends to increase with M_W.

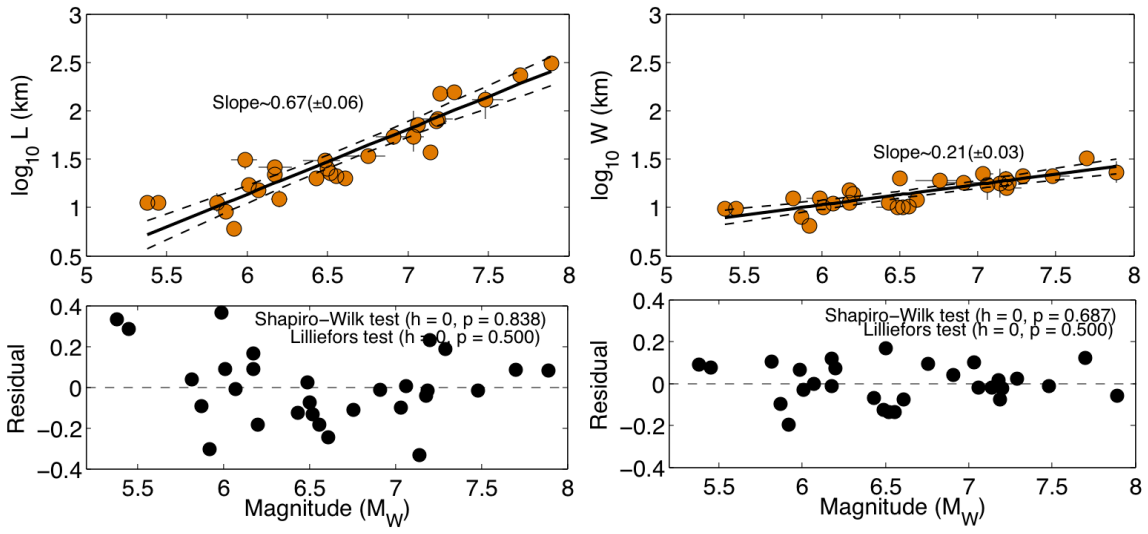

Figure A1. The top panel plots the regression analysis between M_W and $\log_{10} L$, and M_W and $\log_{10} W$ using the entire dataset of 30 continental strike-slip events with 65 rupture models, covering M_W 5.5 - 8.0, L = 6.5 km to 200 km, and W = 6.5 - 32.0 km. The bottom panel shows the distribution of residuals. The statistical tests for normality, as annotated on each plot, support that residuals are normally distributed.

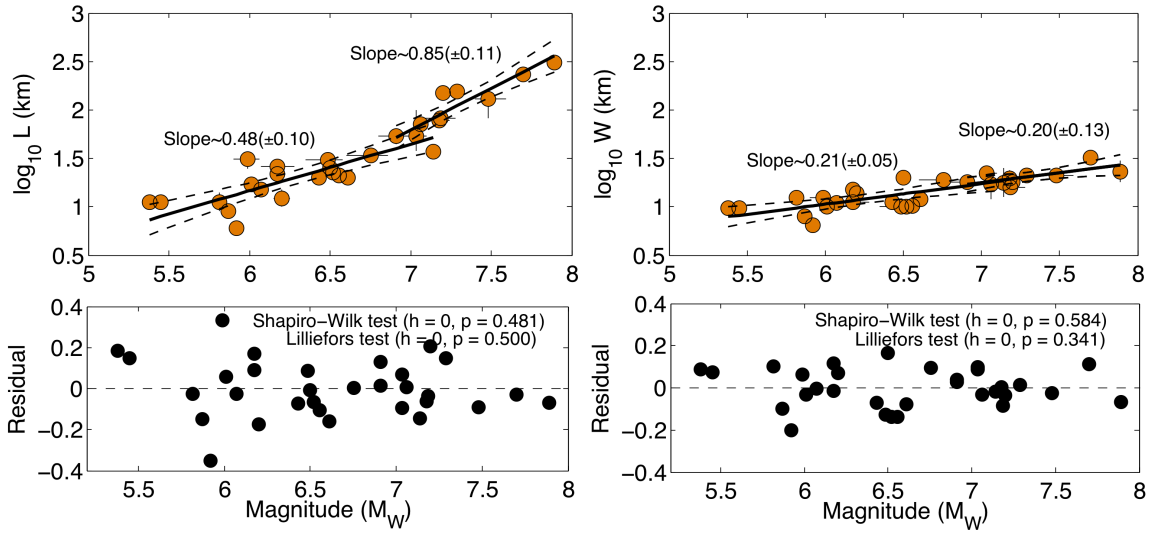

Figure A2. Similar to Figure A1, but now the regression analysis adopts a bilinear model with crossover at L=55 km between M_W and $\log_{10} L$, and L= 45 km between M_W and $\log_{10} W$. In case of M_W vs. $\log_{10} L$, the slope changes from ~0.6 for $M_W \leq 7.1$ to ~0.9 for $M_W > 7.1$. On the other hand, the scaling relationships between M_W and $\log_{10} W$ have slopes that do not differ statistically, and also from the fit on the entire data range (Fig. A1). The bilinear model (specifically for scaling of L) associate marginally lower average residual but more parameters. Therefore, we cannot conclude it to be better than the linear model.

Electronic Supplement

New Empirical Earthquake-Source Scaling Laws

by Kiran Kumar S. Thingbaijam, P. Martin Mai and Katsuichiro Goda

Figures depicting regression analysis, normality probability plots and comparisons between different source-scaling relationships, and tables listing rupture models and different earthquake source-scaling relationships.

LIST OF TABLES

Table S1. The rupture models and estimated rupture dimensions

Table S2. Comparison of source-scaling relationships for shallow crustal reverse-faulting events obtained by various studies

Table S3. Same as Table S2, but for subduction-interface events obtained by various studies

Table S4. Same as Table S2, but for normal-faulting events obtained by various studies

Table S5. Same as Table S2, but for strike-slip events obtained by various studies

LIST OF FIGURES

Figure S1. The black solid lines denote the general orthogonal regressions between M_W and $\log_{10} W$, where M_W is moment magnitude and W is rupture width. The dashed black lines show the 95% confidence intervals of the linear fits. The dashed red lines are linear fits with the slope fixed to be equal to 0.5 (as given by self-similar constraint). Except for reverse-slip events, the regressions show deviation from the self-similar scaling.

Figure S2. Normality probability plots of residuals for the regressions between M_W and $\log_{10} W$ (Fig. S1). The data-points follow linear trends in each case, suggesting that the distribution is close to a normal one. The results of additional statistical tests, as annotated, also indicate that the residuals are essentially normally distributed.

Figure S3. Similar to Figure S1, but for regressions between M_W and $\log_{10} L$, where L is rupture length. Except for normal-slip events, the regressions shows a general tendency to deviate from the self-similar scaling, which is more evident with the strike-slip events with estimated slope ~ 0.7.

Figure S4. Similar to Figure S2, but for the regressions between M_W and $\log_{10} L$ (Fig. S3), showing that the data-points follow linear trends in each case, hence the distributions are close to follow normality. The results of additional statistical tests, as annotated, also indicate that residuals are normally distributed.

Figure S5. Similar to Figure S1, but showing the scaling between M_W and $\log_{10} A$, where A is rupture area. Furthermore, the depicted scaling relationships (in black lines) are derived from scaling relationships of W and L, instead of applying a direct regression. Except for normal-slip events, the empirical scaling relationships are consistent with self-similar scaling.

Figure S6. Same as Figure S2, but for the scaling relationships between M_W and $\log_{10} A$ (Fig. S5).

Figure S7. Regression between rupture width W and average slip D on logarithm-logarithm scale. The legends are same as that for Figure S1. The red lines represent this linear fit with fixed slope ~1.0.

Figure S8. Regressions between rupture width L and average slip D on logarithm-logarithm scale. The legends are same as that for Figure S1. The red lines represent this linear fit with fixed slope ~1.0.

Figure S9. Same as Fig. S8, but for the regressions between moment magnitude M_W and average displacement D. The observed relationships are more or less statistically consistent with $D \propto M_W^{0.5}$ (given by the lighter solid lines), except for normal-faulting events, which deviate from this scaling behavior.

Figure S10. Source-scaling relationships provided by different studies for reverse-faulting shallow crustal earthquakes (listed in Table S2). The standard errors associated with these relationships have not been depicted.

Figure S11. Same as Fig. S10, but for subduction-interface events.

Figure S12. Same as Fig. S10, but for normal-faulting events.

Figure S13. Same as Fig. S10, but for strike-slip events.

Figure S14. The fault dip angles shows a positive correlation (correlation coefficient ~ 0.72) with fault aspect ratios (L/W, where L and W are rupture length and width) for large events ($M_W \geq 7.0$). For this event subset, the linear orthogonal fit (dashed line) also suggests a positive correlation. The symbols and notations are the same as in Figure S1.

LIST OF REFERENCES

Altiner, Y., W. Söhne, C. Güney, J. Perlt, R. Wang, and M. Muzli (2013). A geodetic study of the 23 October 2011 Van, Turkey earthquake, *Tectonophysics* **588**, 118–134.

Ammon, C. J., J. Chen, H.-K. Thio, D. Robinson, S. Ni, V. Hjorleifsdottir, H. Kanamori, T. Lay, S. Das, D. Helmberger, G. Ichinose, J. Polet, and D. Wald (2005). Rupture process of the great 2004 Sumatra-Andaman earthquake, *Science* **308**, 1133–1139.

Ammon, C. J., T. Lay, H. Kanamori, and M. Cleveland (2011). A rupture model of the 2011 off the Pacific coast of Tohoku Earthquake, *Earth Planets Space* **63**, 693–696.

Antolik, M., A. Kaverina, and D. S. Dreger (2000). Compound rupture of the great 1998 Antarctic plate earthquake, *J. Geophys. Res*., **105**, 23825–23838.

Archuleta, R. J. (1984). A faulting model for the 1979 Imperial Valley earthquake. *J. Geophys. Res*. **89**, 4559–4585.

Asano, K. and T. Iwata (2006). Source process and near-source ground motions of the 2005 West Off Fukuoka Prefecture earthquake, *Earth Planets Space* **58**, 93–98.

Asano, K. and T. Iwata (2009). Source rupture process of the 2004 Chuetsu, Mid-Niigata prefecture, Japan, earthquake inferred from waveform inversion with dense strong-motion data. *Bull. Seismol. Soc. Am*. **99**, 123–140.

Asano, K. and T. Iwata (2011a). Source rupture process of the 2007 Noto Hanto, Japan, earthquake estimated by the joint inversion of strong motion and GPS data. *Bull. Seismol. Soc. Am.* **101**, 2467–2480.

Asano, K. and T. Iwata (2011b). Characterization of stress drops on asperities estimated from the heterogeneous kinematic slip model for strong motion prediction for inland crustal earthquakes in Japan. *Pageoph* 168, 105–116.

Asano, K., T. Iwata, and K. Irikura (2005). Estimation of source rupture process and strong ground motion simulation of the 2002 Denali, Alaska, earthquake. *Bull. Seismol. Soc. Am.* **95**, 1701–1715.

Atzori, S., C. Tolomei, A. Antonioli, J. P. Merryman Boncori, S. Bannister, E. Trasatti, P. Pasquali, and S. Salvi (2012). The 2010–2011 Canterbury, New Zealand, seismic sequence: Multiple source analysis from InSAR data and modeling, *J. Geophys. Res.* 117, B08305, doi: 10.1029/2012JB009178.

Avouac, J.-P., F. Ayoub, S. Wei, J.-P. Ampuero, L. Meng, S. Leprince, R. Jolivet, Z. Duputel, and D. Helmberger (2014). The 2013, Mw 7.7 Balochistan earthquake,

energetic strike-slip reactivation of a thrust fault. *Earth Planet. Sci. Lett.* **391**,128–134.

Baba, T., Y. Tanioka, P. R. Cummins, and K. Uhira (2002). The slip distribution of the 1946 Nankai earthquake estimated from tsunami inversion using a new plate model. *Phys. Earth Planet. Int.* **132**, 59–73.

Bejar-Pizzaro, M., D. Carrizo, A. Socquet, R. Armijo, S. Barrientos, F. Bondoux, S. Bonvalot, J. Campos, D. Comte, J. B. de Chabalier, *et al*. (2010). Asperities, barriers and transition zone in the North Chile seismic gap: State of the art after the 2007 Mw 7.7 Tocopilla earthquake inferred by GPS and InSAR data, *Geophys. Jour. Int.*, doi: 10.1111/j.1365-246X.2010.04748.x.

Bennett, R. A., R. E. Reilinger, W. Rodi, Y. P. Li, M. N. Toksoz, and K. Hudnut (1995). Coseismic fault slip associated with the 1992 M_W 6.1 Joshua-Tree, California, Earthquake - Implications for the Joshua-Tree Landers Earthquake Sequence. *J. Geophys. Res.***100**, 6443–6461.

Beroza, G. C. (1991). Near-source modeling of the Loma-Prieta earthquake - evidence for heterogeneous slip and implications for earthquake hazard. *Bull. Seismol. Soc. Am* **81**, 1603–1621.

Beroza, G. C., and P. Spudich (1988). Linearized Inversion for Fault Rupture Behavior - Application to the 1984 Morgan-Hill, California, Earthquake. *J. Geophys. Res*. **93**, 6275–6296.

Birgoren, G., H. Sekiguchi, and K. Irikura (2004). Rupture model of the 1999 Duzce, Turkey, earthquake deduced from high and low frequency strong motion data. *Geophys. Res. Lett* **31**, L05610, doi: 10.1029/2003GL019194.

Blaser, L., F. Krüger, M. Ohrnberger, and F. Scherbaum (2010). Scaling relations of earthquake source parameter estimates with special focus on subduction environment. *Bull. Seismol. Soc. Am.***100**, 2914–2926.

Bouchon, M., M. N. Toksoz, H. Karabulut, M. P. Bouin, M. Dietrich, M. Aktar, and M. Edie (2002). Space and time evolution of rupture and faulting during the 1999 Izmit (Turkey) earthquake. *Bull. Seismol. Soc. Am* **92**, 256–266.

Cakir, Z., J. B. de Chabalier, R. Armijo, B. Meyer, A. Barka, and G. Peltzer (2003). Coseismic and early post-seismic slip associated with the 1999 Izmit earthquake (Turkey), from SAR interferometry and tectonic field observations. *Geophys. J. Int.* **155**, 93–110.

Calais, E., A. Freed, G. Mattioli, F. Amelung, S. Jonsson, P. Jansma, S.-H. Hong, T. Dixon, C. Prepetit, and R. Moplaisir (2010). Transpressional rupture of an unmapped fault during the 2010 Haiti earthquake, *Nature Geosci*. **3**, 794–799.

Chi, W. C., D. Dreger, and A. Kaverina (2001). Finite-source modeling of the 1999 Taiwan (Chi-Chi) earthquake derived from a dense strong-motion network. *Bull. Seismol. Soc. Am.* **91**,1144–1157.

Cho, I., and I. Nakanishi (2000). Investigation of the three-dimensional fault geometry ruptured by the 1995 Hyogo-Ken Nanbu earthquake using strong-motion and geodetic data. *Bull. Seismol. Soc. Am* **90**, 450–467.

Cirella, A., A. Piatanesi, E. Tinti, and M. Cocco (2008). Rupture process of the 2007 Niigata-ken Chuetsu-oki earthquake by non-linear joint inversion of strong motion and GPS data, *Geophys. Res. Lett* **35**, L16306, doi: 10.1029/2008GL034756.

Cirella, A., A. Piatanesi, E. Tinti, M. Chini, and M. Cocco (2012). Complexity of the rupture process during the 2009 L'Aquila, Italy, earthquake, *Geophys. Jour. Int.* **190**, 607–621.

Cohee, B. P., and G. C. Beroza (1994). Slip distribution of the 1992 Landers earthquake and its implications for earthquake source mechanics. *Bull. Seismol. Soc. Am.* **84**, 692–712.

Courboulex, F., M. A. Santoyo, J. F. Pacheco, and S. K. Singh (1997). The 14 September 1995 (M=7.3) Copala, Mexico, Earthquake: A source study using teleseismic, regional, and local data. *Bull. Seismol. Soc. Am.* **87**, 999–1010.

Cultrera, G., G. Ameri, A. Saraò, A. Cirella, and A. Emolo (2013). Ground-motion simulations within ShakeMap methodology: application to the 2008 Iwate-Miyagi Nairiku (Japan) and 1980 Irpinia (Italy) earthquakes. *Geophys. Jour. Int.* **193**, 220–237.

Custodio, S., P. C. Liu, and R. J. Archuleta (2005). The 2004 Mw 6.0 Parkfield, California, earthquake: Inversion of near-source ground motion using multiple data sets. *Geophys. Res. Lett.* **32**, L23312, doi:10.1029/2005GL024417

Delouis B., J.-M. Nocquet, and M. Vallée (2010). Slip distribution of the February 27, 2010 Mw = 8.8 Maule Earthquake, central Chile, from static and high-rate GPS, InSAR, and broadband teleseismic data, *Geophys. Res. Lett.* **37**, L17305, doi:10.1029/2010GL043899.

Delouis, B., D. Giardini, P. Lundgren, and J. Salichon (2002). Joint inversion of InSAR, GPS, teleseismic, and strong-motion data for the spatial and temporal distribution of

earthquake slip: Application to the 1999 Izmit mainshock. *Bull. Seismol. Soc. Am.* **92**, 278–299.

Delouis, B., P. Lundgren, and D. Giardini (2004). Slip distributions of the 1999 Dücze (Mw 7.2) and Izmit (Mw 7.6) earthquakes on the North Anatolian Fault (Turkey): A combined analysis, *Internal report*.

Dreger, D. S. (1994). Empirical Greens-function study of the January 17, 1994 Northridge, California Earthquake. *Geophys. Res. Lett*. **21**, 2633–2636.

Dreger, D. S., L. Gee, P. Lombard, M. H. Murray, and B. Romanowicz (2005). Rapid finite-source analysis and near-fault strong ground motions: Application to the 2003 Mw 6.5 San Simeon and 2004 Mw 6.0 Parkfield earthquakes. *Seis. Res. Lett.* **76**, 40–48.

Elliott, J. R., A. C Copley, R. Holley, K. Scharer, and B. Parsons (2013). The 2011 Mw 7.1 Van (Eastern Turkey) earthquake. *Jour. Geophys. Res.* **118**, 1619–1637.

Elliott, J. R., R. J. Walters, P. C. England, J. A. Jackson, Z. Li, and B. Parsons (2010). Extension on the Tibetan plateau: recent normal faulting measured by InSAR and body wave seismology. *Geophys. Jour. Int.* **183**, 503–535.

Emolo, A., and A. Zollo (2005). Kinematic Source Parameters for the 1989 Loma Prieta Earthquake from the Nonlinear Inversion of Accelerograms. *Bull. Seismol. Soc. Am.* **95**, 981–994.

Fielding, E. J., A. Sladen, Z. Li, J.-P. Avouac, R. Bürgmann, and I. Ryder (2013). Kinematic fault slip evolution source models of the 2008 M7.9 Wenchuan earthquake in China from SAR Interferometry, GPS and teleseismic analysis and implications for Longmen Shan tectonics, *Geophys. J. Int.*, doi:10.1093/gji/ggt155.

Fujii, Y., K. Satake, S. Sakai, M. Shinohara, and T. Kanazawa (2011). Tsunami source of the 2011 off the Pacific coast of Tohoku Earthquake, *Earth Planets Space* **63**, 815–820.

Fukuyama, E., and K. Irikura (1986). Rupture process of the 1983 Japan Sea (Akita-Oki) earthquake using a waveform inversion method. *Bull. Seismol. Soc. Am.* **76**, 1623–1640.

Goda, K., T. Yasuda, N. Mori, and T. Maruyama (2016). New scaling relationships of earthquake source parameters for stochastic tsunami simulation, *Coast. Eng. Jour.* **58**, doi: http://dx.doi.org/10.1142/S0578563416500108

Gualandi A., E. Serpelloni, M.E. Belardinelli (2013). *Pers. Comm.*

Gusman A. R., Y. Tanioka, S. Sakai, and H. Tsushima (2012). Source model of the great 2011 Tohoku earthquake estimated from tsunami waveforms and crustal deformation data, *Earth Planet. Sci. Lett.* 341–344, 234–242.

Gusman, A. R., Y. Tanioka, T. Kobayashi, H. Latief, and W. Pandoe (2010). Slip distribution of the 2007 Bengkulu earthquake inferred from tsunami waveforms and InSAR data, *Jour. Geophys. Res.* **115**, B12316, doi:10.1029/2010JB007565.

Hanks, T. C., and W. H. Bakun (2002). A bilinear source-scaling model for M-log A observations of continental earthquakes, *Bull. Seismol. Soc. Am.* **92**, 1841–1846.

Hartzell, S. (1989). Comparison of seismic waveform inversion results for the rupture history of a finite fault - application to the 1986 North Palm-Springs, California, Earthquake. *J. Geophys. Res*. **94**, 7515–7534.

Hartzell, S. H., and M. Iida (1990). Source complexity of the 1987 Whittier Narrows, California, earthquake from the inversion of strong motion records. *J. Geophys. Res.* 95, 12475–12485.

Hartzell, S. H., and T. H. Heaton (1986). Rupture history of the 1984 Morgan Hill, California, earthquake from the inversion of strong motion records. Bull. Seismol. Soc. Am **76**, 649–674.

Hartzell, S. H., and T.H. Heaton (1983). Inversion of strong ground motion and teleseismic waveform data for the fault rupture history of the 1979 Imperial Valley, California, earthquake. *Bull. Seismol. Soc. Am.* **73**, 1553–1583.

Hartzell, S., and C. Langer (1993). Importance of model parameterization in finite fault inversions; application to the 1974 Mw 8.0 Peru earthquake. *J. Geophys. Res.* **98**, 22123–22134.

Hartzell, S., and C. Mendoza (1991). Application of an iterative least-squares wave-form inversion of strong-motion and teleseismic records to the 1978 Tabas, Iran, Earthquake. *Bull. Seismol. Soc. Am.* **81**, 305–331.

Hartzell, S., P. C. Liu, and C. Mendoza (1996). The 1994 Northridge, California, earthquake; investigation of rupture velocity, risetime, and high-frequency radiation. *J. Geophys. Res.* **101**, 20091–20108.

Hayes, G. (2011). Rapid source characterization of the 03-11-2011 Mw 9.0 Off the pacific coast of Tohoku earthquake, *Earth Planets Space* **63**, 529–534.

Hayes, G. P., R. W. Briggs, A. Sladen, E. J. Fielding, C. Prentice, K. Hudnut, P. Mann, F. W. Taylor, A. J. Crone, R. Gold, T. Ito and M. Simons (2010). Complex rupture during the 12 January 2010 Haiti earthquake, *Nature Geosci.* **3**, 800-805.

Heaton, T. H. (1982). The 1971 San-Fernando Earthquake - a Double Event? *Bull. Seismol. Soc. Am.* **72**, 2037–2062.

Hernandez, B., M. Cocco, F. Cotton, S. Stramondo, O. Scotti, F. Courboulex, and M. Campillo (2004). Rupture history of the 1997 Umbria-Marche (central Italy) main shocks from the inversion of GPS, DInSAR and near field strong motion data, *Ann. Geophys.* **47**, 1355–1376.

Hernandez, B., N. M. Shapiro, S. K. Singh, J. F. Pacheco, F. Cotton, M. Campillo, A. Iglesias, V. Cruz, J. M. Gomez, and L. Alcantara (2001). Rupture history of September 30, 1999 intraplate earthquake of Oaxaca, Mexico (Mw 7.5) from inversion of strong-motion data. *Geophys. Res. Lett.* **28**, 363–366.

Hikima, K. and K. Koketsu (2004). Source processes of the foreshock, mainshock and largest aftershock in the 2003 Miyagi-ken Hokubu, Japan, earthquake sequence, *Earth Planets Space* **56**, 87–93.

Horikawa, H. (2001). Earthquake doublet in Kagoshima, Japan: Rupture of asperities in a stress shadow. *Bull. Seismol. Soc. Am.* **91**, 112–127.

Horikawa, H., K. Hirahara, Y. Umeda, M. Hashimoto, and F. Kusano (1996). Simultaneous inversion of geodetic and strong-motion data for the source process of the Hyogo-ken Nanbu, Japan, earthquake, *J. Phys. Earth* **44**, 455–471.

Hough, S. E., and D. S. Dreger (1995). Source parameters of the 23 April 1992 M 6.1 Joshua Tree, California, earthquake and its aftershocks; empirical Green's function analysis of GEOS and TERRAscope data, *Bull. Seismol. Soc. Am.* **85**,1576–1590.

Hudnut, K. W., Z. Shen, M. Murray, S. McClusky, R. King, T. Herring, B. Hager, Y. Feng, P. Fang, A. Donnellan, and Y. Block (1996). Co-seismic displacements of the 1994 Northridge, California, earthquake, *Bull. Seismol. Soc. Am*. **86**, 19–36.

Ichinose, G. A., H. K. Thio, P. G. Somerville, T. Sato, and T. Ishii (2003). Rupture process of the 1944 Tonankai earthquake (Ms 8.1) from the inversion of teleseismic and regional seismograms. *J. Geophys. Res.* **108**, B2497, doi: 10.1029/2003JB002393.

Ichinose, G. A., P. Somerville, H. K. Thio, S. Matsushima, and T. Sato (2005). Rupture process of the 1948 Fukui earthquake (M 7.1) from the joint inversion of seismic waveform and geodetic data, *J. Geophys. Res.* **110**, B05301, doi: 10.1029/2004JB003437.

Ide S., A. Baltay, and G. C. Beroza (2011). Shallow dynamic overshoot and energetic deep rupture in the 2011 Mw 9.0 Tohoku-Oki earthquake, *Science* **332**, 1426–1429.

Ide, S. (1999). Source process of the 1997 Yamaguchi, Japan, earthquake analyzed in different frequency bands, *Geophys. Res. Lett*. **26**, 1973–1976

Ide, S., M. Takeo, and Y. Yoshida (1996). Source process of the 1995 Kobe earthquake: Determination of spatio-temporal slip distribution by Bayesian modeling. *Bull. Seismol. Soc. Am.* **86**, 547–566.

Iwata, T., H. Sekiguchi, Y. Matsumoto, H. Miyake, and K. Irikura (2000). Source process of the 2000 western Tottori Prefecture earthquake and near-source strong ground motion, 2000 Fall Meeting, Seismol. Soc. Japan, Tsukuba.

Ji, C., D. J. Wald, and D. V. Helmberger (2002). Source description of the 1999 Hector Mine, California, earthquake, part II: Complexity of slip history. *Bull. Seismol. Soc. Am.* **92**, 1208–1226.

Johnson, K. M., Y. J. Hsu, P. Segall, and S. B. Yu. (2001). Fault geometry and slip distribution of the 1999 Chi-Chi, Taiwan earthquake imaged from inversion of GPS data. *Geophys. Res. Lett.* **28**, 2285–2288.

Jonsson, S., H. Zebker, P. Segall, and F. Amelung (2002). Fault slip distribution of the 1999 Mw 7.1 Hector Mine, California, earthquake, estimated from satellite radar and GPS measurements. *Bull. Seismol. Soc. Am.* **92**, 1377–1389.

Kakehi, Y. (2004). Analysis of the 2001 Geiyo, Japan, earthquake using high-density strong ground motion data: detailed rupture process of a slab earthquake in a medium with a large velocity contrast. *J. Geophys. Res.* **109**, B08306, doi:10.1029/2004JB002980.

Kato, T., and M. Ando (1997). Source mechanisms of the 1944 Tonankai and 1946 Nankaido earthquakes: Spatial heterogeneity of rise times. *Geophys. Res. Lett.* **24**, 2055–2058.

Kaverina, A., D. Dreger, and E. Price. (2002). The combined inversion of seismic and geodetic data for the source process of the 16 October 1999 Mw 7.1 Hector Mine, California, earthquake. *Bull. Seismol. Soc. Am*. **92**, 1266–1280.

Kikuchi, M., M. Nakamura, and K. Yoshikawa (2003). Source rupture processes of the 1944 Tonankai earthquake and the 1945 Mikawa earthquake derived from low-gain seismograms. *Earth Planets Space* **55**, 159–172.

Kobayashi, R., and K. Koketsu (2005). Source process of the 1923 Kanto earthquake inferred from historical geodetic, teleseismic, and strong motion data. *Earth Planets Space* **57**, 261–270.

Koketsu, K., K. Hikima, S. Miyazaki, and S. Ide. (2004). Joint inversion of strong motion and geodetic data for the source process of the 2003 Tokachi-oki, Hokkaido, earthquake. *Earth Planets Space* **56**, 329–334.

Koketsu, K., S. Yoshida, and H. Higashihara (1998). A fault model of the 1995 Kobe earthquake derived from the GPS data on the Akashi Kaikyo Bridge and other datasets. *Earth Planets Space* **50**, 803–811.

Konca, A. O. (2015). Rupture process of 2011 Mw 7. 1 Van, Eastern Turkey earthquake from joint inversion of strong-motion, high-rate GPS, teleseismic, and GPS data. *Jour. Seis.***19**, 969–988.

Konca, A. O., J-P. Avouac, A. Sladen, A. J. Meltzner, K. Sieh, P. Fang, Z. Li, J. Galetzka, J. Genrich, M. Chlieh, D. H. Natawidjaja, Y. Bock, E. Fielding, C. Ji, and D. V. Helmberger (2008). Partial rupture of a locked patch of the Sumatra megathrust during the 2007 earthquake sequence, *Nature* **456**, 631–635.

Konca, A. O., V. Hjorleifsdottir, T. A. Song, J. Avouac, D. V. Helmberger, C. Ji, K. Sieh, R. Briggs, and A. Meltzner (2007). Rupture kinematics of the 2005, Mw 8.6, Nias-Simeulue earthquake from the joint inversion of seismic and geodetic data, *Bull. Seism. Soc. Am*. **97**, S307–S322.

Larsen, S., R. Reilinger, H. Neugebauer, and W. Strange (1992). Global positioning system measurements of deformations associated with the 1987 Superstition Hills Earthquake - evidence for conjugate faulting, *J. Geophys. Res*. **97**, 4885–4902.

Lay T., C. J. Ammon, H. Kanamori, L. Xue, and M. J. Kim (2011). Possible large near-trench slip during the 2011 Mw 9.0 off the Pacific coast of Tohoku Earthquake. *Earth Planets Space* **63**, 687–692.

Lay, T., H. Kanamori, C. J. Ammon, A. R. Hutko, K. Furlong, and L. Rivera (2009). The 2006–2007 Kuril Islands great earthquake sequence, *Jour. Geophys. Res*. **114**, B11308, doi:10.1029/2008JB006280.

Lay, T., L. Ye, H. Kanamori, Y. Yamazaki, K. F. Cheung, and C. J. Ammon (2013b). The February 6, 2013 Mw 8.0 Santa Cruz Islands earthquake and tsunami. *Tectonophysics* **608**, 1109–1121.

Lay, T., L. Ye, H. Kanamori, Y. Yamazaki, K. F. Cheung, K. Kwong, and K. D. Koper (2013a). The October 28, 2012 Mw 7.8 Haida Gwaii underthrusting earthquake and tsunami: Slip partitioning along the Queen Charlotte Fault transpressional plate boundary. *Earth Planet. Sci. Lett.* **375**, 57–70

Leonard, M. (2010). Earthquake fault scaling: relating rupture length, width, average displacement, and moment release. *Bull. Seismol. Soc. Am*. **100**, 1971–1988.

Liu, C., Y. Zheng, X. Xiong, R. Wang, A. López and J. Li (2015). Rupture processes of the 2012 September 5 Mw 7.6 Nicoya, Costa Rica earthquake constrained by improved geodetic and seismological observations. *Geophys. Jour. Int.* **203**, 175–183.

Liu, H., and D. V. Helmberger (1983). The near-source ground motion of the 6 August 1979 Coyote Lake, California, earthquake. *Bull. Seismol. Soc. Am.* **73,** 201–218.

Lorito, S., F. Romano, S. Atzori, X. Tong, A. Avallone, J. McCloskey, M. Cocco, E. Boschi, and A. Piatanesi (2011). Limited overlap between the seismic gap and coseismic slip of the great 2010 Chile earthquake, *Nat. Geosci.* **4**, 173–177.

Luttrell, K. M., Tong, X., Sandwell, D. T., Brooks, B. A., & Bevis, M. G. (2011). Estimates of stress drop and crustal tectonic stress from the 27 February 2010 Maule, Chile, earthquake: Implications for fault strength. Journal of Geophysical Research: Solid Earth (1978–2012), 116(B11).

Ma, K. F., J. Mori, S. J. Lee, and S. B. Yu (2001). Spatial and temporal distribution of slip for the 1999 Chi-Chi, Taiwan, earthquake. *Bull. Seismol. Soc. Am.* **91**, 1069–1087.

Mai, P. M., and G. C. Beroza (2000). Source scaling properties from finite-fault-rupture models. *Bull. Seismol. Soc. Am*. **90**, 604–615.

Mai, P. M., and K. K. S. Thingbaijam (2014). SRCMOD: an online database of finite-fault rupture models. *Seism. Res. Lett.* **85**, 1348–1357.

Mendoza, C. (1993). Coseismic slip of 2 large mexican earthquakes from teleseismic body wave-forms - implications for asperity interaction in the Michoacan plate boundary segment. *J. Geophys. Res*. **98,** 8197–8210.

Mendoza, C. (1995). Finite-fault analysis of the 1979 March 14 Petatlan, Mexico, earthquake using teleseismic P-wave-forms. *Geophys. J. Int*. **121**, 675–683.

Mendoza, C., and S. H. Hartzell (1988). Inversion for slip distribution using teleseismic P waveforms; North Palm Springs, Borah Peak, and Michoacan earthquakes. *Bull. Seismol. Soc. Am.* **78**, 1092–1111.

Mendoza, C., and S. H. Hartzell (1989). Slip distribution of the 19 September 1985 Michoacan, Mexico, earthquake-near-source and teleseismic constraints. *Bull. Seismol. Soc. Am.* **79**, 655–669.

Mendoza, C., and S. Hartzell (1999). Fault-slip distribution of the 1995 Colima-Jalisco, Mexico, earthquake. *Bull. Seismol. Soc. Am.* **89**, 1338–1344.

Mendoza, C., S. Hartzell, and T. Monfret (1994). Wide-band analysis of the 3 March 1985 Central Chile Earthquake - Overall source process and rupture history. *Bull. Seismol. Soc. Am.* **84**, 269–283.

Miura, S., Y. Suwa, T. Sato, K. Tachibana, and A. Hasegawa (2004). Slip distribution of the 2003 northern Miyagi earthquake (M6.4) deduced from geodetic inversion. *Earth Planets Space* **56**, 95–101.

Miyakoshi, K, T. Kagawa, H. Sekiguchi, T. Iwata, and K. Irikura (2000). Source characterization of inland earthquakes in Japan using source inversion results, *Proc. 12th World Conf. Earthq. Eng*., Auckland, New Zealand.

Motagh, M., B. Schurr, J. Anderssohn, B. Cailleau, T. R. Walter, R. Wang, and J.-P. Villotte (2010). Subduction earthquake deformation associated with 14 November 2007, Mw 7.8 Tocopilla earthquake in Chile: Results from InSAR and aftershocks, *Tectonophysics* **490**, 60–68.

Nagai, R., M. Kikuchi, and Y. Yamanaka (2001). Comparative Study on the Source Processes of Reccurent Large Earthquakes in Sariku-oki Region: the 1968 Tokachi-oki Earthquake and the 1994 Sanriku-oki Earthquake. *Zishin* **54**, 267–280.

Nakahara, H., T. Nishimura, H. Sato, M. Ohtake, S. Kinoshita, and H. Hamaguchi (2002). Broadband source process of the 1998 Iwate prefecture, Japan, earthquake as

revealed from inversion analyses of seismic waveforms and envelopes. *Bull. Seismol. Soc. Am.* **92**, 1708–1720.

Nakayama, W., and M. Takeo (1997). Slip history of the 1994 Sanriku-Haruka-Oki, Japan, earthquake deduced from strong-motion data. *Bull. Seismol. Soc. Am.* **87**, 918-931.

Oglesby, D. D., D. S. Dreger, R. A. Harris, N. Ratchkovski, and R. Hansen (2004). Inverse kinematic and forward dynamic models of the 2002 Denali fault earthquake, Alaska. *Bull. Seismol. Soc. Am.* **94**, S214–S233.

Okuwaki, R., Y. Yagi, R. Aránguiz, J. González, and G. González (2016). Rupture process during the 2015 Illapel, Chile Earthquake: zigzag-along-dip rupture episodes. *Pageoph* **173**, 1011–1020.

Piatanesi, A., A. Cirella, P. Spudich and M. Cocco (2007). A global search inversion for earthquake kinematic rupture history: Application to the 2000 western Tottori, Japan earthquake. Jour. Geophys. Res.**112**, B07314, doi: 10.1029/2006JB004821

Poiata, N., H. Miyake, K. Koketsu and K. Hikima (2012a). Strong-Motion and teleseismic waveform inversions for the source process of the 2003 Bam, Iran, earthquake. *Bull. Seismol. Soc. Am.* **102**, 1477–1496.

Poiata, N., K. Koketsu, A. Vuan, and H. Miyake (2012b). Low-frequency and broad-band source models for the 2009 L'Aquila, Italy, earthquake, *Geophys. J. Int.* **191**, 224–242.

Pollitz, F.F., Brooks, B., Tong, X., Bevis, M.G., Foster, J.H., Bürgmann, R., Smalley, R., Vigny, C., Socquet, A., Ruegg, J.C. and Campos, J., 2011. Coseismic slip

distribution of the February 27, 2010 Mw 8.8 Maule, Chile earthquake, *Geophys. Res. Lett.* **38**, L09309, doi:10.1029/2011GL047065.

Reilinger, R. E., S. Ergintav, R. Burgmann, S. McClusky, O. Lenk, A. Barka, O. Gurkan, L. Hearn, K. L. Feigl, R. Cakmak, B. Aktug, H. Ozener, and M. N. Toksoz (2000). Coseismic and postseismic fault slip for the 17 August 1999, M=7.5, Izmit, Turkey earthquake. *Science* **289**, 1519–1524.

Rhie, J., D. Dreger, R. Burgmann, and B. Romanowicz (2007). Slip of the 2004 Sumatra–Andaman Earthquake from joint inversion of long-period global seismic waveforms and GPS static Offsets, *Bull. Seismol. Soc. Am.* **97**, S115–S127.

Salichon, J., B. Delouis, P. Lundgren, D. Giardini, M. Costantini, and P. Rosen (2003). Joint inversion of broadband teleseismic and interferometric synthetic aperture radar (InSAR) data for the slip history of the Mw=7.7, Nazca ridge (Peru) earthquake of 12 November 1996. *J. Geophys. Res.* **108**, doi:10.1029/2001JB000913.

Salichon, J., P. Lundgren, B. Delouis, and D. Giardini (2004). Slip History of the 16 October 1999 Mw 7.1 Hector Mine Earthquake (California) from the Inversion of InSAR, GPS, and Teleseismic Data. *Bull. Seismol. Soc. Am*. **94**, 2015–2027.

Satake, K., Y. Fujii, T. Harada, and Y. Namegaya (2013). Time and space distribution of coseismic slip of the 2011 Tohoku Earthquake as inferred from tsunami Waveform data, *Bull. Seismol. Soc. Am*. **103**, 1473–1492.

Sekiguchi (2002) Pers. Comm.

Sekiguchi (2003) Pers. Comm.

Sekiguchi, H. and T. Iwata (2001). Rupture Process of the 2001 Geiyo Earthquake obtained from Strong Motion Data [Ver.1], http://sms.dpri.kyoto-u.ac.jp/iwata/zisin/geiyo-e.html.

Sekiguchi, H., and T. Iwata (2002). Rupture process of the 1999 Kocaeli, Turkey, earthquake estimated from strong-motion waveforms. *Bull. Seismol. Soc. Am.* **92**, 300–311.

Sekiguchi, H., Irikura, K., and Iwata, T. (2002). Source inversion for estimating the continuous slip distribution on a fault – introduction of Green's functions convolved with a correction function to give moving dislocation effects in subfaults. *Geophys. Jour. Int.* **150**, 377–391.

Semmane, F., F. Cotton, and M. Campillo. (2005a). The 2000 Tottori earthquake: A shallow earthquake with no surface rupture and slip properties controlled by depth. *J. Geophys. Res*. **110**, B03306, doi:10.1029/2004JB003194.

Semmane,F., M. Campillo, and F. Cotton (2005b). Fault location and source process of the Boumerdes, Algeria Earthquake inferred from geodetic and strong motion data, *Geophys. Res. Lett.* **32**, L01305, doi:10.1029/2004GL021268

Shao, G., X. Li, C. Ji. and T. Maeda (2011). Focal mechanism and slip history of 2011 Mw 9.1 off the Pacific coast of Tohoku earthquake, constrained with teleseismic body and surface waves, *Earth Planets Space* **63**, 559–564.

Shen, Z. K., B. X. Ge, D. D. Jackson, D. Potter, M. Cline, and L. Y. Sung (1996). Northridge earthquake rupture models based on the global positioning system measurements. *Bull. Seismol. Soc. Am.* 86, S37–S48.

Skarlatoudis, A.A., P.G. Somerville, and H.K. Thio (2016). Source-scaling relations of interface subduction earthquakes for strong ground motion and tsunami simulation. *Bull. Seismol. Soc. Am* **106,** doi: 10.1785/0120150320

Sladen, A., H. Tavera, M. Simons, J. P. Avouac, A. O. Konca, H. Perfettini, L. Audin, E. J. Fielding, F. Ortega, and R. Cavagnoud (2010), Source model of the 2007 Mw 8.0 Pisco, Peru earthquake: Implications for seismogenic behavior of subduction megathrusts, *J. Geophys. Res*. **115**, B02405, doi:10.1029/2009JB006429.

Spence, W., C. Mendoza, E. R. Engdahl, G. L. Choy, and E. Norabuena (1999). Seismic subduction of the Nazca Ridge as shown by the 1996-97 Peru earthquakes, *Pageoph* **154**, 753–776.

Steidl, J. H., R. J. Archuleta, and S. H. Hartzell (1991). Rupture History of the 1989 Loma-Prieta, California, Earthquake. *Bull. Seismol. Soc. Am.* **81**,1573–1602.

Strasser, F. O., M. C. Arango, and J. J. Bommer (2010). Scaling of the source dimensions of interface and intraslab subduction-zone earthquakes with moment magnitude. *Seism. Res. Lett.* **81**, 941–950.

Sudhaus, H., and S. Jonsson (2009). Improved source modelling through combined use of InSAR and GPS under consideration of correlated data errors: application to the June 2000 Kleifarvatn earthquake, Iceland, *Geophys. J. Int.***176**, 389–404.

Sudhaus, H., and S. Jonsson (2011). Source model for the 1997 Zirkuh earthquake (Mw=7.2) in Iran derived from JERS and ERS InSAR observations, *Geophys. J. Int.* **185**, 676–692.

Takeo, M. (1988). Rupture process of the 1980 Izu-Hanto-Toho-Oki earthquake deduced from strong motion seismograms. *Bull. Seismol. Soc. Am.* **78**, 1074–1091.

Takeo, M. (1990). Fault heterogeneity of inland earthquakes in Japan. *Bull. Earthq. Res. Inst.* **65**, 541–569.

Tanioka, Y., and K. Satake (2001a). Detailed coseismic slip distribution of the 1944 Tonankai earthquake estimated from tsunami waveforms. *Geophys. Res. Lett.* **28**, 1075–1078.

Tanioka, Y., and K. Satake (2001b). Coseismic slip distribution of the 1946 Nankai earthquake and aseismic slips caused by the earthquake. *Earth Planets Space* **53**, 235–241.

Tanioka, Y., K. Hirata, R. Hino, and T. Kanazawa (2004). Slip distribution of the 2003 Tokachi-oki earthquake estimated from tsunami waveform inversion. *Earth Planets Space* **56**, 373–376.

Utkucu, M. (2013). 23 October 2011 Van, Eastern Anatolia, earthquake (M_W 7.1) and seismotectonics of Lake Van area. *Jour. Seism.* **17**, 783–805.

Wald, D. J. (1992). Strong motion and broad-band teleseismic analysis of the 1991 Sierra-Madre, California, earthquake. *J. Geophys. Res.* **97**, 11033–11046.

Wald, D. J. (1996). Slip history of the 1995 Kobe, Japan, earthquake determined from strong motion, teleseismic, and geodetic data. *J. Phys. Earth.* **44**, 489–503.

Wald, D. J., and P. G. Somerville (1995). Variable-slip rupture model of the Great 1923 Kanto, Japan, Earthquake - geodetic and body-wave-form analysis. *Bull. Seismol. Soc. Am.* **85**, 159–177.

Wald, D. J., and T. H. Heaton (1994). Spatial and temporal distribution of slip for the 1992 Landers, California, Earthquake. *Bull. Seismol. Soc. Am.* **84**, 668–691.

Wald, D. J., D. V. Helmberger, and S. H. Hartzell (1990). Rupture process of the 1987 Superstition Hills Earthquake from the inversion of strong-motion data. *Bull. Seismol. Soc. Am*. **80**, 1079–1098.

Wald, D. J., D. V. Helmberger, and T. H. Heaton (1991). Rupture model of the 1989 Loma-Prieta Earthquake from the inversion of strong-Motion and broad-band teleseismic data. *Bull. Seismol. Soc. Am.* **81**,1540–1572.

Wald, D. J., T. H. Heaton, and K. W. Hudnut (1996). The slip history of the 1994 Northridge, California, earthquake determined from strong-motion, teleseismic, GPS, and leveling data. *Bull. Seismol. Soc. Am.* **86**, S49–S70.

Wang, H., J.R. Elliott, T.J. Craig, T. J. Wright, J. Liu-Zeng, and A. Hooper (2014). Normal faulting sequence in the Pumqu-Xainza Rift constrained by InSAR and teleseismic body-wave seismology. *Geoch. Geophys. Geosys.* **15**, 2947–2963.

Wei, S. J., D. V. Helmberger, S. Owen, R. W. Graves, K. W. Hudnut and E. Fielding, (2013a). Complementary slip distributions of the largest earthquakes in the 2012 Brawley swarm, Imperial Valley, California, *Geophys. Res. Lett.* **40**, doi:10.1002/grl.50259

Wei, S. J., D. V. Helmberger, Z.W. Zhan, and R. W. Graves, (2013b) Rupture complexity of the Mw 8.3 Sea of Okhotsk earthquake: rapid triggering of complementary earthquakes? *Geophys, Res, Lett.* **40**, doi: 10.1002/grl.50977.

Wei, S. J., R.W. Graves, D. Helmberger, J.P. Avouac and J.L. Jiang (2012) Sources of shaking and flooding during the Tohoku-Oki earthquake: A mixture of rupture styles, *Earth Planet. Sci. Lett.* 333–334, 91–100.

Wei, S., E. Fielding, S. Leprince, A. Sladen, J.P. Avouac, D. Helmberger , E. Hauksson, R. Chu, M. Simons, K. Hudnut, T. Herring & R. Briggs (2011). Superficial simplicity of the 2010 El Mayor-Cucapah earthquake of Baja California in Mexico. *Nat. Geosci.*, doi:10.1038/ngeo1213,

Wells, D. L., and K. J. Coppersmith (1994). New empirical relationships among magnitude, rupture length, rupture width, rupture area, and surface displacement, *Bull. Seismol. Soc. Am.* **84**, 974–1002.

Wu, C. J., M. Takeo, and S. Ide (2001). Source process of the Chi-Chi earthquake: A joint inversion of strong motion data and global positioning system data with a multi-fault model. *Bull. Seismol. Soc. Am.* **91**, 1128–1143.

Yagi Y., N. Nishimura, and A. Kasahara (2012). Source process of the 12 May 2008 Wenchuan, China, earthquake determined by waveform inversion of teleseismic body waves with a data covariance matrix, *Earth Planets Space* **64**, e13–e16.

Yagi, Y. (2004). Source rupture process of the 2003 Tokachi-oki earthquake determined by joint inversion of teleseismic body wave and strong ground motion data, *Earth Planets Space* **56**, 311–316.

Yagi, Y. and Y. Fukahata (2011a). Introduction of uncertainty of Green's function into waveform inversion for seismic source processes, *Geophys. J. Int.* **186**, 711–720.

Yagi, Y. and Y. Fukahata (2011b). Rupture process of the 2011 Tohoku-oki earthquake and absolute elastic strain release, *Geophys. Res. Lett.* **38**, L19307, doi:10.1029/2011GL048701.

Yagi, Y., and M. Kikuchi (2000). Source rupture process of the Kocaeli, Turkey, earthquake of August 17, 1999, obtained by joint inversion of near-field data and teleseismic data. *Geophys. Res. Lett*. **27**, 1969–1972.

Yagi, Y., and R. Okuwaki (2015), Integrated seismic source model of the 2015 Gorkha, Nepal, earthquake, *Geophys. Res. Lett.* **42**, doi:10.1002/2015GL064995.

Yagi, Y., M. Kikuchi, S. Yoshida, and T. Sagiya (1999). Comparison of the coseismic rupture with the aftershock distribution in the Hyuga-nada earthquakes of 1996. *Geophys. Res. Lett.* 26, 3161–3164.

Yagi, Y., M. Kikuchi, S. Yoshida, and Y. Yamanaka (1998). Source process of the Hyuga-nada Earthquake of April 1, 1968 (Mjma 7.5), and its relationship to the subsequent seismicity, *Zishin* **51**, 139–148.

Yagi, Y., T. Mikurno, J. Pacheco, and G. Reyes (2004). Source rupture process of the Tecoman, Colima, Mexico earthquake of 22 January 2003, determined by joint inversion of teleseismic body-wave and near-source data. *Bull. Seismol. Soc. Am.* **94**, 1795–1807.

Yamanaka, Y., and M. Kikuchi (2003). Source process of the recurrent Tokachi-oki earthquake on September 26, 2003, inferred from teleseismic body waves. *Earth Planets Space* **55,** E21–E24.

Yamanaka, Y., and M. Kikuchi (2004). Asperity map along the subduction zone in northeastern Japan inferred from regional seismic data, *J. Geophys. Res.* **109**, B07307, doi:10.1029/2003JB002683.

Yamazaki, Y., T. Lay, K. F. Cheung, H. Yue, and H. Kanamori (2011). Modeling near-field tsunami observations to improve finite-fault slip models for the 11 March 2011 Tohoku earthquake, *Geophys. Res. Lett.* **38**, L00G15, doi:10.1029/2011GL049130.

Ye, L., T. Lay, H. Kanamori, and K.D. Koper (2013). Energy release of the 2013 Mw 8.3 Sea of Okhotsk earthquake and deep slab stress heterogeneity. *Science* **341**, 1380–1384.

Yoshida, S., K. Koketsu, B. Shibazaki, T. Sagiya, T. Kato, and Y. Yoshida (1996). Joint inversion of near- and far-field waveforms and geodetic data for the rupture process of the 1995 Kobe earthquake. *J. Phys. Earth.* **44**, 437–454.

Yue H., T. Lay, S. Y. Schwartz, L. Rivera, M. Protti, T. H. Dixon, S. Owen and A. V. Newman (2013). The 5 September 2012 Nicoya, CostaRica Mw 7.6 earthquake rupture process from joint inversion of high-rate GPS, strong-motion, and teleseismic P wave data and its relationship to adjacent plate boundary interface properties. *J. Geophys. Res.* 2013JB010187, doi:10.1002/jgrb.50379

Yue, H, T. Lay and K. D. Koper (2012), En Echelon and Orthogonal Fault Ruptures of the 11 April 2012 Great Intraplate Earthquakes. *Nature* **490**, 245–249.

Yue, H. and T. Lay (2013). Source Rupture Models for the Mw 9.0 2011 Tohoku Earthquake from Joint Inversions of High-Rate Geodetic and Seismic Data, *Bull. Seism. Soc. Am.* **103**, 1242–1255.

Zeng, Y. H., and C. H. Chen (2001). Fault rupture process of the 20 September 1999 Chi-Chi, Taiwan, earthquake. *Bull. Seismol. Soc. Am.* **91**, 1088–1098.

Zeng, Y., and J. Anderson (2000). Evaluation of numerical procedures for simulating near-fault long-period ground motions using Zeng method. Report 2000/01 to the PEER Utilities Program, available at http://peer.berkeley.edu

Table S1. The rupture models and estimated rupture dimensions.

evTAG	M_W	FT	S	*L* (km)	*W* (km)	*D* (m)	Reference
s1923KANTOJ01KOBA	8.08	RS	*	130.0	70.0	4.10	Kobayashi and Koketsu (2005)
s1923KANTOJ01WALD	7.95	RS	*	130.0	70.0	2.53	Wald and Somerville (1995)
s1944TONANK01ICHI	8.04	RS	*	220.0	140.0	1.05	Ichinose et al. (2003)
s1944TONANK01KIKU	7.99	RS	*	140.0	80.0	2.36	Kikuchi et al. (2003)
s1944TONANK01TANI	8.10	RS	*	270.0	180.0	0.82	Tanioka and Satake (2001a)
s1946NANKAI01BABA	8.40	RS	*	360.0	180.0	1.54	Baba et al. (2002)
s1946NANKAI01TANI	8.40	RS	*	360.0	180.0	1.64	Tanioka and Satake (2001b)
s1979IMPERI01ARCH	6.53	SS		35.0	11.0	0.63	Archuleta (1984)
s1979IMPERI01HART	6.58	SS		36.0	10.4	0.69	Hartzell and Heaton (1983)
s1979IMPERI01ZENG	6.35	SS		23.0	9.0	0.84	Zeng and Anderson (2000)
s1984MORGAN01BERO	6.28	SS		25.5	11.0	0.32	Beroza and Spudich (1988)
s1984MORGAN01HART	6.07	SS		27.0	11.5	0.16	Hartzell and Heaton (1986)
s1986NORTHP01HART	6.21	SS		22.0	15.2	0.15	Hartzell (1989)
s1986NORTHP01MEND	6.14	SS		22.0	15.2	0.13	Mendoza and Hartzell (1988)
s1987SUPERS01LARS	6.60	SS		25.0	10.0	1.12	Larsen et al. (1992)
s1987SUPERS01WALD	6.51	SS		18.0	10.4	1.02	Wald et al. (1990)
s1989LOMAPR01BERO	6.95	OS		32.0	15.0	1.66	Beroza (1991)
s1989LOMAPR01EMOL	6.91	OS		35.0	14.0	1.46	Emolo and Zollo (2005)
s1989LOMAPR01STEI	6.99	OS		38.0	17.0	1.38	Steidl et al. (1991)
s1989LOMAPR01WALD	6.94	OS		40.0	17.5	1.24	Wald et al. (1991)
s1989LOMAPR01ZENG	6.98	OS		32.0	13.0	2.43	Zeng and Anderson (2000)
s1992JOSHUA01BENN	6.25	SS		15.0	16.0	0.33	Bennet et al. (1995)
s1992JOSHUA01HOUG	6.15	SS		10.0	12.0	0.46	Hough and Dreger (1995)
s1992LANDER01COHE	7.08	SS		84.0	18.0	1.32	Cohee and Beroza (1994)
s1992LANDER01WALD	7.28	SS		93.0	15.0	2.02	Wald and Heaton (1994)
s1992LANDER01ZENG	7.20	SS		73.0	15.0	2.20	Zeng and Anderson (2000)
s1994NORTHR01DREG	6.66	RS		17.0	25.0	0.76	Dreger (1994)
s1994NORTHR01HART	6.73	RS		20.0	24.9	0.71	Hartzell et al. (1996)
s1994NORTHR01HUDN	6.81	RS		20.0	24.0	1.13	Hudnut et al. (1996)
s1994NORTHR01SHEN	6.84	RS		25.7	27.9	0.81	Shen et al. (1996)
s1994NORTHR01WALD	6.80	RS		18.0	24.0	1.03	Wald et al. (1996)
s1994NORTHR01ZENG	6.71	RS		15.0	17.5	1.20	Zeng and Anderson (2000)
s1994SANRIK01NAGA	7.70	RS	*	110.0	100.0	0.99	Nagai et al. (2001)
s1994SANRIK01NAKA	7.88	RS	*	110.0	160.0	0.63	Nakayama and Takeo (1997)
s1995KOBEJA01CHOx	6.80	SS		48.0	20.0	0.54	Cho and Nakanishi (2000)
s1995KOBEJA01HORI	7.01	SS		52.0	15.2	1.30	Horikawa et al. (1996)
s1995KOBEJA01IDEx	6.89	SS		44.0	19.0	0.82	Ide et al. (1996)
s1995KOBEJA01KOKE	6.87	SS		60.0	16.0	0.91	Koketsu et al. (1998)
s1995KOBEJA01WALD	6.92	SS		60.0	20.0	0.73	Wald (1996)
s1995KOBEJA01YOSH	6.86	SS		56.0	16.0	0.84	Yoshida et al. (1996)

evTAG	M_W	FT	S	*L* (km)	*W* (km)	*D* (m)	Reference
s1995KOBEJA01ZENG	6.90	SS		53.5	19.5	0.76	Zeng and Anderson (2000)
s1995KOBEJA02SEKI	7.02	SS		63.6	20.5	0.79	Sekiguchi et al. (2002)
s1996NAZCAR01SALI	7.84	RS	*	140.0	80.0	0.95	Salichon et al. (2003)
s1996NAZCAR01SPEN	8.06	RS	*	216.0	108.0	1.18	Spence et al. (1999)
s1997KAGOSH01HORI	6.10	SS		14.0	10.0	0.36	Horikawa (2001)
s1997KAGOSH01MIYA	6.04	SS		16.0	12.0	0.20	Miyakoshi et al. (2000)
s1997YAMAGU01IDEx	5.81	SS		9.0	11.0	0.21	Ide (1999)
s1997YAMAGU01MIYA	5.82	SS		14.0	14.0	0.09	Miyakoshi et al. (2000)
s1998IWATEJ01MIYA	6.27	RS		12.0	12.0	0.12	Miyakoshi et al. (2000)
s1998IWATEJ01NAKA	6.30	RS		10.0	8.0	0.49	Nakahara et al. (2002)
s1999CHICHI01CHIx	7.68	RS		98.0	35.0	4.08	Chi et al. (2001)
s1999CHICHI01JOHN	7.58	RS		90.1	30.0	3.86	Johnson et al. (2001)
s1999CHICHI01SEKI	7.63	RS		78.0	39.0	3.75	Sekiguchi (2002)
s1999CHICHI01WUxx	7.67	RS		62.0	35.0	5.88	Wu et al. (2001)
s1999CHICHI01ZENG	7.61	RS		84.0	42.0	3.02	Zeng and Chen (2001)
s1999CHICHI02MAxx	7.69	RS		80.0	40.0	4.74	Ma et al. (2001)
s1999DUZCET01BIRG	7.10	SS		34.7	12.6	1.10	Birgoren et al. (2004)
s1999DUZCET01DELO	7.18	SS		40.0	25.0	2.02	Delouis et al. (2004)
s1999HECTOR01JIxx	7.17	SS		72.0	16.2	1.87	Ji et al. (2002)
s1999HECTOR01JONS	7.16	SS		73.5	21.0	1.52	Jonsson et al. (2002)
s1999HECTOR01KAVE	7.24	SS		98.0	24.0	0.97	Kaverina et al. (2002)
s1999HECTOR01SALI	7.14	SS		69.0	18.0	1.61	Salichon et al. (2004)
s1999IZMITT01BOUC	7.59	SS		141.0	18.0	3.13	Bouchon et al. (2002)
s1999IZMITT01CAKI	7.47	SS		140.0	24.0	1.74	Cakir et al. (2003)
s1999IZMITT01DELO	7.56	SS		165.0	22.5	1.91	Delouis et al. (2002)
s1999IZMITT01REIL	7.42	SS		145.6	18.2	1.90	Reilinger et al. (2000)
s1999IZMITT01SEKI	7.44	SS		126.0	23.3	1.63	Sekiguchi and Iwata (2002)
s1999IZMITT01YAGI	7.40	SS		81.9	21.6	2.57	Yagi and Kikuchi (2000)
s2000TOTTOR01IWAT	6.86	SS		33.0	21.0	0.85	Iwata et al. (2000)
s2000TOTTOR01PIAT	6.60	SS		38.0	18.0	1.33	Piatanesi et al. (2007)
s2000TOTTOR01SEKI	6.83	SS		34.0	17.6	0.57	Sekiguchi (2003)
s2000TOTTOR01SEMM	6.73	SS		32.0	20.0	0.62	Semmane et al. (2005a)
s2001GEIYOJ01KAKE	6.68	NS		30.0	18.0	0.67	Kakehi (2004)
s2001GEIYOJ01SEKI	6.79	NS		30.0	21.0	0.83	Sekiguchi and Iwata (2001)
s2002DENALI01ASAN	7.87	SS		288.0	18.0	4.32	Asano et al. (2005)
s2002DENALI01OGLE	7.91	SS		330.0	30.0	2.32	Oglesby et al. (2004)
s2003MIYAGI01HIKI	6.10	RS		18.0	10.0	0.31	Hikima and Koketsu (2004)
s2003MIYAGI01MIUR	6.08	RS		9.6	9.6	0.59	Miura et al. (2004)
s2003TOKACH01KOKE	8.21	RS	*	120.0	100.0	3.11	Koketsu et al. (2004)
s2003TOKACH01TANI	7.96	RS	*	120.0	120.0	1.06	Tanioka et al. (2004)
s2003TOKACH01YAGI	8.16	RS	*	120.0	170.0	1.58	Yagi (2004)
s2003TOKACH01YAMA	8.03	RS	*	120.0	80.0	1.92	Yamanaka and Kikuchi (2003)

evTAG	M_W	FT	S	*L* (km)	*W* (km)	*D* (m)	Reference
s2004PARKFI01CUST	6.06	SS		36.1	11.9	0.10	Custodio et al. (2005)
s2004PARKFI01DREG	6.00	SS		24.6	12.1	0.15	Dreger et al. (2005)
s2004PARKFI01JIxx	5.90	SS		34.0	13.1	0.08	CALTECH
s2004SUMATR01AMMO	9.10	RS	*	1420.0	224.0	3.55	Ammon et al. (2005)
s2004SUMATR01JIxx	8.89	RS	*	450.0	180.0	6.77	UCSB
s2004SUMATR02RHIE	9.19	RS	*	970.5	199.6	11.43	Rhie et al. (2007)
s2005KASHMI01KONC	7.60	RS		76.0	35.0	2.94	CALTECH
s2005KASHMI01SHAO	7.60	RS		108.0	45.0	2.45	UCSB
s2005SUMATR01JIxx	8.70	RS	*	380.0	192.0	3.50	CALTECH
s2005SUMATR01KONC	8.50	RS	*	304.0	192.0	2.72	Konca et al. (2007)
s2005SUMATR01SHAO	8.68	RS	*	340.0	220.0	3.38	UCSB
s2006JAVAIN01YAGI	7.82	RS	*	220.0	140.0	0.75	Yagi and Fukahata (2011a)
s2006SOUTHE01JIxx	7.70	RS	*	315.0	77.0	0.46	UCSB
s2006SOUTHE01KONC	7.90	RS	*	240.0	162.5	1.53	CALTECH
s2006KURILI01JIxx	8.30	RS	*	280.0	125.0	2.66	UCSB
s2006KURILI01LAYx	8.40	RS	*	240.0	100.0	4.58	Lay et al. (2009)
s2006KURILI01SLAD	8.30	RS	*	315.0	132.0	1.74	CALTECH
s2007BENKUL01JIxx	8.40	RS	*	460.0	159.5	1.10	UCSB
s2007BENKUL02GUSM	8.50	RS	*	300.0	225.0	1.72	Gusman et al. (2010)
s2007BENKUL02KONC	8.40	RS	*	256.0	192.0	1.68	Konca et al. (2008)
s2007KURILI01JIxx	8.10	NS		192.0	35.0	7.31	UCSB
s2007KURILI01SLAD	8.10	NS		216.0	35.0	4.22	CALTECH
s2007PAGAII01JIxx	7.90	RS	*	225.0	90.0	0.76	USGS
s2007PAGAII01KONC	7.90	RS	*	192.0	110.0	0.80	Konca et al. (2008)
s2007PAGAII01SLAD	7.90	RS	*	168.0	100.0	0.99	CALTECH
s2007PISCOP01JIxx	8.00	RS	*	156.0	108.0	2.01	USGS
s2007PISCOP01KONC	8.00	RS	*	168.0	160.0	0.75	CALTECH
s2007PISCOP01SLAD	8.00	RS	*	120.0	120.0	1.63	Sladen et al.(2010)
s2007TOCOPI01JIxx	7.81	RS	*	195.0	120.0	0.70	UCSB
s2007TOCOPI01MOTA	7.80	RS	*	233.3	102.9	0.70	Motagh et al. (2010)
s2007TOCOPI01SLAD	7.70	RS	*	162.0	99.0	1.12	CALTECH
s2007TOCOPI01ZENG	7.70	RS	*	180.0	130.0	0.66	USGS
s2007TOCOPI03BEJA	7.70	RS	*	210.0	98.0	0.51	Bejar-Pizzaro et al. (2010)
s2008HONSHU01HAYE	6.80	RS		36.0	22.0	0.98	USGS
s2008IWATEx01ASAN	6.89	RS		34.0	18.0	1.35	Asano and Iwata (2011b)
s2008IWATEx01CULT	7.00	RS		42.7	17.4	1.82	Cultrera et al. (2013)
s2008IWATEx01HAYE	6.80	RS		36.0	22.0	0.98	USGS
s2008SIMEUL01HAYE	7.40	RS	*	90.0	130.0	0.22	USGS
s2008SIMEUL01SLAD	7.40	RS	*	112.0	80.0	0.29	CALTECH
s2008WENCHU01JIxx	7.90	OS		315.0	40.0	2.79	USGS
s2008WENCHU01SLAD	7.90	OS		220.0	28.0	4.45	CALTECH
s2008WENCHU01YAGI	8.03	OS		310.0	60.0	3.32	Yagi et al. (2012)

evTAG	M_W	FT	S	*L* (km)	*W* (km)	*D* (m)	Reference
s2008WENCHU03FIEL	7.92	OS		270.0	28.0	3.62	Fielding et al. (2013)
s2009LAQUIL01GUAL	6.30	NS		26.0	20.0	0.24	Gualandi et al. (2013)
s2009LAQUIL01POIA	6.30	NS		24.0	16.0	0.27	Poiata et al. (2012b)
s2009LAQUIL02CIRE	6.10	NS		21.0	15.8	0.44	Cirella et al. (2012)
s2009VANUAT01HAYE	7.80	RS	*	130.0	120.0	0.44	USGS
s2009VANUAT01SLAD	7.60	RS	*	91.0	55.0	0.95	CALTECH
s2010DARFIE01ATZO	7.10	SS		68.0	12.0	2.77	Atzori et al. (2012)
s2010DARFIE01HAYE	7.02	SS		75.0	24.0	0.70	USGS
s2010HAITIx01CALA	7.10	SS		38.0	24.0	1.84	Calais et al. (2010)
s2010HAITIx01HAYE	7.00	SS		99.0	22.5	0.68	Hayes et al. (2010)
s2010HAITIx01SLAD	7.00	SS		42.0	20.0	1.75	CALTECH
s2010MAULEC01DELO	8.80	RS	*	560.0	200.0	3.50	Delouis at al. (2010)
s2010MAULEC01HAYE	8.77	RS	*	450.0	200.0	4.64	USGS
s2010MAULEC01LUTT	8.80	RS	*	520.0	177.3	5.08	Luttrell et al. (2011)
s2010MAULEC01POLL	8.80	RS	*	510.7	132.9	6.89	Pollitz et al. (2011)
s2010MAULEC01SHAO	8.90	RS	*	450.0	187.0	5.41	USGS
s2010MAULEC01SLAD	8.76	RS	*	540.0	180.0	2.42	CALTECH
s2010MAULEC02LORI	8.80	RS	*	550.0	175.0	5.21	Lorito et al. (2011)
s2011PAKIST01HAYE	7.20	NS		35.0	40.0	0.84	USGS
s2011PAKIST02HAYE	7.20	NS		40.0	40.0	0.74	USGS
s2011TOHOKU01AMMO	9.00	RS	*	330.0	180.0	17.69	Ammon et al.(2011)
s2011TOHOKU01HAYE	9.05	RS	*	375.0	260.0	9.40	Hayes (2011)
s2011TOHOKU01IDEx	9.00	RS	*	420.0	225.4	11.31	Ide et al. (2011)
s2011TOHOKU01LAYx	9.00	RS	*	320.0	200.0	18.87	Lay et al. (2011)
s2011TOHOKU01YAGI	9.11	RS	*	380.0	200.0	16.56	Yagi and Fukahata (2011b)
s2011TOHOKU01YAMA	9.00	RS	*	280.0	180.0	19.20	Yamazaki et al. 2011
s2011TOHOKU01YUEx	9.00	RS	*	300.0	210.0	22.60	Yue and Lay (2013)
s2011TOHOKU02FUJI	9.00	RS	*	350.0	200.0	10.72	Fujii et al. (2011)
s2011TOHOKU02GUSM	9.00	RS	*	350.0	200.0	13.28	Gusman et al. (2012)
s2011TOHOKU03SATA	9.00	RS	*	450.0	200.0	11.60	Satake et al. (2013)
s2011TOHOKU03WEIx	9.09	RS	*	450.0	200.0	14.49	Wei et al. (2012)
s2011TOHOKU04SHAO	9.10	RS	*	325.0	180.0	20.37	Shao et al. (2011)
s2011VANTUR01ALTI	7.20	RS		53.3	41.2	0.78	Altiner et al. (2013)
s2011VANTUR01ELLI	7.10	RS		31.0	21.6	2.70	Elliott et al. (2013)
s2011VANTUR01HAYE	7.10	RS		55.0	41.2	0.75	USGS
s2011VANTUR01KONC	7.10	RS		55.0	27.5	1.26	Konca (2015)
s2011VANTUR01SHAO	7.13	RS		40.0	45.0	1.02	UCSB
s2011VANTUR01UTKU	7.10	RS		42.0	28.0	1.17	Utkucu 2013
s2012COSTAR01HAYE	7.57	RS	*	110.0	88.0	0.54	USGS
s2012COSTAR01LIUx	7.60	RS	*	120.0	84.0	0.80	Liu et al. (2015)
s2012COSTAR01YUEx	7.60	RS	*	97.5	105.0	0.92	Yue et al. (2013)
s2012MASSET01LAYx	7.82	RS	*	144.0	54.0	2.88	Lay et al. (2013a)

evTAG	M_W	FT	S	*L* (km)	*W* (km)	*D* (m)	Reference
s2012MASSET01SHAO	7.72	RS	*	120.0	50.0	2.26	UCSB
s2012MASSET01WEIx	7.83	RS	*	190.0	90.0	0.66	CALTECH
s2012OAXACA01HAYE	7.40	RS	*	72.0	66.0	0.79	USGS
s2012OAXACA01WEIx	7.40	RS	*	45.0	45.0	1.52	CALTECH
s2012SUMATR01YUEx	8.70	SS		580.0	50.0	8.09	Yue et al. (2012)
s2013OKHOTS01WEIx	8.39	NS		262.5	112.5	1.45	Wei et al. (2013b)
s2013OKHOTS01YExx	8.30	NS		180.0	60.0	4.14	Ye at al. (2013)
s2015GORKHA01HAYE	7.86	RS	*	200.0	150.0	0.79	USGS
s2015GORKHA01YAGI	7.90	RS	*	136.0	88.0	2.91	Yagi and Okuwaki (2015)
s1948FUKUIJ01ICHI	6.65	SS		54.0	18.0	0.33	Ichinose et al. (2005)
s1968HYUGAx01YAGI	7.53	RS	*	72.0	63.0	1.32	Yagi et al. (1998)
s1968TOKACH01NAGA	8.35	RS	*	240.0	120.0	2.41	Nagai et al. (2001)
s1969GIFUxK01TAKE	6.43	SS		20.0	11.2	0.68	Takeo (1990)
s1971SANFER01HEAT	6.82	RS		27.8	13.3	1.46	Heaton (1982)
s1974PERUCE01HART	8.01	RS	*	250.0	140.0	1.02	Hartzell and Langer (1993)
s1978MIYAGI01YAMA	7.61	RS	*	80.0	70.0	0.78	Yamanaka and Kikuchi (2004)
s1978TABASI01HART	7.09	OS		95.0	45.0	0.34	Hartzell and Mendoza (1991)
s1979COYOTE01LIUx	5.92	SS		6.0	6.5	0.67	Liu and Helmberger (1983)
s1979PETATL01MEND	7.39	RS	*	100.0	100.0	0.42	Mendoza (1995)
s1980IZUxHA01TAKE	6.61	SS		20.0	12.0	1.06	Takeo (1988)
s1981PLAYAA01MEND	7.25	RS	*	45.0	55.0	0.83	Mendoza (1993)
s1983BORAHP01MEND	6.82	NS		42.3	26.6	0.44	Mendoza and Hartzell (1988)
s1985CENTRA01MEND	8.16	RS	*	255.0	150.0	0.87	Mendoza et al. (1994)
s1985MICHOA01MEND	8.01	RS	*	180.0	139.0	1.39	Mendoza and Hartzell (1989)
s1985ZIHUAT01MEND	7.42	RS	*	67.5	67.5	0.76	Mendoza (1993)
s1987ELMORE01LARS	6.52	SS		22.5	10.0	0.97	Larsen et al. (1992)
s1987WHITTI01HART	5.89	RS		10.0	10.0	0.26	Hartzell and Iida (1990)
s1991SIERRA01WALD	5.59	RS		4.9	4.8	0.31	Wald (1992)
s1993PUMQUx01WANG	6.29	NS		26.0	19.0	0.19	Wang et al. (2014)
s1995COLIMA01MEND	7.96	RS	*	170.0	100.0	1.39	Mendoza and Hartzell (1999)
s1995COPALA01COUR	7.30	RS	*	70.0	55.0	0.52	Courboulex et al. (1997)
s1996HYUGAx01YAGI	6.81	RS	*	32.1	32.1	0.54	Yagi et al. (1999)
s1996HYUGAx02YAGI	6.68	RS	*	29.2	29.2	0.42	Yagi et al. (1999)
s1996PUMQUx01WANG	6.08	NS		22.0	17.0	0.12	Wang et al. (2014)
s1997COLFIO03HERN	5.86	NS		9.0	6.0	0.45	Hernandez et al. (2004)
s1997KAGOSH02HORI	6.01	SS		17.0	10.0	0.21	Horikawa (2001)
s1997ZIRKUH01SUDH	7.20	SS		149.4	18.0	1.14	Sudhaus and Jonsson (2011)
s1998ANTARC01ANTO	7.98	SS		200.0	35.0	4.55	Antolik et al. (2000)
s1998ANTARC02ANTO	7.76	NS		75.0	45.0	4.52	Antolik et al. (2000)
s1998PUMQUx01WANG	6.16	NS		36.0	21.0	0.08	Wang et al. (2014)
s1999OAXACA01HERN	7.47	NS		82.5	45.0	0.70	Hernandez et al. (2001)
s2000KLEIFA01SUDH	5.87	SS		9.0	8.0	0.31	Sudhaus and Jonsson (2009)

evTAG	M_W	FT	S	*L* (km)	*W* (km)	*D* (m)	Reference
s2003BAMIRA01POIA	6.50	SS		25.0	20.0	0.48	Poiata et al. (2012a)
s2003BOUMER01SEMM	7.10	RS		64.0	32.0	1.24	Semmane et al. (2005b)
s2003CARLSB01WEIx	7.60	SS		290.0	36.0	0.61	CALTECH
s2003COLIMA01YAGI	7.50	RS	*	70.0	85.0	0.61	Yagi et al. (2004)
s2004IRIANx01WEIx	7.20	SS		92.0	28.0	1.12	CALTECH
s2004NIIGAT01ASAN	6.62	RS		28.0	18.0	0.67	Asano and Iwata (2009)
s2004ZHONGB01ELLI	6.20	NS		17.0	19.6	0.21	Elliott et al. (2010)
s2005FUKUOK01ASAN	6.60	SS		26.0	18.0	0.68	Asano and Iwata (2006)
s2005NORTHE01SHAO	7.20	SS		90.0	30.0	0.89	UCSB
s2005ZHONGB01ELLI	6.20	NS		23.0	14.0	0.30	Elliott et al. (2010)
s2007NIIGAT01CIRE	6.60	RS		29.8	21.0	0.50	Cirella et al. (2008)
s2007NOTOHA01ASAN	6.73	RS		28.0	16.0	1.16	Asano and Iwata (2011a)
s2007SOLOMO01JIxx	8.10	RS	*	285.0	80.0	1.55	UCSB
s2008GERZET01ELLI	6.40	NS		14.0	17.0	0.61	Elliott et al. (2010)
s2008GERZET02ELLI	5.90	NS		12.0	8.8	0.29	Elliott et al. (2010)
s2008KERMED01HAYE	7.00	RS	*	45.0	45.0	0.33	USGS
s2008SULAWE01SLAD	7.30	RS	*	104.0	40.0	0.73	CALTECH
s2008YUTIAN01ELLI	7.10	NS		46.6	16.5	2.26	Elliott et al. (2010)
s2008ZHONGB01ELLI	6.70	NS		54.0	24.9	0.31	Elliott et al. (2010)
s2009FIORDL01HAYE	7.60	RS	*	88.0	72.0	1.53	USGS
s2009GULFOF01HAYE	6.90	SS		60.0	18.2	0.64	USGS
s2009OFFSHO01HAYE	7.30	SS		180.0	31.5	0.66	USGS
s2009PAPUAx01HAYE	7.60	RS	*	96.0	78.0	0.91	USGS
s2009SAMOAx01HAYE	8.00	NS		130.0	45.0	5.02	USGS
s2010BONINI01HAYE	7.40	NS		75.0	35.0	0.93	USGS
s2010ELMAYO01WEIx	7.29	SS		156.0	21.0	1.13	Wei et al. (2011)
s2010NORTHE01HAYE	7.80	RS	*	108.0	108.0	0.99	USGS
s2010NORTHE02HAYE	7.20	RS	*	72.0	54.0	0.37	USGS
s2010SUMATR01HAYE	7.70	RS	*	195.0	140.0	0.33	USGS
s2010VANUAT01HAYE	7.30	NS		50.0	38.5	0.86	USGS
s2011KERMAD01HAYE	7.30	NS		104.0	54.0	0.95	USGS
s2011OFFSHO01HAYE	7.30	RS	*	99.0	72.0	0.41	USGS
s2011VANUAT01HAYE	7.30	RS	*	72.0	66.0	0.23	USGS
s2012BRAWLE01WEIx	5.45	SS		11.3	9.8	0.10	Wei et al. (2013a)
s2012BRAWLE02WEIx	5.38	SS		11.3	9.8	0.07	Wei et al. (2013a)
s2012OFFSHO01HAYE	7.30	RS	*	110.0	80.0	0.28	USGS
s2012SUMATR03HAYE	7.20	SS		72.0	17.5	1.93	USGS
s2013BALOCH01AVOU	7.70	SS		232.0	32.0	2.82	Avouac et al. (2014)
s2013KHASHI01WEIx	7.80	NS		100.0	45.0	1.57	CALTECH
s2013SANTAC01LAYx	8.06	RS	*	144.0	90.0	2.86	Lay et al. (2013b)
s2013SCOTIA01HAYE	7.70	SS		322.0	50.0	1.01	USGS
s2014IQUIQU01WEIx	8.10	RS	*	240.0	160.0	0.79	CALTECH

- Each rupture model is associated with unique identifier *evTAG*, which can be used to access the model online on the SRCMOD database (for details, see Mai and Thingbaijam, 2014). USGS, CALTECH and UCSB refer to the online models from the respective organizations/institutes, namely United States Geological Survey, California Institute of Technology, and University of California Santa Barbara. M_W corresponds to moment magnitude of each event. FT stands for faulting type, which can be RS (reverse), NS (normal), SS (strike-slip), or OS (oblique-slip). The subduction-interface events are indicated with '*' listed under the heading denoted by S. The notations - *L*, *W* and *D* stand for rupture length, rupture width, and average slip.

Table S2. Comparison of source-scaling relationships for shallow crustal reverse-faulting events obtained by various studies

Equation	*b (sb)*	*a (sa)*	*s*	Authors
$\log_{10} L = a + b M_W$	**0.614 (0.043)**	**-2.693 (0.292)**	**0.083**	**This study**
	0.60	-2.77	--	MB2000
	0.58 (0.03)	-2.42 (0.21)	0.16	WC1994
	0.57 (0.02)	-2.37 (0.13)	0.18	BEA2010
	0.60	-2.54	--	LEO2010
$\log_{10} W = a + b M_W$	**0.435 (0.050)**	**-1.669 (0.336)**	**0.087**	**This study**
	0.53	-2.34	--	MB2000
	0.41 (0.03)	-1.61 (0.20)	0.15	WC1994
	0.46 (0.02)	-1.86 (0.12)	0.17	BEA2010
	0.40	-1.46	--	LEO2010
$\log_{10} A = a + b M_W$	**1.049 (0.066)**	**-4.362 (0.445)**	**0.121**	**This study**
	1.13	-5.11	--	MB2000
	0.98 (0.06)	-3.99 (0.36)	0.26	WC1994
	1.03 (0.03)	-4.23 (0.18)	0.25	BEA2010
	1.0	-4.0	--	LEO2010

- The slope and intercept are denoted by symbols *a* and *b*, their standard errors by *sa* and *sb*, while standard deviation is denoted by *s*. The authors are: MB2000 (Mai and Beroza, 2000), WC1994 (Wells and Coppersmith, 1994), BEA2010 (Blaser *et al*., 2010), and LEO2010 (Leonard, 2010). The M_W-$\log_{10} A$ relationships for BEA2010 are obtained from the scaling relationships of *W* and *L*.

Table S3. Same as Table S2, but for subduction-interface events obtained by various studies

Equation	*b (sb)*	*a (sa)*	*s*	Authors
$\log_{10} L = a + b M_W$	**0.583 (0.037)**	**-2.412 (0.288)**	**0.107**	**This study**
	0.57 (0.02)	-2.37 (0.13)	0.18	BEA2010
	0.60	-2.54	--	LEO2010
	0.56 (0.03)	-2.48 (0.22)	0.18	SAB2010
	0.47	-1.50	0.17	GEA2016
$\log_{10} W = a + b M_W$	**0.366 (0.031)**	**-0.880 (0.243)**	**0.099**	**This study**
	0.46 (0.02)	-1.86 (0.12)	0.17	BEA2010
	0.40	-1.46	--	LEO2010
	0.35 (0.03)	-0.88 (0.23)	0.17	SAB2010
	0.30	-0.36	--	SST2016
	0.31	-0.49	0.15	GEA2016
$\log_{10} A = a + b M_W$	**0.949 (0.049)**	**-3.292 (0.377)**	**0.150**	**This study**
	1.03 (0.03)	-4.23 (0.18)	0.25	BEA2010
	1.0	-4.0	--	LEO2010
	0.95 (0.05)	-3.48 (0.40)	0.30	SAB2010
	1.0	-3.72	--	SST2016
	0.78	-1.99	0.24	GEA2016

- The authors are: BEA2010 (Blaser *et al*., 2010), LEO2010 (Leonard, 2010), SAB2010 (Strasser *et al*., 2010), and GEA2016 (Goda *et al*., 2016). BEA2010 and LEO2010 did not discriminate subduction interface events from shallow crustal reverse-slip events. The relationships for tsunamigenic events given by GEA2016 are considered here.

Table S4. Same as Table S3, but for normal-faulting events obtained by various studies

Equation	*b (sb)*	*a (sa)*	*s*	Authors
$\log_{10} L = a + b M_W$	**0.485 (0.036)**	**-1.722 (0.260)**	**0.128**	**This study**
	0.50 (0.06)	-1.88 (0.37)	0.17	WC1994
	0.52 (0.04)	-1.91 (0.29)	0.18	BEA2010
$\log_{10} W = a + b M_W$	**0.323 (0.047)**	**-0.829 (0.333)**	**0.127**	**This study**
	0.35 (0.05)	-1.14 (0.28)	0.12	WC1994
	0.36 (0.04)	-1.20 (0.25)	0.16	BEA2010
$\log_{10} A = a + b M_W$	**0.808 (0.059)**	**-2.551 (0.423)**	**0.181**	**This study**
	0.82 (0.08)	-2.87 (0.50)	0.22	WC1994
	0.88 (0.06)	-3.11 (0.38)	0.24	BEA2010

- The authors are: WC1994 (Wells and Coppersmith, 1994), and BEA2010 (Blaser *et al*., 2010).

Table S5. Same as Table S2, but for strike-slip events obtained by various studies

Equation	*b (sb)*	*a (sa)*	*s*	Authors
$\log_{10} L = a + b M_W$	**0.681 (0.052)**	**-2.943 (0.357)**	**0.151**	**This study**
	0.60	-2.69	--	MB2000
	0.62 (0.02)	-2.57 (0.12)	0.16	WC1994
	0.64 (0.02)	-2.69 (0.11)	0.18	BEA2010
	0.60, $L \leq 45$ km 1.00, $L > 45$ km	-2.50, $L \leq 45$ km	--	LEO2010
$\log_{10} W = a + b M_W$	**0.261 (0.026)**	**-0.543 (0.179)**	**0.105**	**This study**
	0.26	-0.64	--	MB2000
	0.27 (0.02)	-0.76 (0.12)	0.14	WC1994
	0.33 (0.03)	-1.12 (0.12)	0.15	BEA2010
	0.40, $L \leq 45$ km 0.00, $L > 45$ km	-1.49, $L \leq 45$ km 1.23, $L > 45$ km	--	LEO2010
$\log_{10} A = a + b M_W$	**0.942 (0.058)**	**-3.486 (0.399)**	**0.184**	**This study**
	0.86	-3.33	--	MB2000
	0.90 (0.03)	-3.42 (0.18)	0.22	WC1994
	0.97 (0.04)	-3.81 (0.16)	0.23	BEA2010
	1.0	-3.99	--	LEO2010
	1.00, A≤537 km^2 0.75, A>537 km^2	-3.98, A≤537 km^2 -2.30, A>537 km^2	--	HB2002

- The authors are: MB2000 (Mai and Beroza, 2000), WC1994 (Wells and Coppersmith, 1994), BEA2010 (Blaser *et al.*, 2010), LEO2010 (Leonard, 2010), and HB2002 (Hanks and Bakun, 2002.

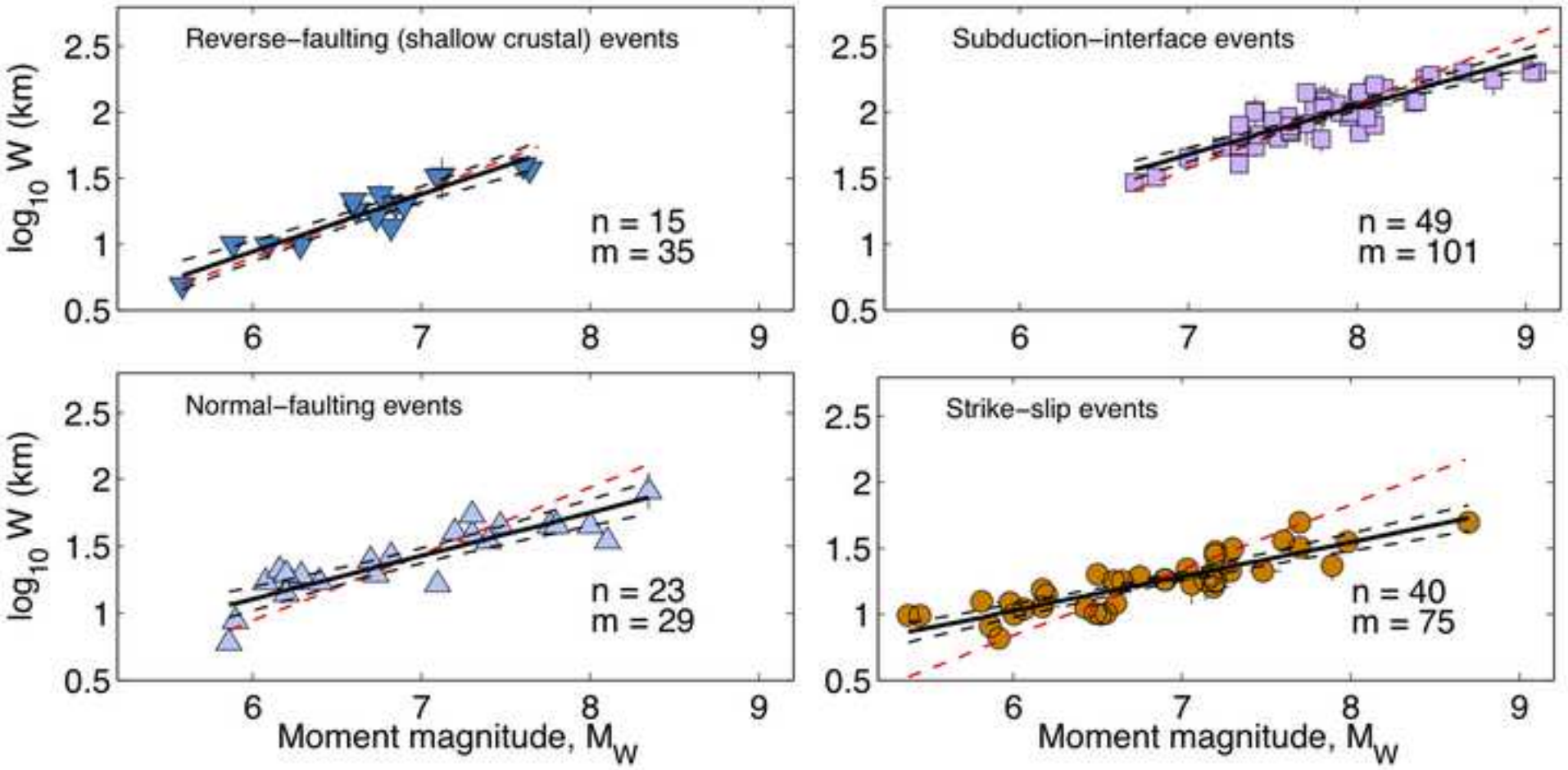

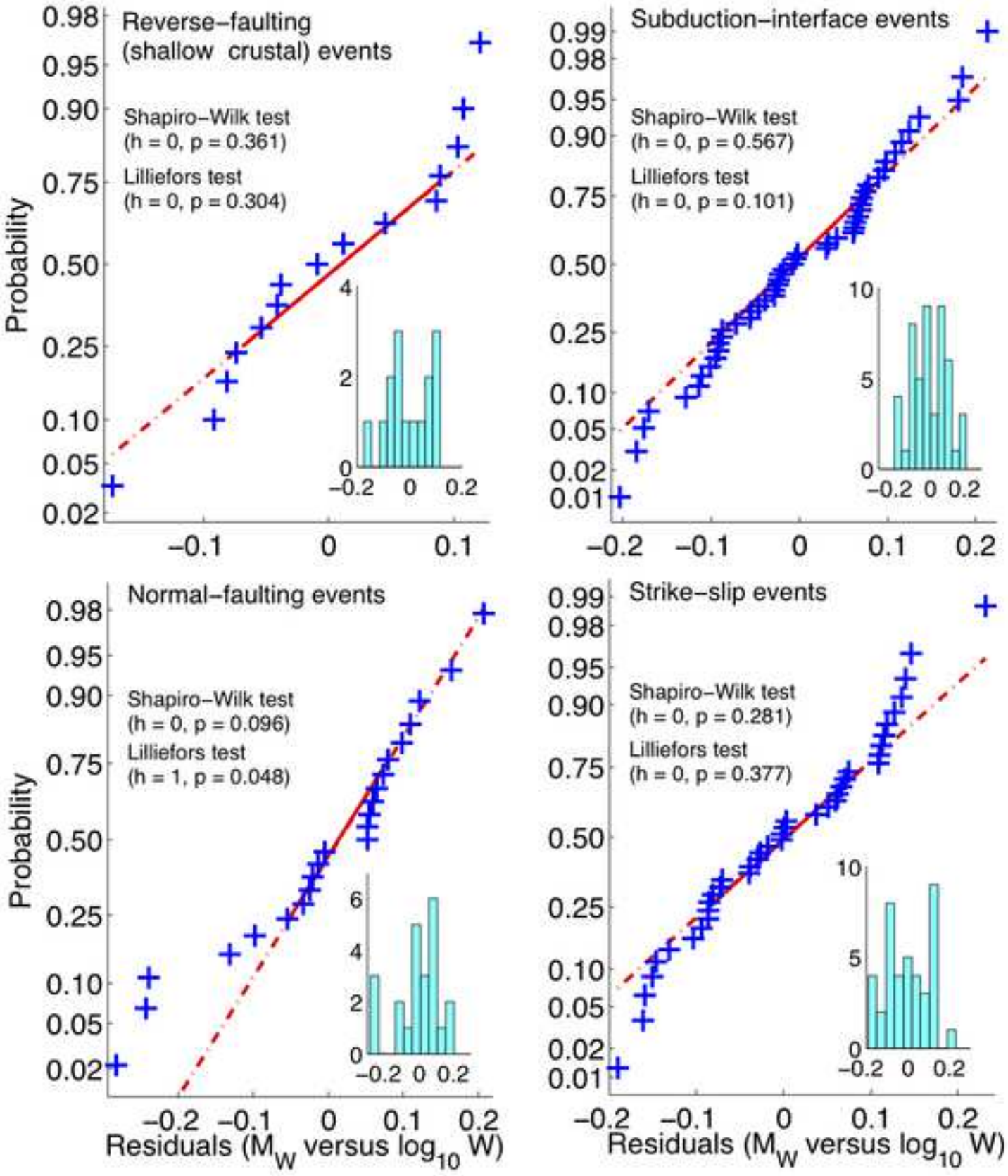

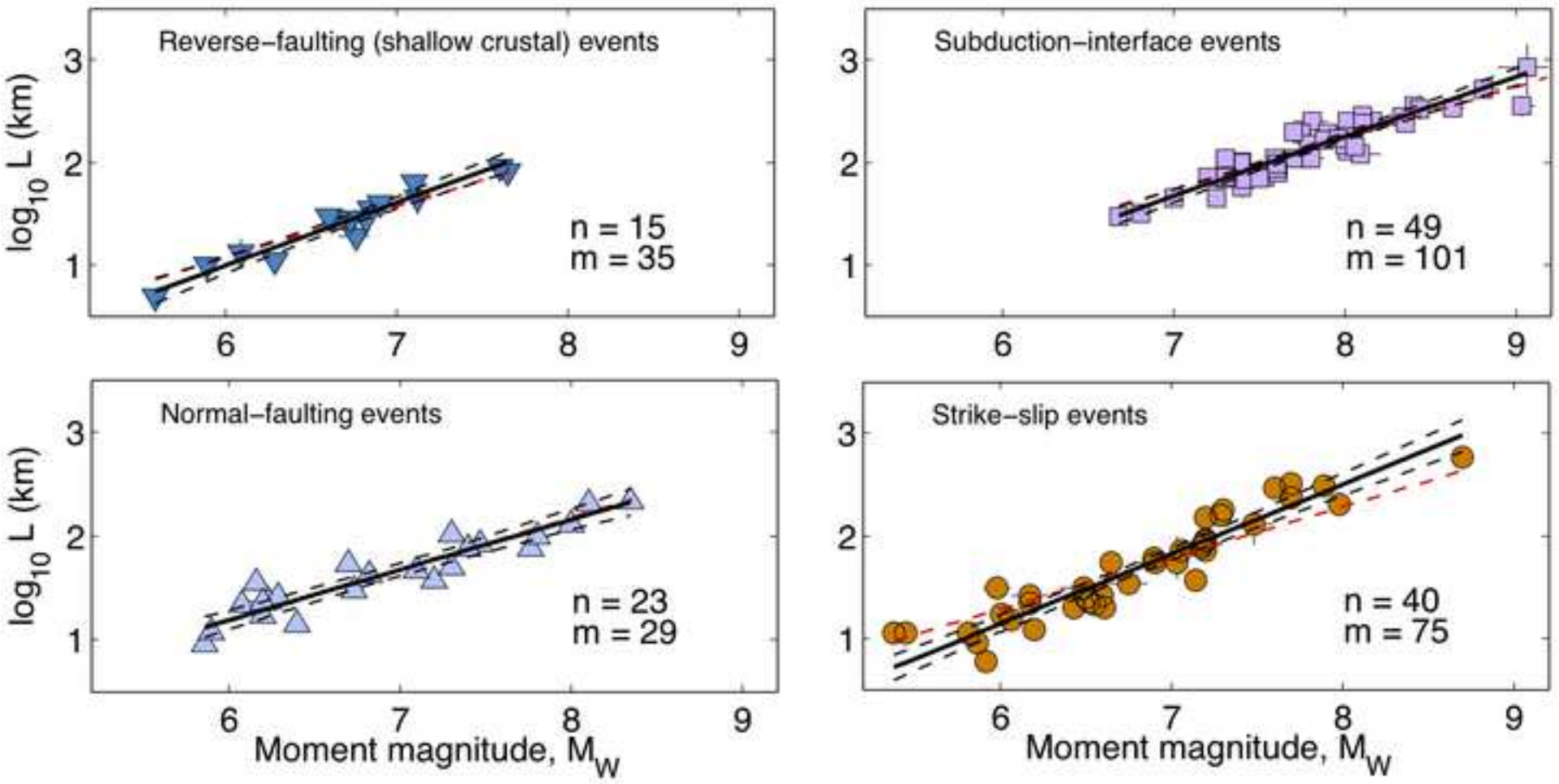

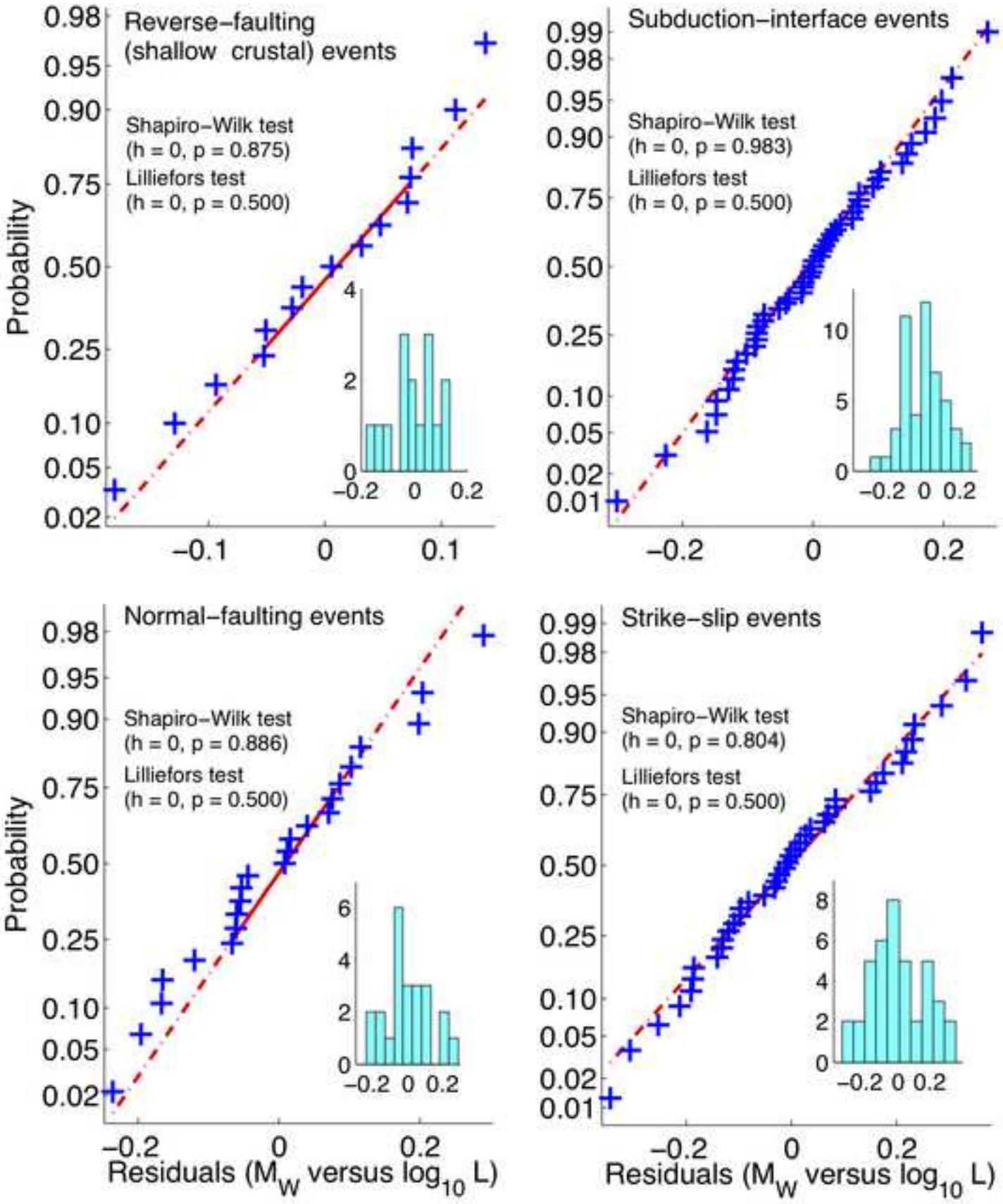

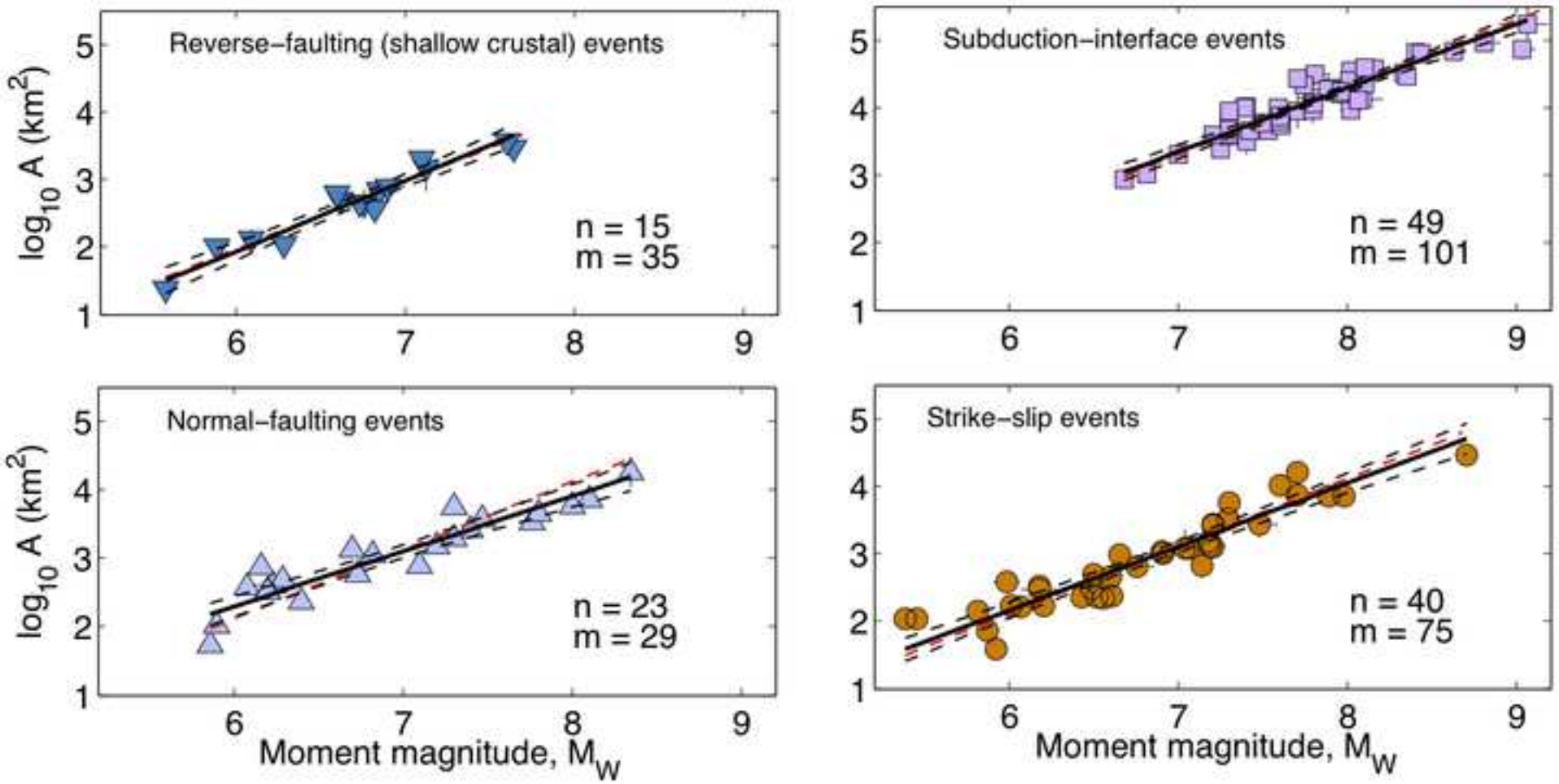

Click here to download Supplemental Material (Main Page, Tables, Figures) neoBSSA-EQS-FigureS6.png

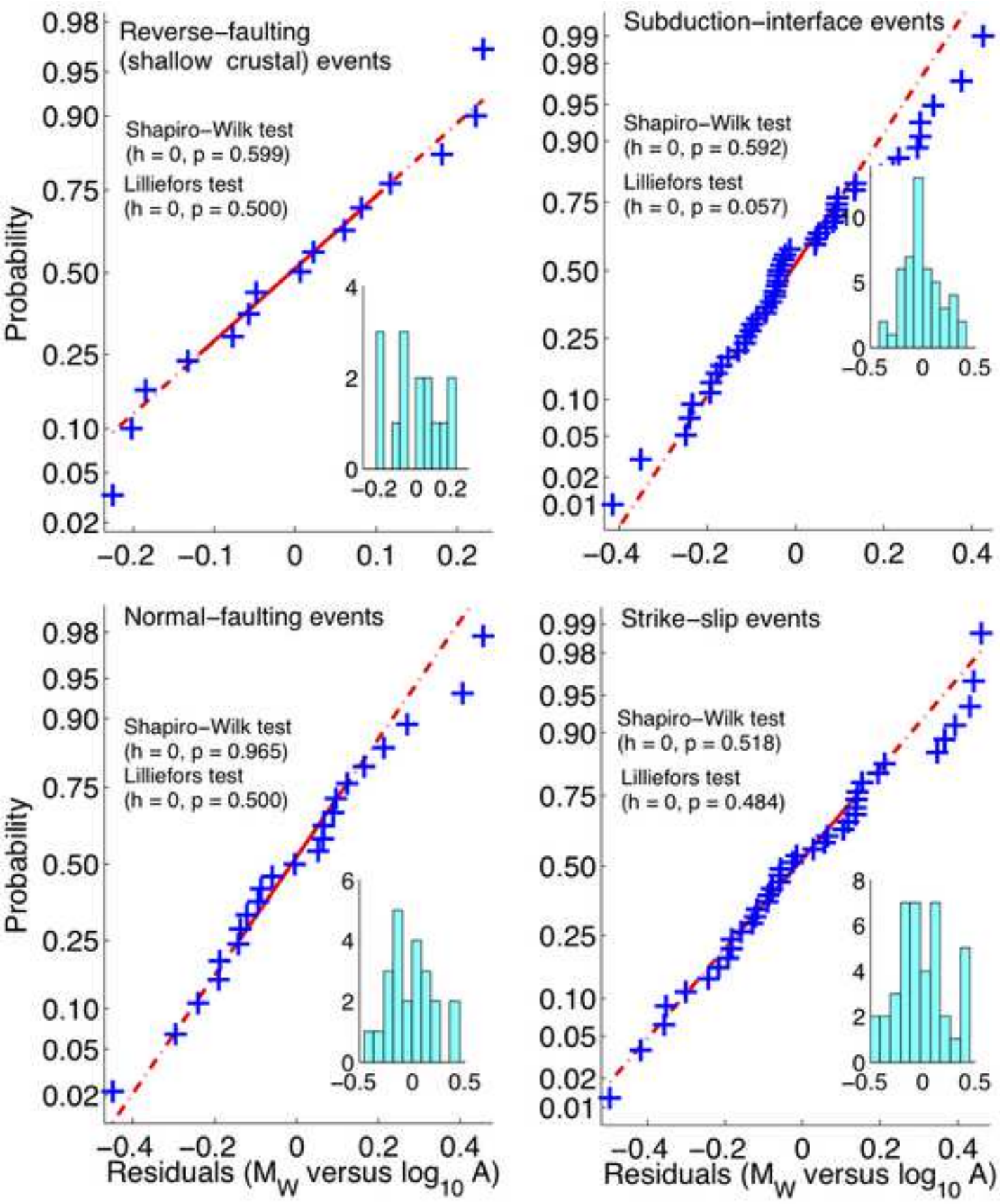

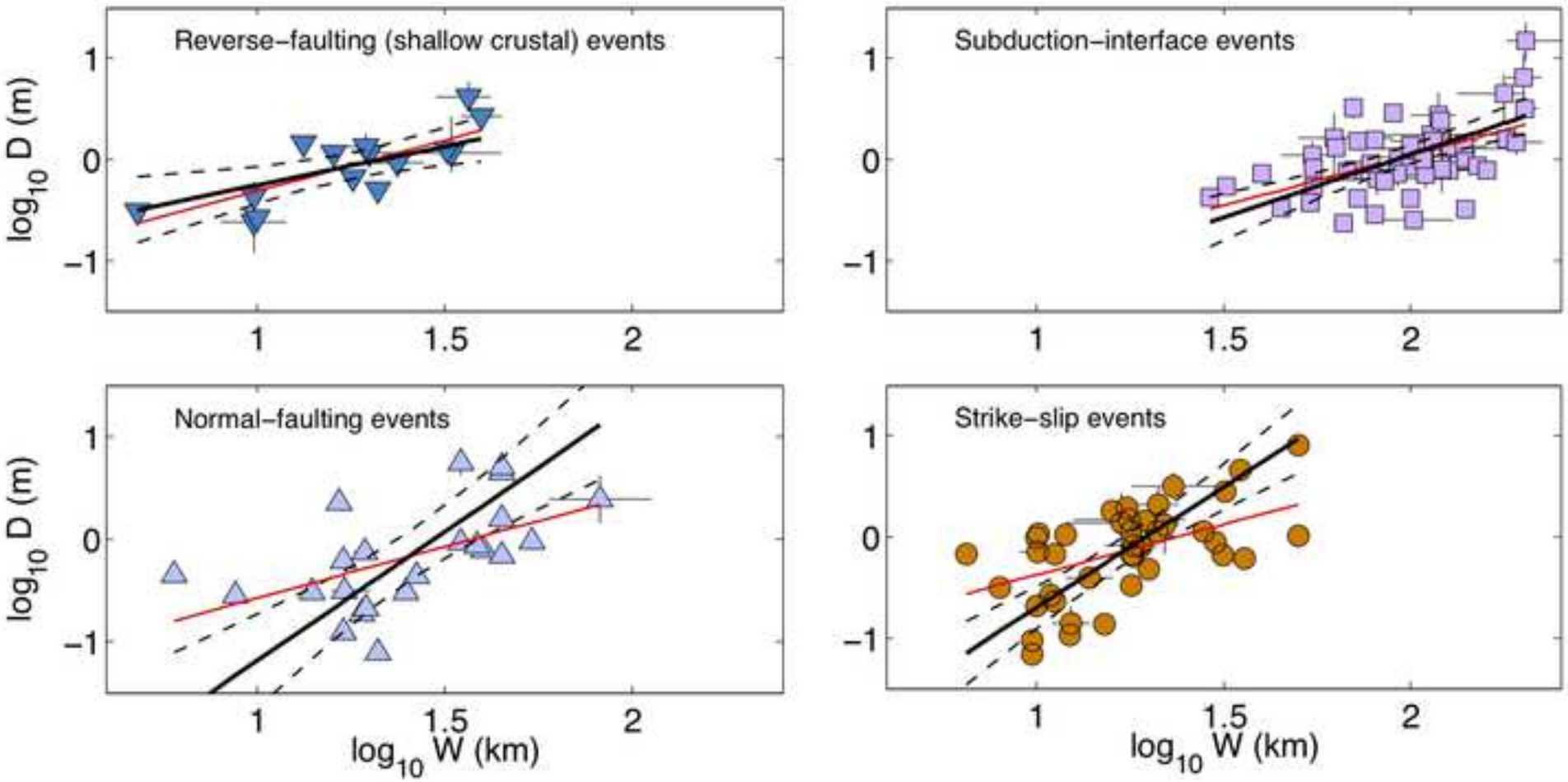

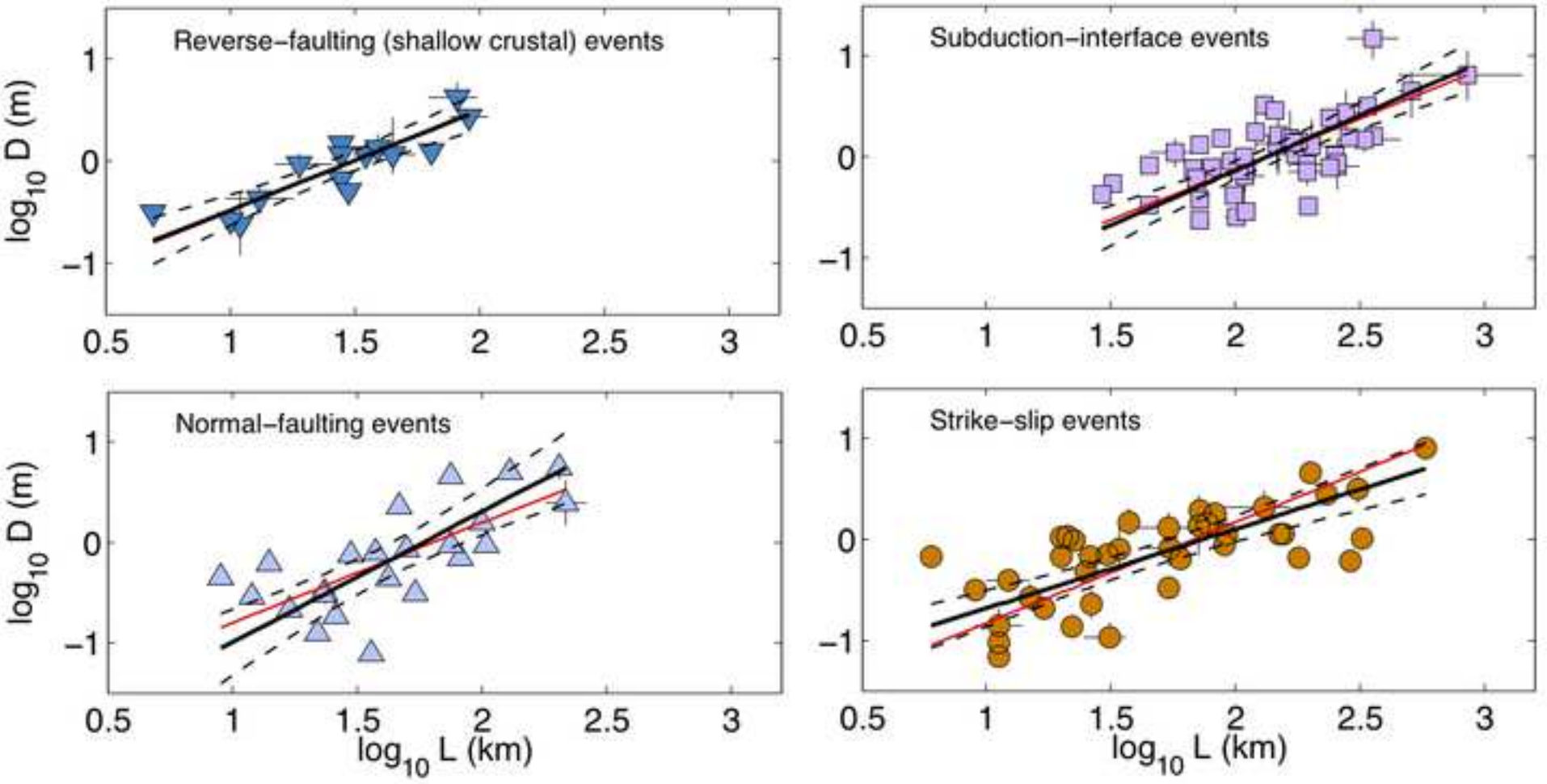

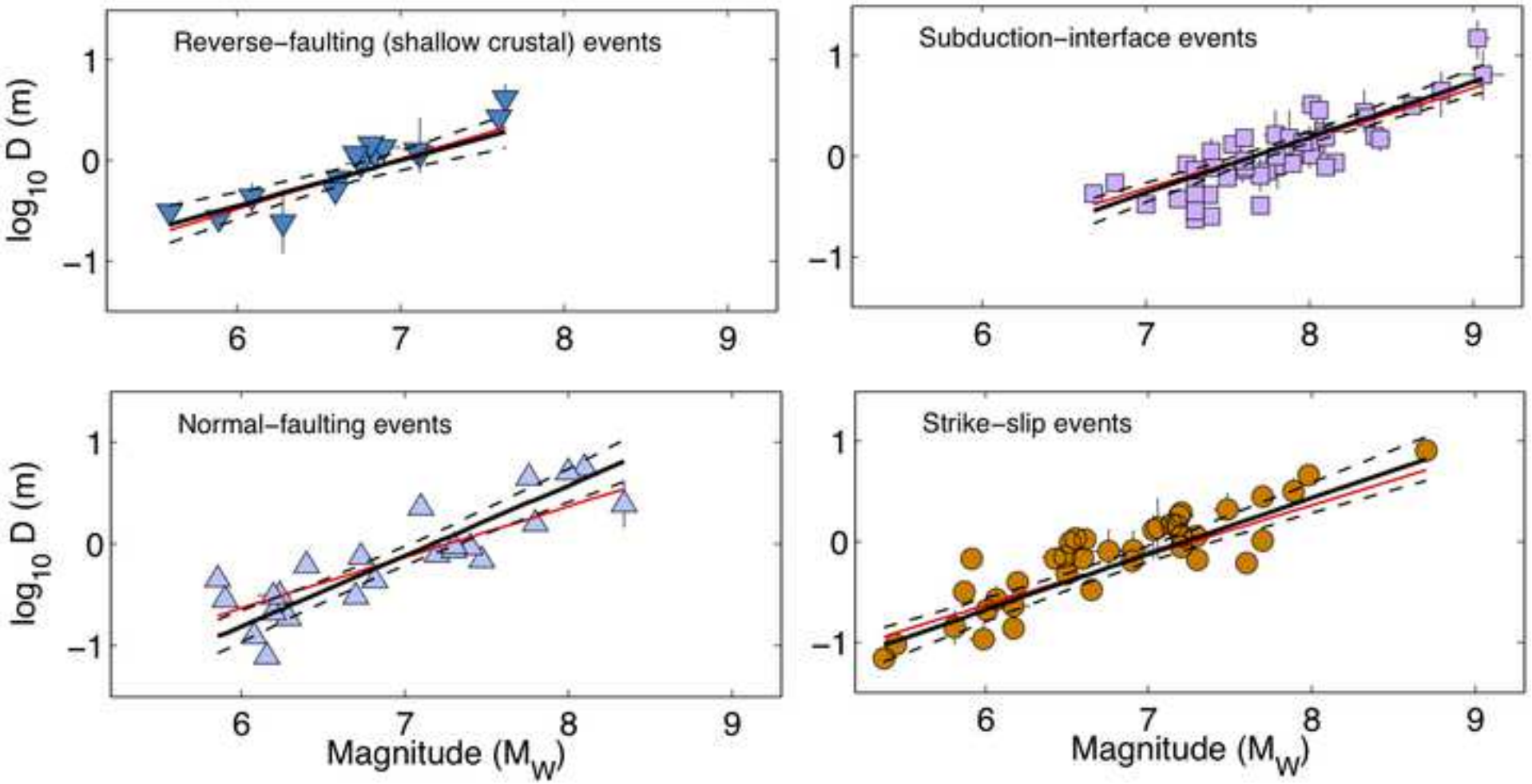

Figures

Click here to download Supplemental Material (Main Page, Tables, Figures)
neoBSSA-EQS-FigureS10.png

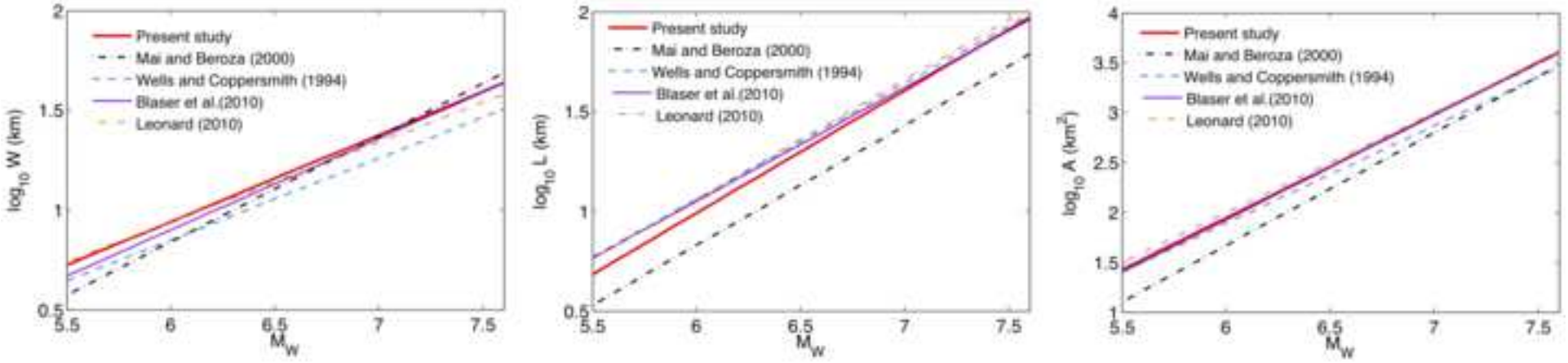

Figures

Click here to download Supplemental Material (Main Page, Tables, Figures)
neoBSSA-EQS-FigureS11.png

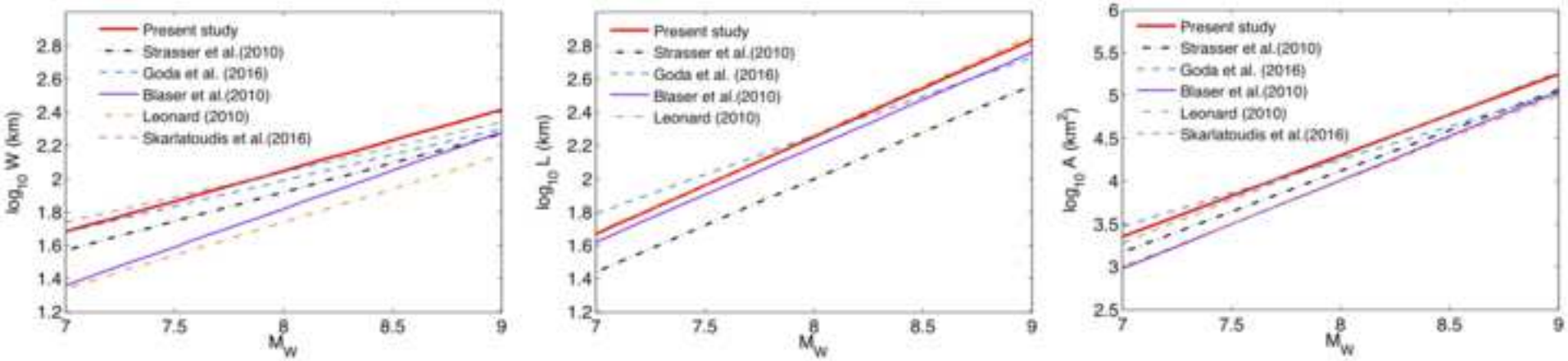

Figures

Click here to download Supplemental Material (Main Page, Tables, Figures)
neoBSSA-EQS-FigureS12.png

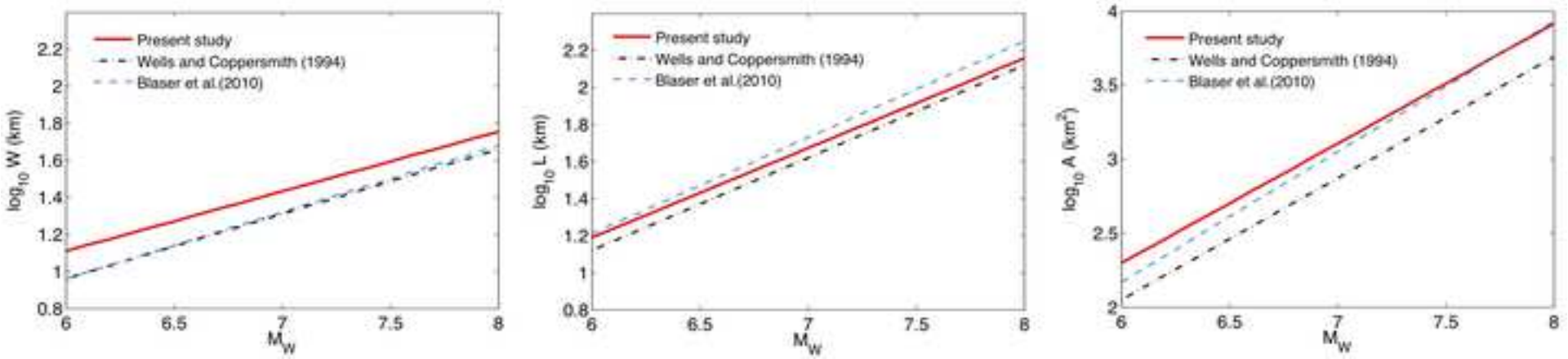

Figures

Click here to download Supplemental Material (Main Page, Tables, Figures)
neoBSSA-EQS-FigureS13.png

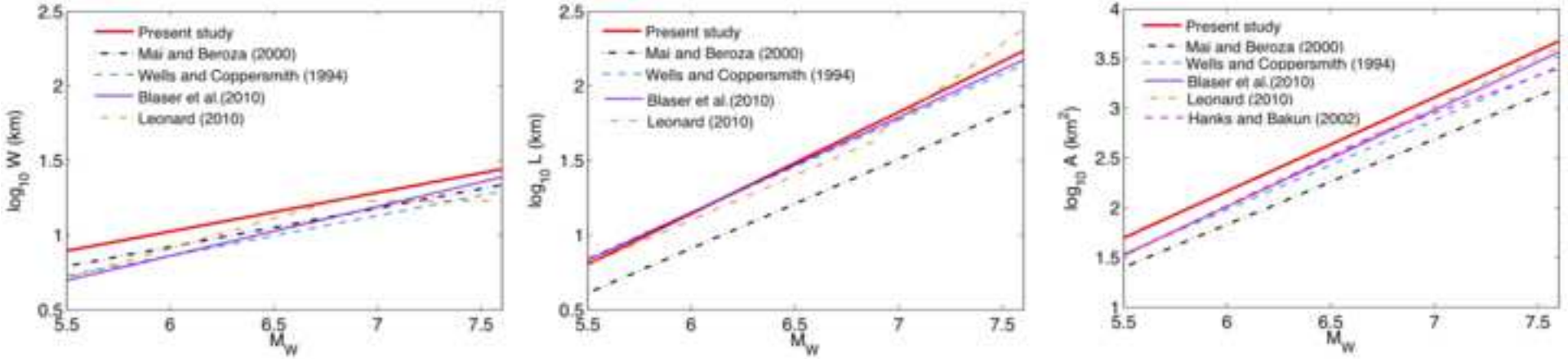

Figures

Click here to download Supplemental Material (Main Page, Tables, Figures)
neoBSSA-EQS-FigureS14.png

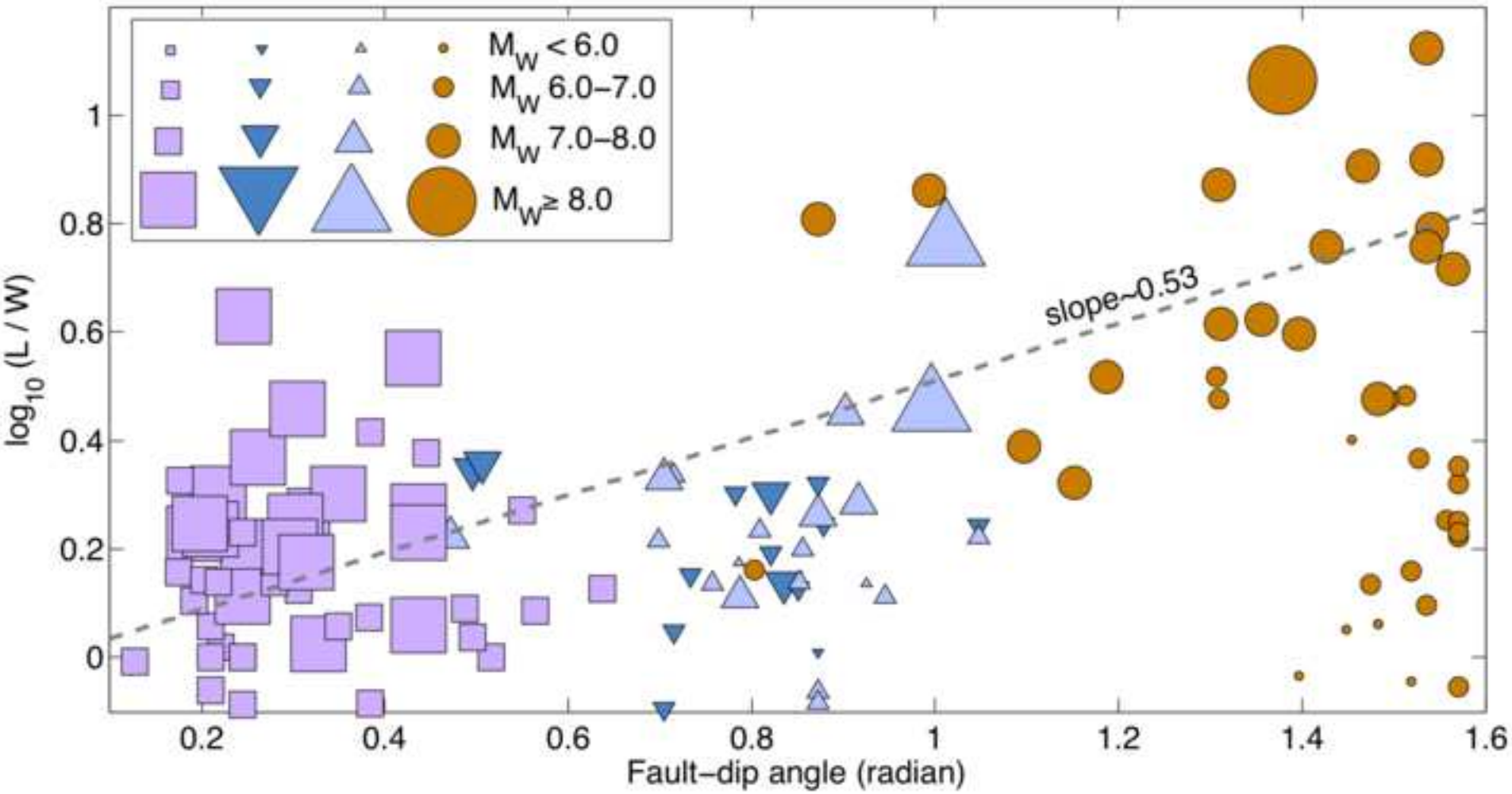

Bulletin of the Seismological Society of America

COPYRIGHT/PUBLICATION-CHARGES FORM

PLEASE FILL OUT AND SUBMIT THIS FORM ONLINE WHEN SUBMITTING YOUR PAPER OR FAX IT TO FAX NUMBER 503 405 7190

Manuscript Number: BSSA-D- 17-00017 [leave blank for new submissions]

Title: New Empirical Earthquake-Source Scaling Laws

Authors: Kiran Kumar Singh Thingbaijam, Paul Martin Mai, and Katsuichiro Goda

COPYRIGHT

In accordance with Public Law 94-533, copyright to the article listed above is hereby transferred to the Seismological Society of America (for U.S. Government employees, to the extent transferable) effective if and when the article is accepted for publication in the *Bulletin of the Seismological Society of America*. The authors reserve the right to use all or part of the article in future works of their own. In addition, the authors affirm that the article has not been copyrighted and that it is not being submitted for publication elsewhere.

To be signed by at least one of the authors (who agrees to inform the others, if any) or, in the case of "work made for hire," by the employer.

Authorized Signature for Copyright	Kiran Kumar Singh Thingbaijam Print Name (and title, if not author)	May 27, 2017 Date

PUBLICATION CHARGES

The Seismological Society of America requests that institutions supporting research share in the cost of publicizing the results of that research. The Editor has the discretion of waiving publication charges for authors who do not have institutional support. In addition to regular publication charges there is a nominal fee for publishing electronic supplements. Current rates are available at http://www.seismosoc.org/publications/bssa/authors/bssa-page-charges.php

Color options: Color figures can be published (1) in color both in the online journal and in the printed journal, or (2) in color online and gray scale in print. Online color is free; authors will be charged for color in print. You must choose one option for all of the color figures within a paper; that is, you cannot choose option (1) for one color figure and option (2) for another color figure. You cannot submit two versions of the same figure, one for color and one for gray scale. You are responsible for ensuring that color figures are understandable when converted to gray scale, and that text references and captions are appropriate for both online and print versions. Color figures must be submitted before the paper is accepted for publication.

Art guidelines are at http://www.seismosoc.org/publications/bssa/authors/bssa-art-submissions.php

Will publication charges be paid? Check one:

_____ **BOTH PUBLICATION CHARGES AND COLOR CHARGES WILL BE PAID**, and all color figures for this paper will be color both online and in print. This option requires full payment of publication & color charges.

__√__ **ONLY PUBLICATION CHARGES WILL BE PAID**, and all figures for this paper will be gray scale in print. Color figures, if any, will be color online.

_____ **REQUEST A REDUCTION IN PUBLICATION CHARGES.** Send a letter of request and explanation to the Editor-in-Chief at BSSA@seismosoc.org. Color figures, if any, will be color online but grey scale in print.

Send Invoice to: Prof. Martin Mai

Building 1, King Abdullah University of Science & Technology, Thuwal, Kingdom of Saudi Arabia

If your paper is accepted for publication, SSA requires that you fill out and submit an online billing/offprint form.

Questions regarding billing should be directed to the SSA Business Office,
400 Evelyn Avenue, Suite 201 Albany, CA 94706 USA Phone 510 525-5474 Fax 510 525-7204

Rev. 2014-05-29